POLITECNICO
MILANO 1863

SCUOLA DI INGEGNERIA INDUSTRIALE
E DELL'INFORMAZIONE

Feasibility study of energy-absorbing auxetic beams for rotorcraft subfloors

Tesi di Laurea Magistrale in
Aeronautical Engineering - Ingegneria Aeronautica

Author: **Matteo Moretti**

Student ID: 245047
Advisor: Prof. Alessandro Airoldi
Co-advisors: Antonio Maria Caporale
Academic Year: 2024-25

Alla mia nonna, l'angelo mi protegge.
A dieci anni esatti da quel 26 marzo, questo traguardo è per te.

Abstract

Evolving rotorcraft safety standards demand lightweight, crashworthy structures. In this context, the subfloor is a structural component that is critical for dissipating kinetic energy during impacts. To enhance its protective capabilities, auxetic metamaterials, such as re-entrant honeycombs, offer extraordinary energy absorption through their negative Poisson's ratio and foam synergy: by drawing material inward to densify locally, they ensure a stable, progressive crushing mechanism.

This thesis aims to optimize foam-filled aluminum re-entrant honeycombs as energy-absorbing subfloor components. Objectives include elastic characterization (focusing on Poisson's ratios and in-plane shear modulus), weight minimization, physical prototyping, and developing an experimentally validated Finite Element Model (FEM) for non-linear crash dynamics.

Analyses revealed a critical trade-off: foam-filled auxetic honeycombs excel in compression but lack the shear stiffness for structural roles. Conversely, applying continuous aluminum skins resolves shear compliance but transmits lethal peak forces. To bridge this gap, a novel 45° aluminum grid configuration was developed. This intermediate solution elevates shear resistance while preserving auxetic behavior. Dynamic simulations highlighted its exceptional potential in managing localized impacts, yielding Specific Energy Absorption (SEA) values significantly higher than global crushing. Finally, full-scale Anthropomorphic Test Device (ATD) simulations proved the auxetic foam-filled subfloor ensures survivability on both flat and uneven surfaces. The grid-stiffened variant, while slightly exceeding safety thresholds during uniform flat drops, surprisingly maintains survivable accelerations under severe asymmetric loads, confirming auxetic effectiveness in localized impacts and laying a robust foundation for future implementations.

Keywords: auxetic metamaterials; re-entrant honeycombs; helicopter subfloor; Specific Energy Absorption (SEA); rotorcraft crashworthiness; Finite Element Method (FEM).

Abstract in lingua italiana

La continua evoluzione della sicurezza elicotteristica richiede soluzioni capaci di bilanciare leggerezza e alta resistenza all'impatto (crashworthiness). In tale contesto, il sottopavimento è cruciale per dissipare l'energia cinetica. I metamateriali cellulari, come i nidi d'ape rientranti, offrono uno straordinario assorbimento d'energia grazie al coefficiente di Poisson negativo e alla sinergia con schiume polimeriche: richiamando materiale verso l'interno e densificandosi localmente, garantiscono infatti uno schiacciamento stabile e progressivo.
Questa tesi vuole ottimizzare nidi d'ape rientranti in alluminio riempiti con schiuma poliuretanica, valutandone l'integrazione come assorbitori nel sottopavimento. Gli obiettivi includono: caratterizzazione elastica (focus sui coefficienti di Poisson e modulo di taglio nel piano), minimizzazione del peso, prototipazione fisica e crash test, sviluppo di un modello FEM validato sperimentalmente per simulare crash non lineari. Le analisi statiche e dinamiche hanno evidenziato un compromesso critico: i nidi d'ape auxetici, pur eccellendo in compressione, risultano troppo cedevoli a taglio per ruoli strutturali. Viceversa, l'applicazione di pelli continue in alluminio risolve tale cedevolezza ma penalizza la crashworthiness, trasmettendo picchi di forza letali. Per superare questo limite, è stata sviluppata un'innovativa griglia in alluminio a 45°: una soluzione intermedia capace di fornire il vincolo geometrico necessario ad aumentare la resistenza a taglio, preservando al contempo il comportamento auxetico. Le simulazioni hanno evidenziato l'alto potenziale nella gestione degli impatti localizzati, con valori di Specific Energy Absorption (SEA) nettamente superiori a quelli dello schiacciamento globale. Infine, simulazioni con manichini antropomorfi (ATD) confermano che il sottopavimento con solo travi auxetiche garantisce la sopravvivenza su superfici sia piatte che irregolari. La variante a griglia, pur superando lievemente le soglie su terreno piatto, mantiene sorprendentemente le accelerazioni entro limiti tollerabili sotto severi carichi asimmetrici, confermando l'efficacia degli auxetici negli impatti localizzati e ponendo una solida base per sviluppi futuri.

Parole chiave: metamateriali auxetici; nidi d'ape rientranti; sottopavimento di elicotteri; energia specifica assorbita; crashworthiness; analisi agli elementi finiti.

Contents

Introduction

Over the years, the design of aeronautical structures has always been driven by a rigorous compromise between performance and weight reduction. In recent decades, however, the concept of safety has evolved beyond the simple prevention of structural failure under operational loads. A new driver has become fundamental in the design process: crashworthiness. This concept refers to the ability of an aircraft to protect its occupants during a possible crash event. The final goal is not just to prevent the structure from breaking, but also to ensure that it absorbs the impact energy, keeping the accelerations transmitted to the human body within survivable limits. This aspect is particularly important for helicopters, which operate in much more complex environments compared to fixed-wing aircraft. They fly at low altitudes, hover near obstacles, and land on unprepared terrain. Statistically, this makes them more exposed to hard landings or vertical impacts. Therefore, the airframe must include specific systems designed to manage crash energy.
The key structures involved in energy absorption in helicopters are the landing gear, the subfloor, and the seats. Located between the outer skin of the fuselage and the cabin floor, the subfloor plays a structural role, but it can also act as a crumple zone. Its job should be to deform plastically during an impact, dissipating kinetic energy to preserve the safety of the passengers. To improve the performance of such structures, research is moving towards advanced cellular materials and metamaterials. Among these, auxetic materials are extremely interesting for crashworthiness applications because of their exceptional properties. The term *auxetic* refers to structures whose Poisson's ratio is negative. Conventional materials, when stretched, become thinner, while auxetic materials behave oppositely, expanding laterally when pulled and contracting laterally when compressed. This counter-intuitive behavior offers significant advantages in engineering. Under compressive impact loads, an auxetic structure tends to densify locally. Instead of pushing material away from the impact point, it draws material in. This increases resistance to indentation and allows the structure to absorb energy through a more stable and progressive deformation mechanism, avoiding catastrophic buckling. Additionally, these open cellular structures can be combined with other materials. For instance, filling the empty cells with lightweight polymeric foam creates a hybrid structure, widely adopted

in different fields. The foam tends to stabilize the cellular skeleton and increase energy absorption, while the skeleton confines the foam. This synergistic interaction improves the overall stiffness and energy dissipation, creating a system with a very high specific strength-to-weight ratio.
The main goal of this thesis is to study re-entrant aluminum honeycombs, a specific type of auxetic structure, and evaluate their potential as energy absorbers for helicopter and VTOL subfloors. The work covers the entire process, from theoretical analysis to practical manufacturing and numerical simulation. The honeycomb geometric features became the basis for creating structures from scratch. The first specific objective is the elastic characterization of auxetic beams to understand how the geometric parameters of the repeated cell, such as angles, lengths, and thickness, influence the mechanical properties. Special attention is given to the in-plane shear modulus G_{12}, which is critical for the stability of the subfloor. The second step is the attempt to minimize the weight of the structure while maintaining high stiffness and ensuring that the resulting parameters create a structure that can actually be manufactured. Subsequently, an adapted configuration has been built and tested. This involves addressing the challenges of making the aluminum re-entrant core and correctly integrating the foam filler. Two specimens with the same geometric characteristics were constructed and subjected to a dynamic impact test using a vertical drop weight tower. Finally, a reliable Finite Element Model (FEM) is needed. The model must be able to predict both the linear elastic behavior and the non-linear behavior. In conclusion, a particular case study is analyzed: a realistic subfloor system is designed using the optimized auxetic structure, and its behavior is simulated during a crash. The performance is evaluated by examining the Specific Energy Absorption (SEA) and the stability of the crushing force.
The thesis is divided into four main chapters, following the logical flow from theory to application.

Chapter 1 presents the background of the research. It starts with an introduction about cellular materials and the concept of auxeticity. It explains the mechanics of the negative Poisson's ratio and why re-entrant hexagonal geometries are useful in engineering. Moreover, it discusses hybrid structures, focusing on the benefits of combining metal cores with foam filling. Then, it continues with an overview of helicopter crashworthiness, explaining why the subfloor is important and providing a state of the art presentation.

Chapter 2 is dedicated to the numerical analysis of mechanical properties. The elastic constants of the material ($E_{11}, E_{22}, \nu_{12}, G_{12}$) are calculated. The study compares four configurations: the empty re-entrant core, the sandwich panel with skins, the foam-filled

sandwich, and finally the foam-filled re-entrant honeycomb without skins. Fitting functions are derived to link the geometry to performance. The chapter ends with an optimization process to find the geometric parameters that offer the best trade-off between weight, shear stiffness, and auxetic behavior.

Chapter 3 describes the experimental work. It details the manufacturing process used to build the aluminum prototypes and the technique for foam filling. The chapter also reports the setup and results of static mechanical tests. These experimental data are essential for characterizing the base materials and verifying whether the theoretical predictions made in the previous chapter are accurate. Finally, the localized impact test performed on the manufactured specimens is described in detail. The output data are presented in the following chapter.

Chapter 4 focuses on non-linear crash analyses. Explicit dynamic simulations are performed using `Abaqus/Explicit` to study how the auxetic absorbers behave under impact. First, the numerical model is validated by comparing it with the experimental results from Chapter 3. Once the model is proven reliable, it is used to simulate two scenarios on the two optimized models obtained in Chapter 2: global compressive impact and localized impact. A new configuration emerges to satisfy the need for a solution that is less rigid than the skins but more resistant than the honeycomb solo. Skins are thereby substituted with an aluminum grid at a 45° orientation. The new concept is briefly studied under static conditions to prove its structural role and is finally tested dynamically. In conclusion, a full-scale application case study is considered: a subfloor system of beams subjected to crash loads on both plain and irregular terrains. The results are analyzed in terms of energy dissipation and load uniformity, providing a final assessment of whether this auxetic design is a valid solution for improving helicopter safety.

1 | Re-entrant honeycomb structures and helicopter subfloors

1.1. Auxetic metamaterials

In the landscape of advanced materials engineering, a specific class of cellular structures has emerged as a possible game-changer for energy absorption applications: auxetic materials. Conventional engineering materials typically exhibit a positive Poisson's ratio, contracting laterally when stretched and bulging when compressed. Poisson's ratio is defined as the negative of the ratio between transverse strain and axial strain:

$$\nu = -\frac{\epsilon_T}{\epsilon_L} \tag{1.1}$$

Auxetic materials possess a negative Poisson's ratio (indicated as `NPR` in the literature). This counter-intuitive property means that they expand laterally when placed under tension and contract laterally when compressed.

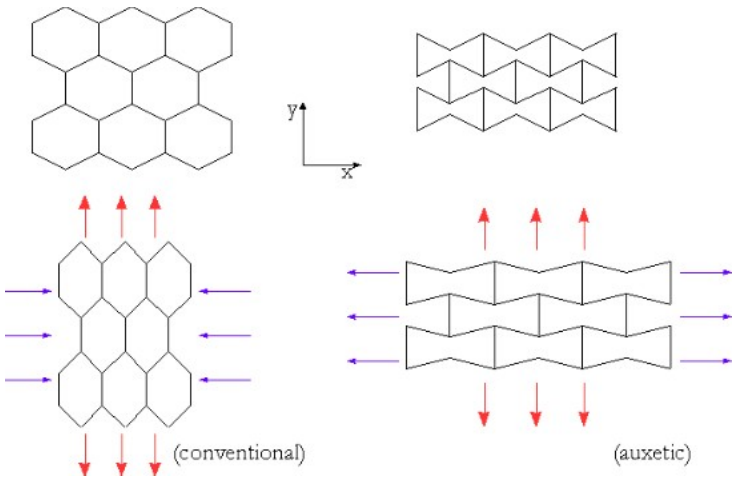

Figure 1.1: Comparison: auxetic ($\nu < 0$) and non-auxetic ($\nu > 0$) exagonal honeycombs.

This unique behavior is not usually the result of the intrinsic atomic arrangement of the base material, but rather arises from the carefully designed geometry of the cellular microstructure [29], as shown in Figure 1.2. For this reason, they are often referred to as *mechanical metamaterials* or *geometrically induced* auxetics. The macroscopic response is dictated by the internal topology, which can be engineered to achieve specific mechanical goals.

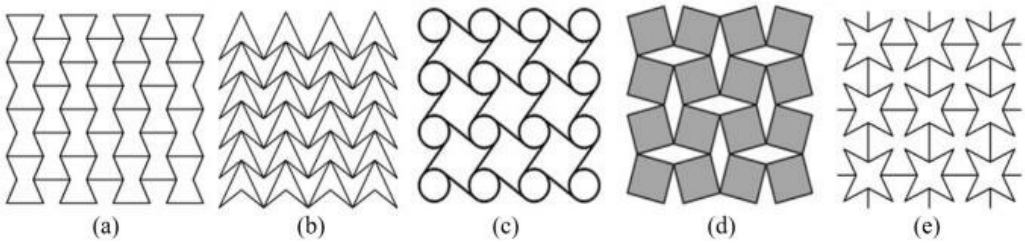

Figure 1.2: Auxetic geometries [31].

1.1.1. Mechanical properties

The implications of a negative Poisson's ratio extend beyond simple geometric deformation. From a mechanical point of view, one of the most significant benefits concerns the relationship between shear stiffness and volumetric stiffness. In typical isotropic materials, the resistance to volume change (bulk modulus, k) is typically much higher than the resistance to shape distortion (shear modulus, G). However, as the Poisson's ratio becomes negative, this relationship can change. For auxetic cellular structures, it allows for a significant enhancement of the shear modulus relative to the bulk modulus (G/k ratio). In practical terms, it means that while the absolute stiffness of these lightweight structures remains lower compared to solid metals, they are exceptionally efficient at resisting shear distortions for their specific weight [20].
Furthermore, auxetic materials demonstrate superior indentation resistance. When a common material is impacted locally, it tends to flow away from the impact zone, reducing density and resistance in that critical area. Conversely, an auxetic structure tends to contract laterally under compression, effectively drawing material into the impact zone [4]. This densification effect increases the local hardness and allows the structure to better distribute the impact load, making it ideal for protective applications and localized impact absorption.

1.1.2. Applications in engineering fields

The versatility of metamaterials has led to their adoption in various high-tech sectors, fundamentally driven by their enhanced shear modulus, acoustic damping, and superior energy absorption capabilities [27]. In the aerospace and automotive fields, auxetic cores present unique advantages for manufacturing double-curved sandwich panels: their inherent tendency to adopt a synclastic curvature allows the core ribs to remain perfectly normal to the curved surface, maximizing out-of-plane stiffness. Furthermore, they are extensively investigated for morphing airfoils, where the capability to undergo large shape changes without losing structural integrity allows for wings that adapt their profile for aerodynamic efficiency. Applications in thermal protection and turbine engine vanes are also possible. In space engineering, they are employed in smart deployable antennas, exploiting the ability to transition between compact states and extended operational configurations. Beyond aerospace, their superior impact-mitigating properties are exploited in ballistic armor and flexible protective gear. Their counter-intuitive lateral expansion under tension is utilized to create advanced fasteners and composites with exceptional pull-out resistance. Even in the biomedical sector, auxetic geometries are used for stents that expand uniformly within blood vessels, providing better support and reducing damage to vessel walls compared to traditional designs.

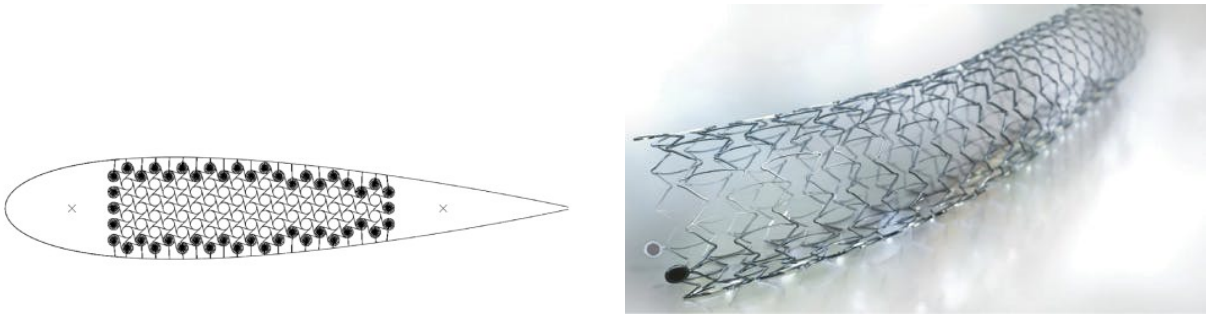

(a) Morphing wing design. (b) Auxetic venous stent.

Figure 1.3: Examples of auxetic materials applied in different engineering fields.

1.1.3. Re-entrant honeycomb

The present work focuses on re-entrant honeycomb structures, which have gained attention due to their relatively simple geometry, ease of fabrication, and predictable mechanical response [7]. The structure of a re-entrant honeycomb is derived from conventional hexagonal honeycombs. The difference lies in the inverted direction of the cell walls, producing a concave geometry similar to an hourglass. In this way, the structure gains auxetic behav-

ior under in-plane loading. Many studies show how this configuration allows for enhanced shear resistance, greater indentation resilience, and superior energy dissipation compared to non-auxetic counterparts [21, 26, 28, 31]. Typically, the materials adopted are aluminum alloys or composites. When fabricated from lightweight metals such as aluminum, re-entrant honeycombs combine the advantages of metallic ductility and recoverable deformation mechanisms associated with auxetic architectures, making them particularly suitable for aerospace crashworthiness applications. The high re-entrant curves that produce the hourglass shape can be more easily obtained with aluminum rather than with composites.

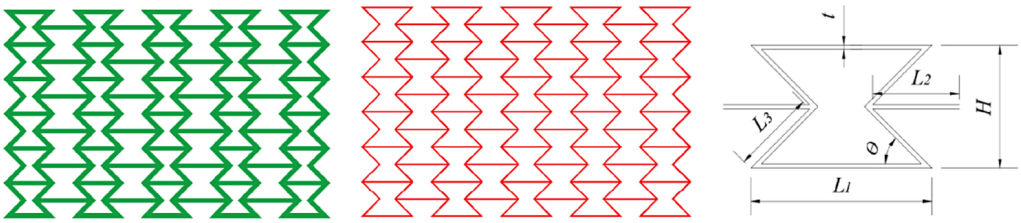

Figure 1.4: Typical re-entrant honeycomb configuration [10].

1.1.4. Re-entrant honeycombs as energy absorbers

The special mechanical behavior induced by the negative Poisson's ratio has made re-entrant cellular structures interesting for advanced crashworthiness research [6]. Unlike conventional topologies that often suffer from catastrophic localized buckling and sharp drops in load-bearing capacity, re-entrant honeycombs exhibit a distinct collapse mechanism under dynamic compression [30]. The inward folding of the oblique ligaments promotes a global densification process, which allows the structure to maintain a constant stress level over a significant displacement range. This extended plateau stress is a critical feature for safety-critical applications, as it maximizes the energy dissipated while limiting the peak deceleration forces transmitted to the cabin.

The efficiency of this energy absorption mechanism is not fixed but is highly dependent on the specific geometric parameters of the unit cell, particularly the wall slenderness. As highlighted in recent experimental studies on metallic auxetic honeycombs [10], two distinct deformation modes can be identified depending on the ratio between wall thickness and strut length (t/l). *Thick-walled* configurations tend to dissipate energy through the formation of stable plastic hinges at the cell nodes and the subsequent rotation of ligaments. This mode is more desirable as it generates a smooth force-displacement curve. Conversely, *thin-walled* structures are more subjected to strut buckling before full plastic

rotation occurs, leading to fluctuations in the crushing force, which reduces the overall efficiency.

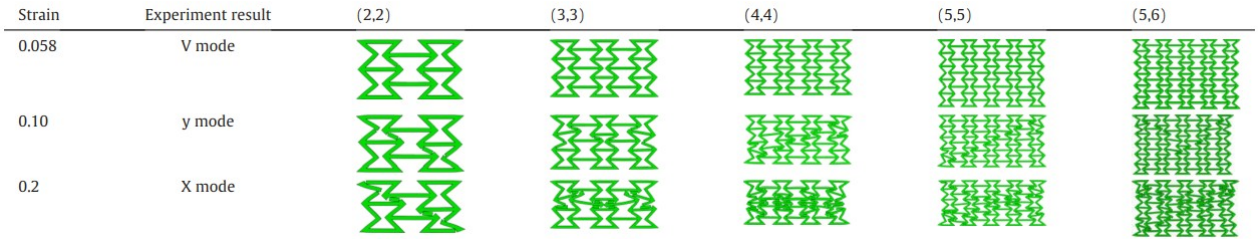

Figure 1.5: Deformation modes of thick-walled honeycomb with different number of cells.

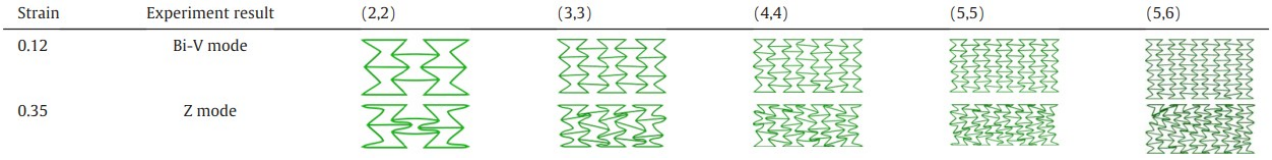

Figure 1.6: Deformation modes of thin-walled honeycomb with different number of cells.

Moreover, the re-entrant angle dictates the degree of auxeticity. Smaller angles produce more closed cells, which intensify the draw-in mechanism, enhancing the indentation resistance during the strain-hardening stage.
Despite these theoretical advantages, the practical implementation of re-entrant geometries faces challenges related to fabrication. Standard manufacturing techniques for honeycomb cores, such as expansion, are ill-suited for the re-entrant hourglass shape due to the inward-facing walls. While recent trends often rely on Additive Manufacturing to overcome these geometric constraints, this thesis adopts an alternative experimental approach based on precision machining and manual assembly. This choice was driven by the specific requirement to utilize standard aluminum alloys with well-characterized plastic properties. By avoiding the potential porosity and brittleness often associated with 3D-printed metals, this fabrication strategy ensures that the experimental results strictly reflect the topological behavior of the auxetic structure rather than material-induced properties.

1.1.5. Foam filler

The auxetic topologies face a notable limitation inherent to all cellular solids: the presence of large void fractions reduces the absolute stiffness compared to solid structures. To overcome this trade-off between lightweight design and structural rigidity, a promising engineering solution is the integration of a secondary phase, typically a lightweight polymeric foam, within the metallic lattice [14].

The creation of such foam-filled hybrid structures is recent and represents a significant step forward in crashworthiness technology. The mechanical advantage of this configuration lies in the synergistic interaction between the two phases. The foam filler acts as a stabilizing medium for the thin-walled aluminum ligaments, effectively creating a continuous support that delays the onset of local instability and prevents premature buckling. Consequently, the structure undergoes more uniform global deformation under load. This interaction enhances the best properties of both materials: the high strength of the metallic skeleton and the energy-dissipating capacity of the porous filler [21].
The benefits of this approach have been extensively explored in recent literature. Hui Chen Luo et al. in [23] conducted a comparative study on the dynamic response of re-entrant and hexagonal honeycombs reinforced with slow-recovery foam. Their research, based on both numerical simulations and experimental testing at various impact velocities, highlighted a crucial geometric effect: foam-filled re-entrant honeycombs exhibit superior stiffness compared to their hexagonal counterparts. Furthermore, the study demonstrated that the energy absorption capacity is not static but increases significantly with variations in cell wall thickness and re-entrant angle, proving the tunability of the hybrid system.

A further advancement in this field was presented by Novak et al. in [28], who investigated the behavior of auxetic aluminum panels characterized by graded geometry and filled with polyurethane foam. By comparing six different configurations, ranging from uniform to graded and foam-filled variants, the authors observed a strong correlation between numerical predictions and experimental results. The key finding was that the foam-filled panels not only achieved higher Specific Energy Absorption (SEA) values but also exhibited a much more stable deformation pattern compared to the empty specimens, mitigating the risk of localized failure bands.
Synthesizing the results from the analyzed studies, foam-filled auxetic absorbers exhibit enhanced performance due to the synergistic interaction between the metallic skeleton and the filler. The foam redistributes loads and delays failure, allowing for extensive plastic deformation. The energy absorption is also more effective when the wall thickness increases. Finally, these hybrid structures demonstrate positive strain-rate sensitivity, meaning their energy absorption efficiency increases at higher impact velocities.

1.2. Helicopter crashworthiness and subfloor system

While the potential of auxetic materials is vast, their application in rotorcraft crashworthiness addresses a very specific set of challenges. Over the years, aeronautical structures have been developed under strict safety regulations. Dimensions, performance, and loads

have been constantly improving, forcing the evolution of the materials and construction technologies adopted. Stiffness and strength remain fundamental properties to investigate during the design phase, always considering the aim of aeronautical structures: minimum weight. Although starting in the 1970's, new requirements in terms of tolerance to damage and response to fatigue have emerged, deeply influencing design choices. The concept of passive safety began to make its way through the industry: the ability of a structure to guarantee protection to occupants in the case of an accident became a key design driver for both fixed-wing and rotary-wing aircraft.
In helicopters and VTOLs, the capability of the structure to absorb and dissipate energy during a possible impact is particularly critical. Low altitude flight profiles and complex operational environments, statistically speaking, make helicopters more exposed to crash events than fixed-wing aircraft. For this reason, a significant amount of research is conducted on the improvement of crashworthiness, which means that the constructor can ensure the ability of the structure to preserve occupant survival space and limit accelerations during a crash event. The key structures involved in energy absorption in helicopters are the landing gear, the subfloor, and the seats, as shown in Figure 1.7. Together, they act to absorb and distribute the impact energy in a precisely controlled manner [2].

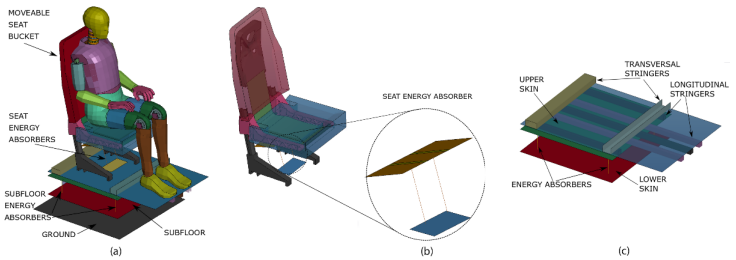

Figure 1.7: Typical energy absorption systems in helicopters [5].

The international regulations imposed by the Federal Aviation Administration (FAA) concern the sole seat system. In Europe, EASA CS-27 and CS-29 must be used for rotorcraft [12, 13]. Considering a seat installed on a horizontal sled facility in a 60° nose-up attitude and subjected to a 30 g horizontal acceleration pulse, the most important certification criterion for the seat regards the lumbar spine load, which must be limited to 6670 N.
The subfloor, which is not mentioned in the regulations, plays a central role in the entire system and will be the focus of investigation in the present thesis work. The subfloor connects the landing gear to the fuselage, and it is responsible for the correct distribution of loads and must deform in a controlled manner in order to dissipate impact energy.
Nowadays, energy absorbers are thin-walled metallic elements. The most commonly used

material is aluminum alloy, and they are usually made from riveted plates and installed at structural intersections. The absorbers are strategically installed within the subfloor to collapse plastically under crash loads. Their performance depends on many parameters, mainly geometry, wall thickness, and material properties such as plastic strength, strain rate sensitivity, and ductility. These properties directly influence the total energy that can be absorbed, the deformation mode, and the risk of premature fracture, which can compromise efficiency [5].

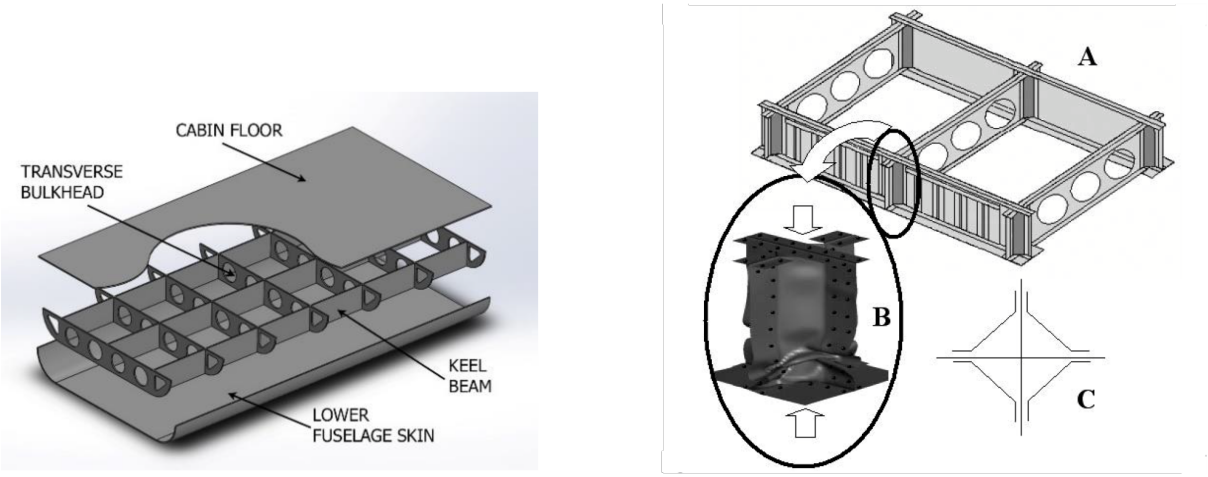

Figure 1.8: Subfloor particular [5] and aluminum alloy absorber at intersection [2].

Energy absorption and load transmission are the two key contrasting requirements that must be balanced in the design of helicopter crashworthy structures to achieve optimal performance. Numerical simulations using finite element methods are now essential tools for obtaining this balance, allowing for complex crash scenarios. The absorbers must deform plastically to dissipate energy, while the surrounding structural elements must remain sufficiently strong to transmit loads and preserve the survival cell.
The aluminum absorbers are designed to undergo progressive plastic collapse under axial compression, which occurs through the formation of sequential folds, allowing the energy to be absorbed at almost a constant load level. The design of such absorbers is governed by several parameters: the available stroke, the maximum allowable load, and the specific energy absorption (SEA), defined as the energy absorbed per unit mass (J/kg). The goal is to maximize absorbed energy without exceeding the load levels that would cause excessive deceleration of the occupants. A trade-off between stiffness and controlled plastic deformability is necessary [22].
Experimental and analytical studies have demonstrated that aluminum subfloor absorbers can significantly reduce the forces transmitted to the cabin during vertical impacts of up to

10 m/s [19], thereby improving occupant survivability. However, aluminum alloys exhibit low strain-rate sensitivity. On one hand, constructors prefer the safe, tested, and effective choice of aluminum subfloor absorbers. On the other hand, constant improvement in research on new materials shows that other promising solutions are possible. For instance, the current standard industrial solutions exhibit very high values of Initial Peak Crush Force (IPCF) before the onset of plastic deformation. As early as 1981, Bell researcher J. D. Cronkhite anticipated smoother, peak-free load-displacement curves as the ideal design target [9]. The issue is that this initial activation peak load transmits dangerous accelerations to the cabin and, thus, to the occupants. Moreover, to avoid global buckling and to prefer progressive folding, these structures demand a significant mass, imposing a weight penalty.

Figure 1.9: Collapse mechanism in an aluminum alloy absorber [2].

To address these issues, this thesis research investigates the potential of cellular materials, with a specific focus on re-entrant aluminum honeycombs, as possible alternative energy absorbing devices. The auxetic topologies are designed to promote a more stable and progressive collapse mechanism. The objectives are to minimize the initial peak force and achieve a flat force-displacement curve in the study of crashing while obtaining a sufficient Specific Energy Absorption (SEA) value.
Among the numerous advantages of cellular materials, three key characteristics are particularly relevant for this application.

The first one is the seamless integration between re-entrant geometries and polymeric foams, as shown in Figure 1.10. Extensive experimental testing on graded auxetic panels has confirmed that foam filling leads to much more stable deformation patterns and higher specific energy absorption compared to empty honeycombs, as aforementioned in Paragraph 1.1.5. Moreover, very recent studies show that foam densification within the pores effectively increases stiffness. The reinforcement effect proves to be robust with different geometric configurations, enhancing mechanical properties regardless of variations in unit cell density or cell wall thickness [21]. Among the possible technological solutions, *direct foaming* approach has recently been proven to be the most effective: it ensures superior interfacial adhesion between the foam and the host structure, creating a synergistic effect that prevents component separation [31].

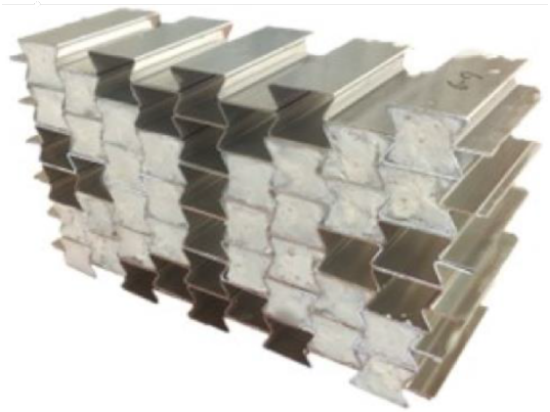

Figure 1.10: Example of PU foam filling for an aluminum re-entrant honeycomb structure [28].

The second characteristic is the excellent response to localized loading. Considering realistic scenarios for helicopters involving uneven or rugged terrain, re-entrant honeycomb structures demonstrate great adaptability and compliance. Professor A. Airoldi specifically addressed this capability [3] and demonstrated that foam-filled auxetic absorbers not only exhibit superior performance under localized impact but also improve the load uniformity ratio and energy dissipation. Furthermore, due to the negative Poisson's effect, these structures present naturally high indentation resistance. For instance, auxetic lattices densify under load, allowing them to better accommodate and resist penetration from potentially rugged surfaces.
Finally, re-entrant honeycombs provide a significant enhancement in shear modulus relative to bulk modulus for a given in-plane stiffness due to their negative Poisson's ratio. This makes them potentially suitable for structural applications, such as the subfloor.

2 | Characterization of the elastic properties

As presented in Chapter 1, the subfloor of a helicopter, which connects the cabin floor and the lower fuselage skin, is a structural macro-component that also plays a crucial role in energy absorption during possible impact events. The area is required to deform in a controlled manner so that it can dissipate the maximum kinetic energy and reduce the loads transmitted to occupants. Traditionally, such components rely on stiff, reinforced beam-column intersections and diagonal strut configurations, which exhibit well-understood and controlled crushing mechanisms, and the collapse behavior is mostly predictable. However, the demand for lighter, safer, and more efficient crashworthy designs, along with advances in material research, has driven the development of innovative structural configurations, such as auxetic re-entrant honeycombs, that can possibly outperform conventional solutions, and substitute them in the future.

The present work focuses on the development of a re-entrant aluminum honeycomb designed as an innovative energy-absorbing element for helicopter subfloor applications. Before crashing, the first fundamental step is the linear static characterization of the structure.
The initial phase of the study involves the generation of the 3D auxetic structure, which was realized through a parametric `MATLAB` script that creates a periodic honeycomb geometry with controlled parameters:

- cell dimensions (length and height);
- re-entrant angle;
- aluminum sheet thickness;
- number of horizontal and vertical cells in the entire structure.

Below, the key features of the honeycomb generator are described. The `MATLAB` function `function_rhc_generator` was developed with the following logic.

1. **Input and validation:** recalls the input parameters and mesh subdivision parameters. Basic checks ensure that the chosen dimensions and angles produce a valid re-entrant geometry; otherwise, the analysis has no reason to start, and the solver moves to the following set of parameters.
2. **Unit cell construction:** a single re-entrant honeycomb cell is generated by defining six key points that represent the vertices of the concave hexagonal cell. These points are connected to form the edges of the hourglass.
3. **Node discretization:** the edges of the unit cell are divided into a specified number of elements (`elside`) to discretize the geometry, and it can be modified to control the mesh density.
4. **Cell replication (horizontal and vertical):** the base cell is replicated in the horizontal and vertical directions according to the input parameters (`n_horizontal` and `n_vertical`).
5. **Extrusion in the thickness direction:** the 2D pattern is extruded along the z-axis by a defined width (`elwidth`), resulting in a 3D representation of the honeycomb structure suitable for finite element modeling.
6. **Merging and cleaning:** duplicate nodes and overlapping elements are identified and merged based on a small positional tolerance.
7. **Element generation:** quadrilateral elements are created by linking corresponding nodes across the extruded layers.
8. **Geometric trimming and centering:** the model is cropped to match the specified overall dimensions and then translated to ensure it lies entirely within the positive x-domain.
9. **Classification of elements:** elements are categorized into horizontal and oblique sets based on their orientation, because it will be necessary to specify different shell thicknesses later.
10. **Foam point definition:** auxiliary points representing foam positions (upper, lower, and internal) are generated. These will be used in future analyses involving foam filling.

The function `main.m` integrates the geometry generator into the complete meshing process. The script controls mesh density and the extrusion along the z-direction, which will be set to 10 mm for the first static analyses. Later, it will become a design parameter, and mesh density can be regulated along the thickness. Then, the function calls the generator

function to build the 3D auxetic geometry and retrieves the arrays containing nodes and elements. After this step, it writes all the relevant data into the output file `mesh.inp`, following the strict syntax and order required by `Abaqus` input files.

The file writing procedure includes the definition of the

```
*PART, NAME=REENTRANT_HONEYCOMB
```

the definition of nodes and elements inside the part, the assignment of element sets (`ELSET`s) for horizontal and oblique regions, and the creation of useful node sets (`NSET`s). Different shell sections are defined for each `ELSET`: oblique elements are assigned the nominal thickness, while horizontal elements are given a doubled thickness to account for their actual double thickness due to the construction technique. Finally, the total length and height of the model are computed and returned as output parameters.

The use of 4-node doubly curved general-purpose shell elements with reduced integration (`S4R` in `Abaqus`) is justified by the slender geometry of the cell walls, whose thickness is small compared to the in-plane cell dimensions. Modeling the structure with such elements allows for an accurate representation of bending and membrane behavior while maintaining a low computational cost under linear static loading conditions.

The constitutive behavior of the aluminum alloy was modeled to accurately capture the severe dynamic response characteristic of crash conditions. The `*MATERIAL` definition includes an initial isotropic linear elastic phase, defined by a Young's modulus of 70 GPa and a Poisson's ratio of 0.3. The plastic behavior and strain-rate effects were modeled using the Johnson-Cook formulation. To simulate structural failure and localized fractures in the cell walls, a Johnson-Cook damage criterion was also applied. This was paired with a displacement-based damage evolution law to handle stiffness degradation and element deletion during the impact. All material (called Al-2024-T3) parameters were taken from the literature [25].

Subsequently, the generated geometry is implemented in `Abaqus` to perform the linear static characterization. The linear analysis allows for assessing the stiffness distribution, identifying load paths, and calculating stiffnesses and Poisson's ratios.

The `Job-1.inp` file acts as the global `Abaqus` input deck that governs the complete finite element simulation. Its structure integrates the mesh data previously generated, so the first line of the file is simply:

```
*INCLUDE, INPUT = mesh.inp
```

In this way, the `Job-1.inp` file remains unchanged and includes the new geometry gener-

ated at each iteration.

The global assembly and the reference points used for applying boundary conditions and loads are then defined. Each reference point (`RP1`, `RP2`, `RP3`, `RP4`) is connected to one of the honeycomb boundaries via constraint equations (top, bottom, left, and right edges). The `*INSTANCE` is then created.

Then, depending on whether E_{11}, E_{22}, or G_{12} is being assessed, different sets of boundary conditions and loads are applied to the reference points. The material section defines the elastic properties of aluminum through a simple isotropic law, while the `*STEP` block describes the static analysis procedure. Field and history outputs are finally requested to store displacements, stresses, and reaction forces.

The entire workflow is automated in `MATLAB` by the `montecarlo.m` script, which coordinates the generation, execution, and post-processing of multiple simulations. The script reads a population of input parameters from the file `population.csv`, where each row corresponds to an individual configuration of geometric parameters (cell size, cell height, angle, thickness, number of horizontal cells, number of vertical cells). These parameter sets have been previously generated by the `LHS.m` script using a Latin Hypercube Sampling technique, which ensures efficient and statistically uniform exploration of the possible design choices. When a geometric configuration is impossible, the honeycomb generator returns a warning so that the analysis can be skipped.

For each individual in the population, `montecarlo.m` performs the following sequence:

1. Deletes any temporary files from previous runs, which is important because every individual runs as *Job-1*. Only at the end of the simulation the result is re-numbered.
2. Calls the `main.m` script to generate a new `mesh.inp` corresponding to the current parameter set.
3. Executes the `Abaqus` simulation through the command window as follows:

```
abaqus job=Job-1 double cpus=4
```

4. Monitors the progress of the analysis, waiting for the `.lck` and `.sta` files to update.
5. Runs a specific Python extraction script (`extraction.py`) to collect key output quantities (e.g., reaction forces or displacements).
6. Saves each result under a unique name (`data-i.rpt`, `Job-i.odb`) corresponding to the current iteration.

Through this integration, each `montecarlo.m` iteration generates a unique honeycomb geometry, runs a complete FEM analysis in `Abaqus`, and stores the output data for post-processing.

Before starting the static analyses, it is necessary to introduce the adopted coordinate system (Figure 2.1). The structures are modeled in the described manner:

- the x-direction (or direction 1) follows the honeycomb along its length;
- the y-direction (or direction 2) follows the honeycomb along its height, and it is directly associated with the parameter `cell height`;
- the z-direction (or direction 3) regards the thickness (extrusion).

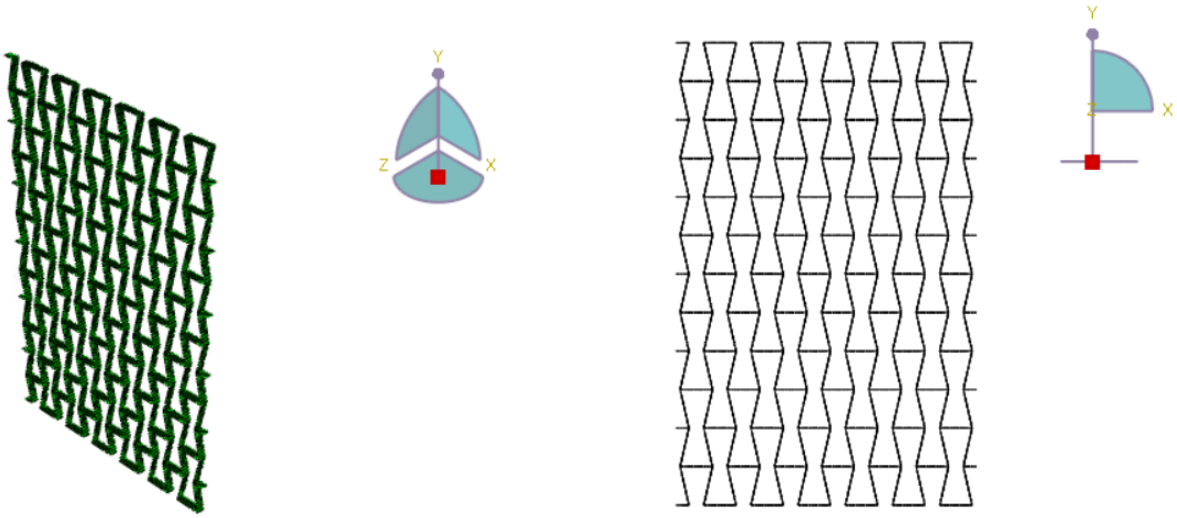

Figure 2.1: Coordinate system in a generic honeycomb structure generated in `Matlab` and imported in `Abaqus/CAE`.

2.1. Evaluation of the transverse Young's modulus E_{22} and Poisson's ratio ν_{21}

The first analyses aim to evaluate the transverse Young's modulus (E_{22}) and the associated Poisson's ratio (ν_{21}) considering the solo re-entrant honeycomb. The script `main.m` generates the re-entrant honeycomb specimen and produces the `mesh.inp`, which is ready to be imported into `Job-1.inp`. The mechanical test is designed to simulate a uniaxial compressive load applied along the global y-direction, corresponding to the transverse direction of the auxetic structure.

2.1.1. Boundary conditions and load

The four reference points (RP1-RP4) are kinematically coupled to the corresponding node sets located on the top, bottom, left, and right edges of the structure using simple linear constraint equations. In this way, each edge behaves as a rigid line that can move or deform only according to the associated reference point. The spatial disposition of the RPs can be arbitrary since the important issue is the correct definition of sets, equations, and constraints.

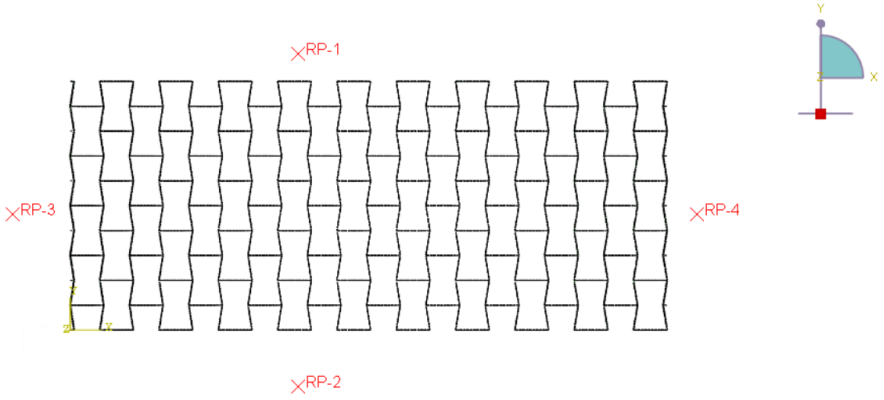

Figure 2.2: Spatial disposition of the 4 reference points in a generic honeycomb structure generated in Matlab and imported in Abaqus/CAE.

The lower edge (RP2) is fully constrained by an ENCASTRE boundary condition, which fixes all translational and rotational degrees of freedom. The right edge (RP4) is constrained in the x-direction to prevent lateral rigid-body motion. The bottom corner nodes are fixed in the out-of-plane direction ($U_3 = 0$) to stabilize the model. The top edge (RP1) is subjected to a concentrated vertical compression force of 100 N in the negative y-direction. This load is evenly distributed over all nodes belonging to the top edge of the honeycomb, thanks to the equation imposed on RP2.

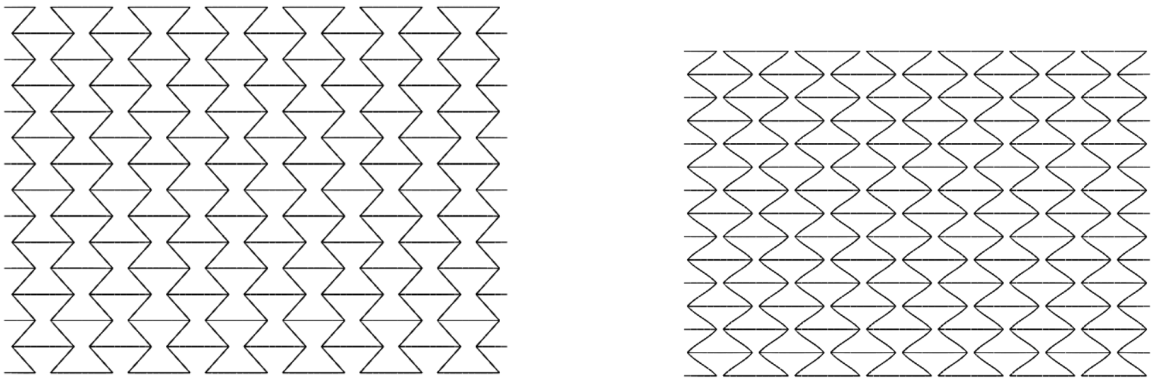

Figure 2.3: Example of undeformed and deformed structure (resulting from Job-2).

2.1.2. Output extraction

After each simulation is successfully completed, the `extraction.py` script automatically accesses the output database (`Job-1.odb`) using the `Abaqus Python API`. The script extracts the displacement fields at the reference points, which act as macroscopic measurement nodes for the test.

Specifically, it extracts the following values.

- The vertical displacement component U_2 at the top reference point (`RP1`), which corresponds to the global elongation in the loading direction.
- The horizontal displacement components U_1 at `RP3` and `RP4`, which represent the average lateral contraction or expansion of the left and right edges. Actually, U_1 at `RP4` is expected to be zero because of the imposed boundary condition, resulting in superfluous but easily accessible information for quick checks.

Data is finally stored in the `data.rpt` file.

2.1.3. Post-processing

A total of 200 configurations have been submitted for analysis, but only 129 were completed successfully.
Afterwards, all the `data-`i`.rpt` files are imported in `MATLAB`. The post-processing script automatically reads the geometric parameters of each configuration from the `population.csv` file and associates them with the corresponding displacement data.
For each individual configuration, the script first reconstructs the macroscopic dimensions of the specific configuration. The effective cross-sectional area subjected to loading is then

obtained as:

$$A_{XZ} = \text{model length} \cdot \text{extrusion width}$$

where the extrusion width represents the constant thickness of the model in the out-of-plane z-direction, set to 10 mm. Given the applied vertical load $F = 100$ N, the average normal stress in the loading direction is calculated as:

$$\sigma_{22} = \frac{F}{A_{XZ}}$$

The axial and transverse strains are evaluated as follows:

$$\varepsilon_{22} = \frac{\Delta y}{\text{model height}}, \qquad \varepsilon_{11} = \frac{\Delta x}{\text{model length}}$$

where $\Delta y = \max(|U_2|)$ is the maximum vertical displacement and $\Delta x = \max(|U_1|)$ is the maximum horizontal displacement. The effective Young's modulus in the loading direction and the in-plane Poisson's ratio are calculated as:

$$E_{22} = \frac{\sigma_{22}}{\varepsilon_{22}}, \qquad \nu_{21} = -\frac{\varepsilon_{11}}{\varepsilon_{22}}$$

The script iterates over all individuals contained in the population matrix, automatically skipping missing results associated with impossible configurations. The computed values of E_{22} and ν_{21} are appended to the corresponding geometric parameters and stored in the final output file `results_with_E_nu.csv`.

2.1.4. Empirical fitting of the results

The very first approach attempted to consider all the independent parameters and their interactions as possible regressors. The fitting procedure employed the `MATLAB` `stepwiselm` function, with a quadratic polynomial model for higher accuracy. This particular function iteratively adds or removes predictors and makes the terms interact according to statistical significance, trying to find an optimal balance between model complexity and precision.

After model training, the predictions were obtained and compared to the values calculated during `Abaqus` simulations. Although it is simple to notice that `stepwiselm` tends to overfit data due to the presence of too many regressors and cross interactions. The two models for E_{22} and ν_{21} were found to be too specific and valid only for combinations of parameters similar to the simulations analyzed. An approximate equation for E_{22} resulting

from this process is shown.

$$E_{22} \approx 3329.10 + 67076.64 \left(\frac{t}{l}\right)^3 + 7.33 \left(\frac{h}{l}\right) - 1818.35 \cos(\alpha) - \frac{3788.79}{\sin(\alpha)} \tag{2.1}$$

Despite its limitations, this preliminary step proved valuable by verifying the underlying physics. The regression successfully captured the fundamental scaling laws, most notably the $(t/l)^3$ and slenderness dependences, and the angle-driven interactions, consistent with established analytical models from the literature.

2.1.5. Physics-enforced fitting of the results

The mechanical behavior of auxetic materials, such as re-entrant honeycombs, can be interpreted within the wider framework of the classical analytical formulations proposed by Ashby and Gibson [16]. Their approach relates the effective mechanical properties of the structure to its geometrical parameters through scaling laws of the form:

$$\frac{E^*}{E_s} = C_E \left(\frac{\rho^*}{\rho_s}\right)^n \qquad \text{and} \qquad \nu^* = f(\text{geometry})$$

where E^* and ν^* are the effective Young's modulus and Poisson's ratio of the material with repeated cells, E_s and ρ_s are the solid material modulus and density, ρ^* is the relative density of the structure, C_E is an empirical constant typically comprised between 0.1 and 0.6, and n is a characteristic exponent that depends on the deformation mode (bending or stretching-dominated).

For general honeycomb materials, professor Gibson and engineer Ashby propose the following formulas [15], which are considered a milestone in cellular material investigation.

$$\frac{E_1}{E_s} = \left(\frac{t}{l}\right)^3 \cdot \frac{cos(\theta)}{(\frac{h}{l} + sin(\theta)) \cdot (sin^2(\theta))} \tag{2.2}$$

$$\frac{E_2}{E_s} = \left(\frac{t}{l}\right)^3 \cdot \frac{(\frac{h}{l} + sin(\theta))}{cos^3(\theta)} \tag{2.3}$$

$$G = E_s \cdot \left(\frac{t}{l}\right)^3 \cdot \frac{(\frac{h}{l} + sin(\theta))}{cos(\theta) \cdot (\frac{h}{l})^2 \cdot (2\frac{h}{l} + 1)} \tag{2.4}$$

$$\nu_1 = \frac{cos^2(\theta)}{(\frac{h}{l} + sin(\theta)) \cdot sin(\theta)} \tag{2.5}$$

$$\nu_2 = \frac{(\frac{h}{l} + sin(\theta)) \cdot sin(\theta)}{cos^2(\theta)} \tag{2.6}$$

In their standard notation:

- l corresponds to the length of the inclined wall, which can be geometrically derived considering the known parameters *cell height* and *angle*;
- h corresponds to the length of the straight wall, which was previously referred to as *cell length*;
- θ is the angle measured between the straight wall and the inclined strut, and it assumes complementary negative values for re-entrant configurations.

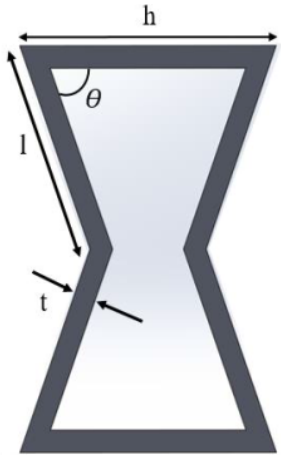

Figure 2.4: Possible convention for re-entrant honeycomb geometric parameters.

Starting from this theoretical basis, the fitting strategy implemented in this work aims to emulate the scaling logic of the Ashby–Gibson laws by expressing the simulated effective quantities E_{22} and ν_{21} as power-law functions of selected geometric predictors. The transformations introduced in the dataset (such as t^3, $1/l^3$, and $1/\sin\theta$) are designed to capture the nonlinear dependence of stiffness on the characteristic wall thickness t, the cell length that influences l, and the re-entrant angle θ, respectively. In classical re-entrant geometries, the modulus typically scales as seen in the formula due to the bending of slender inclined members. By including these suggested transformed terms, the regression model

will be more consistent with the expected physical trends. Additional parameters, such as the cell dimensions and the number of horizontal and vertical repetitions, are retained to account for boundary and size effects observed in finite structures.
To emulate the nonlinear geometric effects while preserving flexibility in model fitting, a polynomial regression approach was adopted. The `MATLAB` script `fitting.m` imports the input dataset `results_with_E_nu.csv`. A pre-processing step is performed to derive dimensionless geometric predictors. The key transformations were defined as:

$$l = \frac{cell\,height}{2\sin(\theta)}, \qquad \frac{cell\,length}{l} = \frac{h}{l}, \qquad \frac{t}{l}, \qquad \sin(\theta), \qquad \cos(\theta)$$

These combinations are physically motivated by the analytical expressions of beam bending and axial deformation in re-entrant lattices. The ratio t^3/l^3 captures the cubic dependence of bending stiffness on the slenderness ratio of the struts, while the trigonometric terms describe the geometric amplification or contraction of the deformation path as a function of the re-entrant angle. The parameters `n horizontal` and `n vertical` are also included to take into consideration the edge effects related to boundary conditions and the finite size of the models analyzed.

The fitting procedure employs the `MATLAB` `fitlm` function to perform robust linear regression.
For the elastic moduli E_{22}, the regressors were constructed directly from the closed-form analytical solutions provided by Gibson and Ashby, augmented with higher-order correction terms proportional to $(t/l)^2$ to account for rib stretching and shear deformation, as described by professors Masters and Evans [24]. This particular physics-informed approach led to exceptional correlations ($R^2 = 0.97$), with the presence of some minor corrective terms. The plotted results in Figure 2.5 show a tight alignment of the data around the $y = x$ line, confirming the model's capability to reproduce the response with good fidelity.
On the other hand, a critical behavior was observed when adopting the same strategy for the transverse Poisson's ratio ν_{21}. In the loading direction perpendicular to the vertical ligaments, the auxetic effect relies entirely on the flexural unfolding of the re-entrant corners. The FEM results clearly showed that this kinematic mechanism is extremely sensitive to the aluminum thickness: as the slender ratio increases, the nodes stiffen. The analytical formulas fail to capture the stiffening that prevents the folding mechanism, leading to a coefficient of correlation of $R^2 = 0.4$.

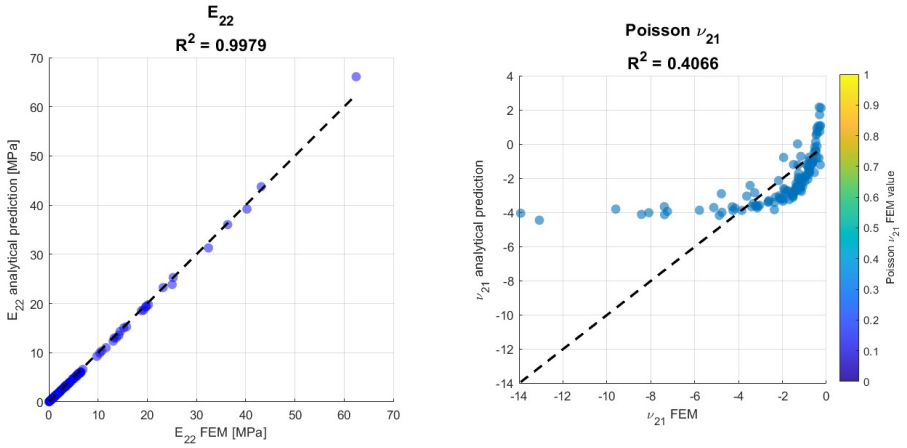

Figure 2.5: Results fitting for E_{22} and ν_{21} using Ashby-Gibson formulas and Masters-Evans corrections.

Consequently, a semi-empirical response surface model based on the fundamental dimensionless groups of the unit cell geometry was adopted. The new approach allowed for quadratic interactions between the terms, and the correlation improved to $R^2 = 0.85$ as shown in Figure 2.6.

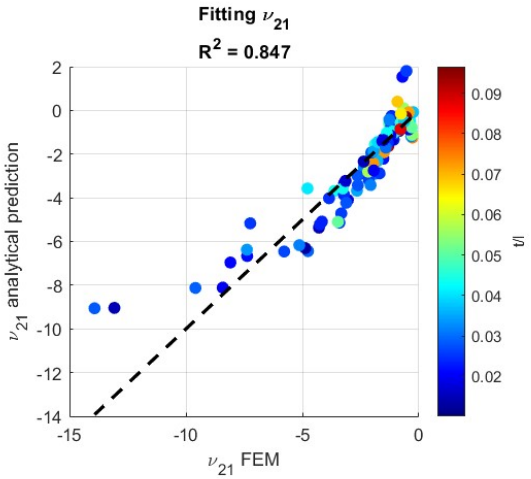

Figure 2.6: Semi-empirical approach to fit ν_{21} results.

Considering a new control set of ten parameters, it is immediate to verify the divergence of results attended, and calculated through `Abaqus`.

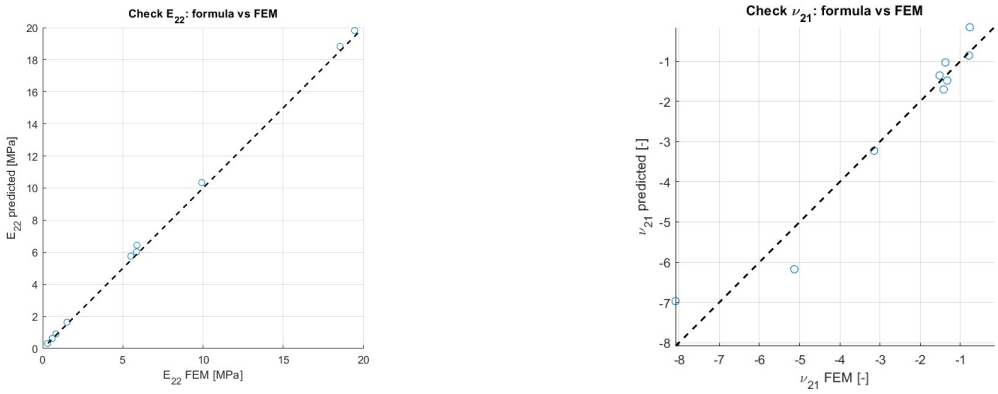

Figure 2.7: Overfitting check.

The checking procedure was performed for every different regression, but it will be demonstrated only for the most relevant cases.
The quality of the fit was evaluated using:

- the coefficient of determination (R^2),
- the mean absolute error (MAE).

In general, R^2 values are typically lower than those for E_{22} due to the higher sensitivity of Poisson's ratio to local geometrical fluctuations.
Both regression models have been exported as `MATLAB` objects (`model_poly_E22.mat` and `model_poly_nu21.mat`), ready for later reuse. For instance, given a complete set of parameters, it is now possible to calculate an approximation for E_{22} and ν_{21} without performing an expensive `Abaqus` analysis.
Based on the regression analysis, the predictive models for the elastic modulus E_{22} and Poisson's ratio ν_{21} are:

$$E_{22} = \left[1.415 \cdot 10^4 + 17.08N_x - 29.87N_y\right] \cdot \left(\frac{t}{l}\right)^3 \frac{\cos(\theta)}{(h/l + \sin(\theta))\sin^2(\theta)} \tag{2.7}$$

$$\begin{aligned} \nu_{21} = &- 6.15 - 2.33 \cdot \frac{\sin(\theta)(h/l + \sin(\theta))}{\cos^2(\theta)} + 687.97 \left(\frac{t}{l}\right)^2 \\ &+ 444.09 \cdot \frac{\sin(\theta)(h/l + \sin(\theta))}{\cos^2(\theta)} \cdot \left(\frac{t}{l}\right)^2 + 0.03N_x + 0.18N_y \end{aligned} \tag{2.8}$$

The regression analysis for E_{22} yielded a proportionality constant $C \approx 0.2$, that strongly deviates from the ideal unity value. This discrepancy reflects the higher compliance of the numerical model due to the combined influence of finite size effects and shear or node

deformations, which are completely neglected in the classical analytical derivation. The actual structural efficiency of the specific finite geometry analyzed compared to an ideal infinite structure is significantly lower.

2.2. Evaluation of the transverse Young's modulus E_{11} and Poisson's ratio ν_{12}

The workflow follows the same logic for the evaluation of E_{11} and the relative Poisson's ratio. Obviously, some changes are needed in the FEM model. The re-entrant honeycomb generation remains unchanged. The new mechanical test simulates a uniaxial compressive load applied along the global x-direction.
Once again, the 4 reference points play a fundamental role for loads and constraints:

- `RP3` is fully constrained by an `ENCASTRE` boundary condition;
- `RP2` is constrained in the y-direction to prevent lateral rigid-body motion;
- `RP1` is loaded in the positive x-direction with a 100 N compressive force.

Moreover, specific corner nodes are fixed in the z-direction to avoid rotations and out-of-plane motion. The equation imposed on `RP1` distributes the load to the left edge of the honeycomb.
A new `Python` extractor has been created to collect the displacement fields of interest: the vertical displacement component U_2 at `RP1` and `RP2` (displacement at `RP2` is for checking purposes only, since it is expected to be zero), and the horizontal displacement components U_1 at `RP3`.

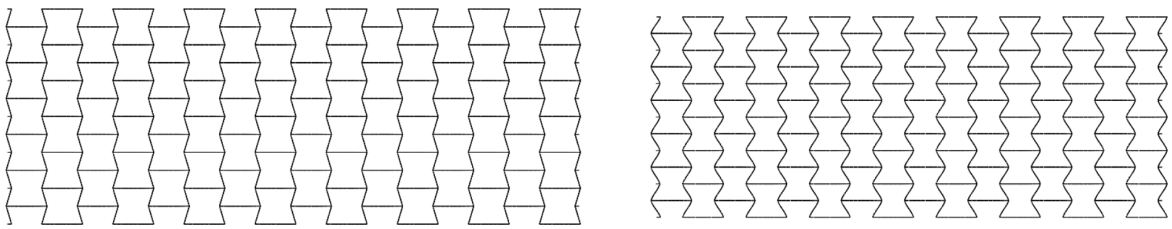

Figure 2.8: Example of undeformed and deformed structure (resulting from Job-3).

A new set of 200 configurations has been submitted for analysis, and 149 of them survived the geometric scanner and produced valid outputs. The data collected have been post-processed in MATLAB in the aforementioned manner, simply adapting the formulas to the present case.

For each valid configuration, the effective cross-sectional area subjected to loading is obtained as:

$$A_{YZ} = \text{model height} \cdot \text{extrusion width}$$

Given the applied vertical load $F = 100$ N, the average normal stress in the loading direction is calculated as:

$$\sigma_{11} = \frac{F}{A_{YZ}}$$

The axial and transverse strains are evaluated as follows:

$$\varepsilon_{22} = \frac{\Delta y}{\text{model height}}, \qquad \varepsilon_{11} = \frac{\Delta x}{\text{model length}}$$

where $\Delta y = \max(|U_2|)$ is the maximum vertical displacement and $\Delta x = \max(|U_1|)$ is the maximum horizontal displacement. Using these quantities, the effective Young's modulus in the loading direction and the in-plane Poisson's ratio are computed as follows:

$$E_{11} = \frac{\sigma_{11}}{\varepsilon_{11}}, \qquad \nu_{12} = -\frac{\varepsilon_{22}}{\varepsilon_{11}}$$

The results are stored in the final output file `results_with_E_nu.csv`, ready for fitting post-processing.
Following the previous approach, the most relevant dependencies have been included as predictors for the `MATLAB` function `fitlm`, with suggested terms, in order to better evaluate the role played by each varying parameter.

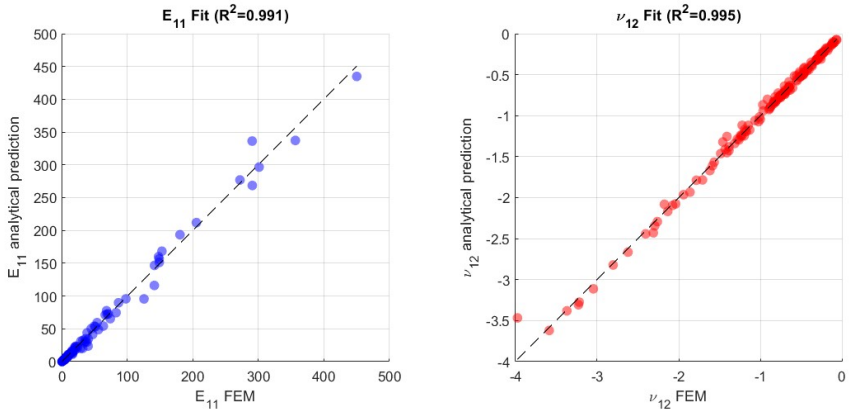

Figure 2.9: Results fitting for E_{11} and ν_{12} using Ashby-Gibson formulas and Masters-Evans corrections.

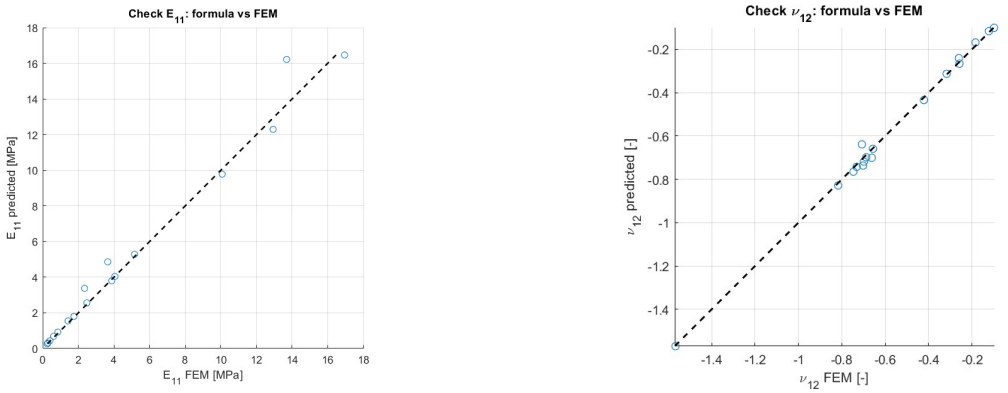

Figure 2.10: Overfitting check.

The following approximate formulas were obtained.

$$E_{11} = \left(2.05 \cdot 10^4 \cdot +6.43 \cdot 10^5 \cdot \left(\frac{t}{l}\right)^2\right) \cdot \left(\frac{t}{l}\right)^3 \frac{h/l + \sin(\theta)}{\cos^3(\theta)} - \mathcal{O}(N_{cells}) \tag{2.9}$$

A crucial physical insight is evident: the coefficient for the thickness correction term is one order of magnitude larger than the base bending term. This indicates that when loaded along the vertical ligaments, the stiffness is dominated by the axial stretching of the ribs rather than their bending. The Masters-Evans correction term captures this effect, neglected by the classical bending-only theory.

$$\nu_{12} = -0.036 + \left(0.98 \cdot \left(\frac{t}{l}\right)^2 - 8.36 \cdot \left(\frac{t}{l}\right)^2\right) \cdot \frac{(h/l + \sin(\theta))\sin(\theta)}{\cos^2(\theta)} - 12.05 \tag{2.10}$$

In strong contrast to the transverse direction (ν_{21}), the parallel Poisson's ratio ν_{12} follows the analytical geometric kinematics almost perfectly. The negative coefficients associated with the $(t/l)^2$ terms quantify the inhibition of the auxetic mechanism due to the structural stiffening of the nodes and shear deformation as the relative density increases, but without the behavior observed in the perpendicular direction.

2.3. Evaluation of shear modulus G_{12}

The numerical estimation of the in-plane shear modulus G_{12} has been performed following the same parametric path described previously, with appropriate modifications. In this case, the aim was to impose a shear deformation on the upper surface of the re-entrant honeycomb structure. The population of 129 elements that successfully completed the

analyses for E_{22} has been adopted for the assessment of the shear modulus. The loading sequence was adapted to represent a pure shear test: a horizontal force of 100 N was applied at the top reference point (`RP1`) along the global x-direction, while the bottom reference point (`RP2`) was fully constrained (`ENCASTRE`). Moreover, the constraint equations between `RP3`, `RP4`, and the left and right edges, respectively, have been removed since the edges must be free to deform. Finally, a uniform in-plane shear strain γ_{12} can be observed across the structure.

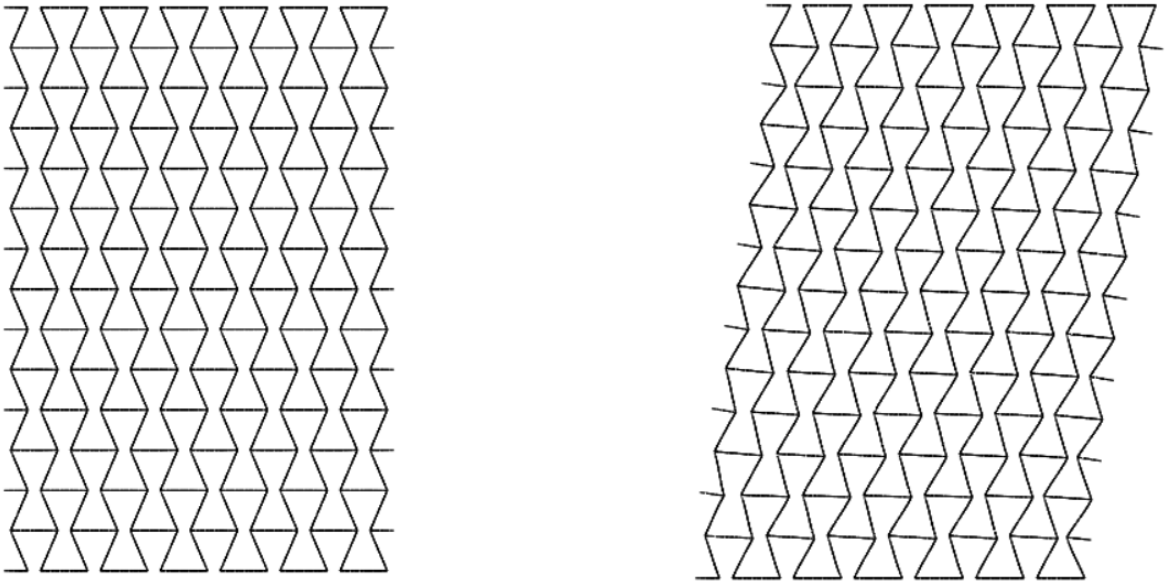

Figure 2.11: Example of undeformed and deformed structure (resulting from Job-8).

The reaction forces and relative displacements recorded at the reference points were extracted to compute the effective shear modulus as follows:

$$G_{12} = \frac{\tau_{12}}{\gamma_{12}} = \frac{\frac{F_x}{A_{XZ}}}{\frac{\Delta u_x}{\text{model height}}}$$

where F_x is the total horizontal reaction at the top boundary and Δu_x is the relative tangential displacement between the top and bottom edges. Note that since `RP2` is fully constrained, the bottom edge will not move.

Once the G_{12} values have been calculated, a new approach has been adopted to capture the parameters influence. It all starts with the theoretical formulation proposed by Ashby-

Gibson, which states:

$$G_{12} = k\left(\frac{t}{l}\right)^{3} \cdot \left(\frac{h}{l} + \sin(\theta)\right) \cdot \left(\cos(\theta) \cdot \left(\frac{2h}{l} + 1\right)\right)^{-1} \cdot \left(\frac{h}{l}\right)^{-2} \tag{2.11}$$

where it is important to remind that the parameters are: t the wall thickness, l the length of the inclined struts, h the length of the cell straight edge, and θ the negative re-entrant angle. The general formulation

$$G_{12} = k\left(\frac{t}{l}\right)^{\alpha} \cdot \left(\frac{h}{l} + \sin(\theta)\right)^{\beta} \cdot \left(\cos(\theta) \cdot \left(\frac{2h}{l} + 1\right) \cdot \left(\frac{h}{l}\right)^{2}\right)^{\gamma} \tag{2.12}$$

with parametric exponents, it is adopted. The data collected are fitted to evaluate how close the exponent is compared to the one prescribed in the literature. The relationship is linearized by applying the logarithm to both sides, so that a standard multiple linear regression model can be adopted. After fitting, the predicted values of the shear modulus in the original scale are simply obtained through exponentiation. Again, the accuracy of the model is evaluated through the coefficient of determination R^2 and the mean absolute error (MAE). The experimental constant $k \approx 139$ GPa is higher than the modulus of the base material. In the FEM model, the effective flexible length of the ribs is shorter than l, resulting in a significantly stiffer response (scaling with l^{-3}) which the regression captures by increasing the proportionality constant. The resulting exponents are now presented.

Table 2.1: Estimated parameters of the model for the shear modulus G_{12}, R^2=0.986

Parameter	**Expected value**	**Estimated value**
Exponent on relative thickness α	3	2.9822
Exponent at numerator β	1	1.1182
Exponent at denominator γ	-1	-1.8578

The coefficient α is captured perfectly, demonstrating once more that bending is the primary deformation mechanism. However, the geometric shape exponents β and γ deviated from the analytical integers. This suggests that secondary mechanisms, such as rib shear deformation, introduce a distortion in the geometric dependency that a pure power-law cannot fully capture. To maintain physical consistency, the final constitutive model will include an additive correction term (Masters and Evans approach) to explicitly account for the shear contribution.

The alternative equation, derived from the usual regression method, is presented.

$$G_{12} \approx \left[\left(\frac{t}{l}\right)^3 \frac{\frac{h}{l}+\sin\theta}{\cos\theta\left(\frac{h}{l}\right)^2\left(1+2\frac{h}{l}\right)}\right]\left[2.28\times10^5+8.91\times10^6\left(\frac{t}{l}\right)^2-3.17\times10^3 N_x\right] \tag{2.13}$$

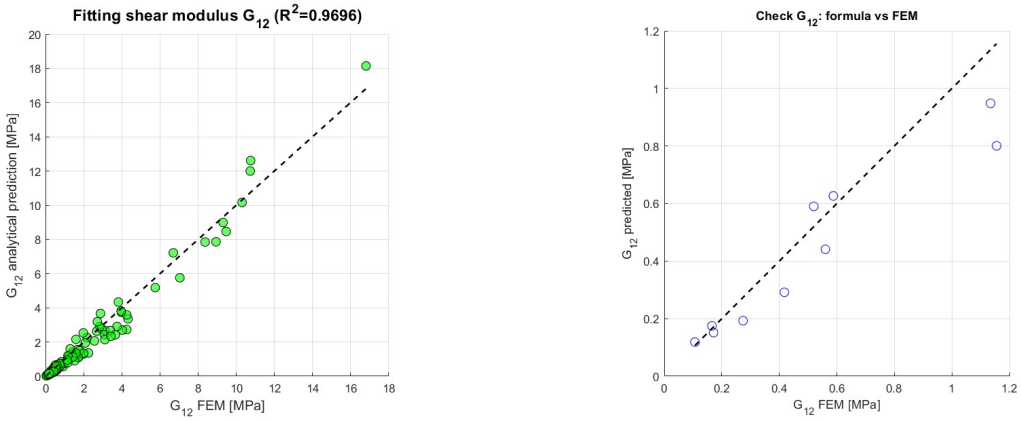

Figure 2.12: Results fitting for G_{12} using Ashby-Gibson formulas and Masters-Evans corrections. Overfitting check.

2.4. Aluminum skins

The nude re-entrant honeycomb has been assessed. Many different design combinations have been studied: the range of stiffness achievable is extended, but still limited. Due to its geometric nature, the structure is very easy to deform. The auxetic behavior is the subject of this analysis, but, at the present moment, the range of stiffness would be insufficient for performing a structural role or during an impact event. Honeycomb structures in aerospace applications can be employed as the core of a sandwich structure, located between two skins. Adding containment skins drastically increases bending stiffness. On the other hand, total weight inevitably increases; however, the resulting gain in stiffness is far greater.

In the present paragraph, sandwich panels are studied: two aluminum thin skins contain the re-entrant honeycomb core.

Aluminum panels constitute a new additional parameter called `skin_thickness`. `LHS.m`, the population generator, chooses values between 0.4 mm and 1.7 mm. They are modeled as simple plates and meshed as shell elements.

The re-entrant honeycomb is newly generated, though the identical logic from the previous paragraphs is followed.

All the scripts need to be updated to include the two aluminum skins.
The new `generate_skins.m` script generates two planar layers of shell elements parallel to the XY-plane. The back skin is positioned at the minimum z-coordinate of the honeycomb (z_{min}), while the front skin is positioned at the maximum z-coordinate (z_{max}). Each skin is meshed using `S4R` elements and constitutes an independent instance. To ensure full continuity between the core and the skins, two `*TIE` constraints are created:

- honeycomb nodes at z_{min} are linked to the back `SURFACE`, created on the back skin;
- honeycomb nodes at z_{max} are linked to the front `SURFACE`, created on the front skin.

In this way, perfect bonding is guaranteed, avoiding relative displacement or separation when the structure is loaded.

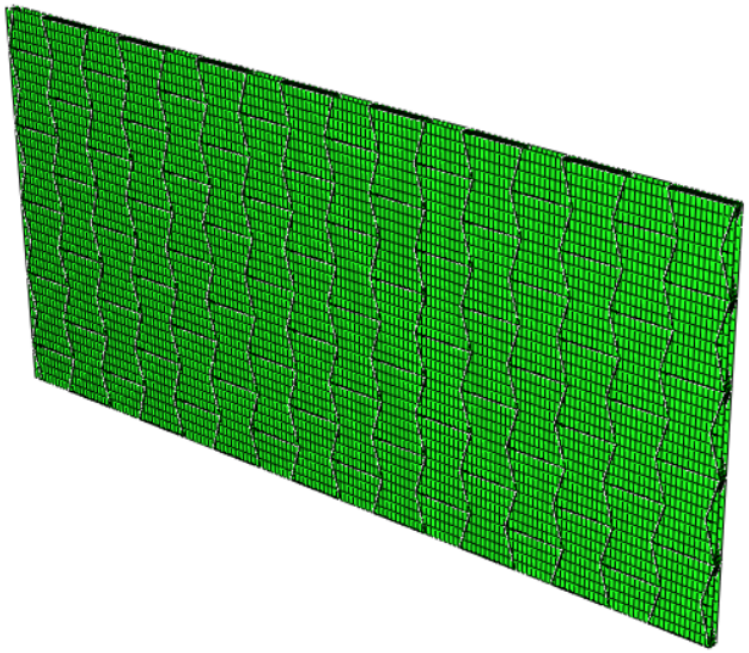

Figure 2.13: Assembly re-entrant honeycomb and skins.

2.4.1. Evaluation of the transverse Young's modulus E_{22} and Poisson's ratio ν_{21}

The evaluation of Young's modulus E_{22} and Poisson's ratio ν_{21} follows the same steps seen in Paragraph 2.1, with some small differences:

- the load applied at `RP1` is now increased to a magnitude of 500 N;
- the cross-sectional area A_{XZ} must take into account the thickness of the two skins.

It is important to underline that the actual magnitude of the load applied it is not relevant in static assessment. A total of 200 brand new analyses were carried out, and 132 of them were completed successfully.

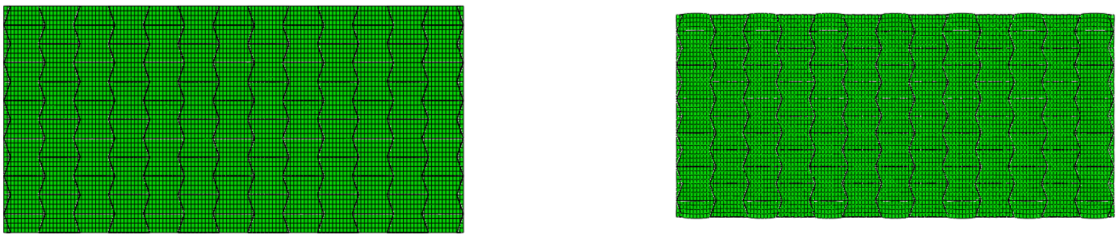

Figure 2.14: Example of undeformed and deformed structure (x10^5 scale factor), Job-10.

As expected, the computed displacements will result in very small values due to the presence of the skins.
The question naturally arises: are the skins the only ones responsible for carrying the load?
To evaluate the role played by each part, a comparison is performed between the results obtained from the `Abaqus` analyses described earlier and hand-made calculations considering only the two skins since their stiffness is dominant. The `MATLAB` script `analytical_confrontation.m` performs a direct comparison between the two approaches. Given the applied load of $F = 500\,\mathrm{N}$, the analytical axial stress acting on the two aluminum skins is obtained as follows:

$$\sigma_{\text{analytical}} = \frac{F}{2\,\text{width} \cdot t_{\text{skin}}}$$

where the factor of two accounts for the load sharing between both skins. Assuming linear elastic behavior of the aluminum ($E_{Al} = 70$ GPa), the axial strain is:

$$\varepsilon_{\text{analytical}} = \frac{\sigma_{\text{analytical}}}{E_{Al}}$$

The total axial displacement of the panel can be expressed as:

$$\Delta l_{\text{analytical}} = \varepsilon_{\text{analytical}} \cdot \text{height}$$

Finally, the analytical and numerical displacements are compared for all configurations:

$$\text{error}_{\%} = \frac{\Delta l_{\text{analytical}} - \Delta y_{\text{Abaqus}}}{\Delta l_{\text{analytical}}} \times 100$$

Although the analytical estimation based on the sole skins provides results that agree with the Abaqus simulations, the comparison reveals a non-negligible difference. The average error is around 13%, which overcomes a reasonable 5% tolerance. This deviation proves that the honeycomb core plays a minor, but not insignificant, structural role in the overall stiffness.
An extract of the first results is shown in Table 2.2.

Table 2.2: Displacement comparison.

WIDTH (mm)	**HEIGHT** (mm)	**SKIN THICKNESS** (mm)	E_{22} (MPa)	$\Delta l_{analytical}$ (µm)	Δy_{Abaqus} (µm)	**ERROR** (%)
885.59	427.56	0.54474	7584.7	3.1653	2.87	9.33
567.92	199.55	1.1817	11802	1.0619	1.204	-13.38
421.39	448.89	1.0796	15539	3.5239	2.819	20.00
636.58	415.65	0.44603	7908.5	5.2282	3.79	27.51
1057.8	299.41	1.3098	13726	0.77179	0.817	-5.86
861.67	323.46	1.4877	14582	0.90112	0.992	-10.08
1344.6	491.02	0.87968	10365	1.4826	1.498	-1.04

Once the results from the `Abaqus` simulations have been extracted, fitting can be performed. The usual logic is adopted and adapted by adding regressors for the skins, more specifically: skin thickness, its powers, and interactions with the other parameters. The total stiffness is derived from the superposition of the bending stiffness of the core and the membrane stiffness of the skins. A `fitlm` linear model is adopted after testing a `stepwise` model that tends to be extremely specific for the database used to train it.

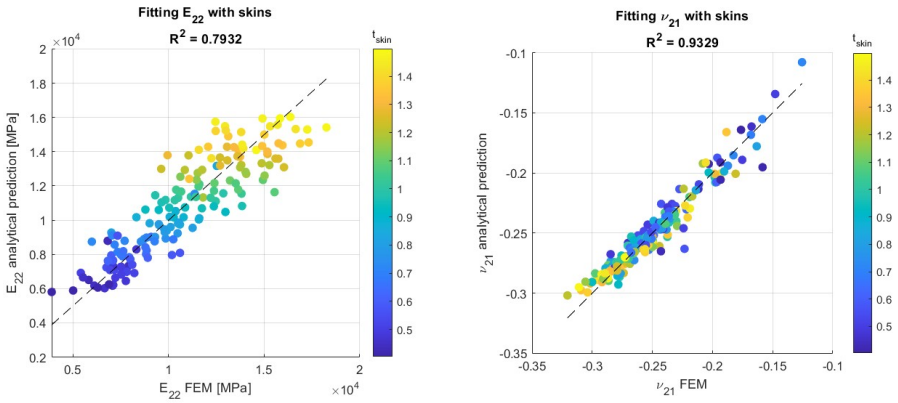

Figure 2.15: Results fitting for E_{22} and ν_{21} for re-entrant honeycomb with skins.

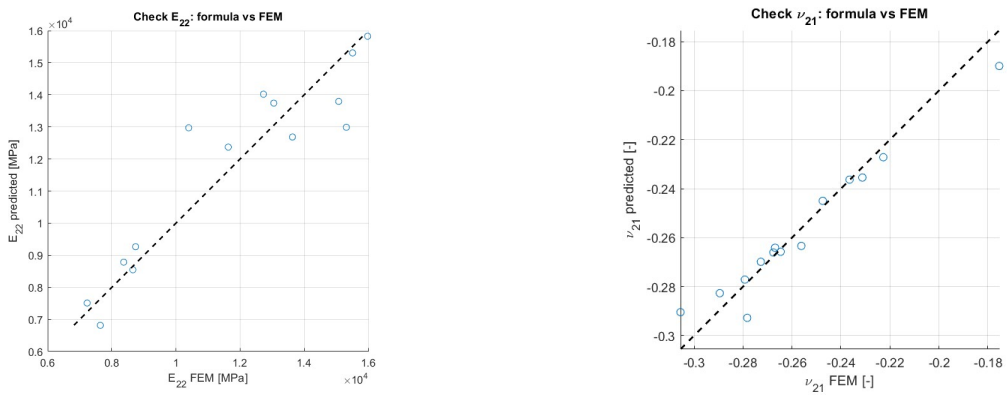

Figure 2.16: Overfitting check.

The resulting semi-empirical constitutive law is:

$$E_{22} \approx (3.00 - 2.97 \cdot t_{skin}) \cdot 10^6 \cdot \left(\frac{t}{l}\right)^3 \cdot \frac{cos(\theta)}{(\frac{h}{l} + sin(\theta)) \cdot (sin^2(\theta))} + 9442.5 \cdot t_{skin} \quad (2.14)$$

A non-trivial interaction mechanism is revealed: while the positive linear term associated with t_{skin} represents the expected stiffness contribution, the negative interaction term indicates that the skins also constrain the rotation of the core nodes at the interface. This effect increases when the skin thickens, and the result is a progressive inhibition of the ideal unfolding mechanism of the re-entrant cells.

The analysis of Poisson's ratio ν_{21} demonstrated a significant improvement in predictability compared to the bare core configuration. For instance, the addition of the aluminum skins stabilizes the kinematic response of the structure. The behavior can be described as

a competition between the auxetic tendency of the core and the conventional contraction of the panels.

$$\nu_{21} \approx -0.28 + 2.19 \cdot \left(\frac{t}{l}\right) - 1.13 \cdot \left(\frac{t}{l} \cdot t_{skin}\right) \tag{2.15}$$

The regression reveals a complex interplay: the baseline auxetic behavior is counteracted by the skin term. However, the interaction negative term highlights the stabilizing role of the face sheets. Rather than directly increasing the auxeticity, the skins mitigate the performance loss caused by thicker ligaments.

2.4.2. Evaluation of the shear modulus G_{12}

The presence of skins constrains the relative motion of the cell walls, resulting in a significant increase in shear stiffness. For this reason, new analyses have been conducted to assess the shear modulus G_{12}.
The structures generated by the new scripts, which include skins, are subjected to the same load and constraints used to assess G_{12} for the sole re-entrant honeycomb. Skins and core communicate through a `*TIE` constraint.
A comparison between a structure and its deformed shape is shown in Figure 2.17.

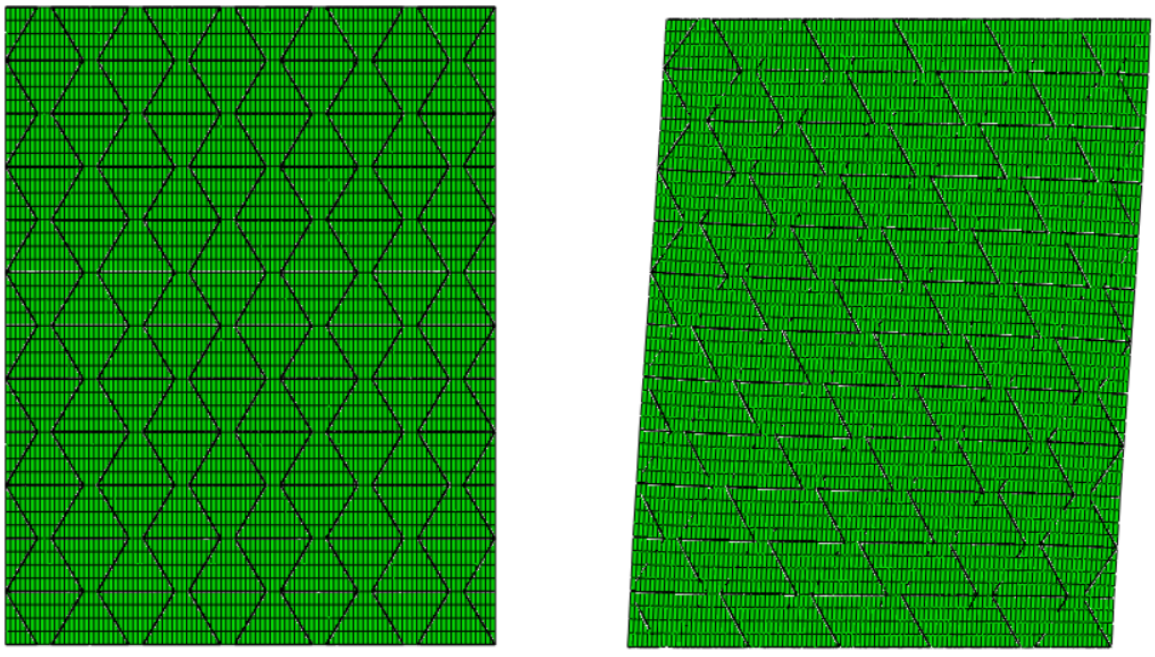

Figure 2.17: Example of undeformed vs deformed structure (x10^5 scale factor), Job-34.

The results have been post-processed, and a new regression function needs to be found, including the new regressor: skin thickness. The shear modulus is modeled using the Rule

of Mixtures, which states that for sandwich panels subject to shear loads [32]:

$$G_{12}^{eff} \approx G_{12}^{Al} \cdot \frac{2t_{skin}}{H_{tot}} \tag{2.16}$$

The total effective stiffness is defined as the superimposition of two contributions: the skins, which depend on their thickness, and the core topology.

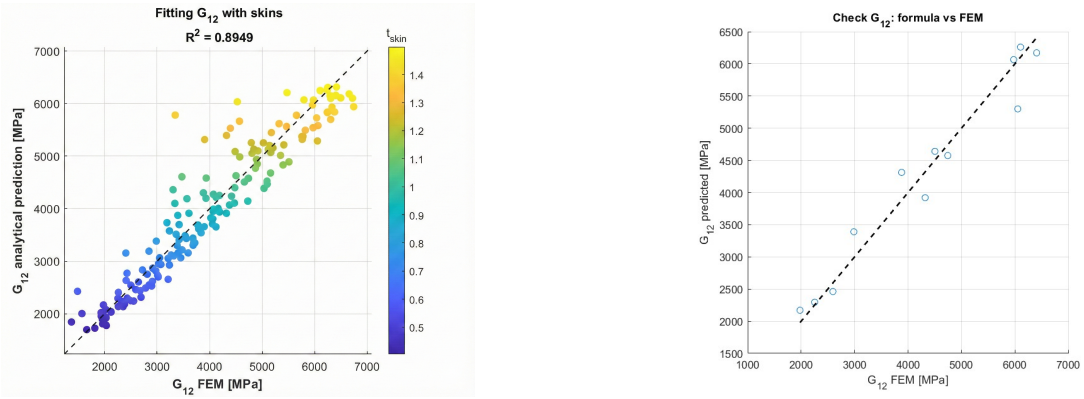

Figure 2.18: Results fitting for G_{12} for re-entrant honeycomb with skins.

$$G_{12} = 4203 \cdot t_{skin} + 1.67 \times 10^6 \cdot \left[\left(\frac{t}{l} \right)^3 \frac{\frac{h}{l} + \sin\theta}{\cos\theta \left(\frac{h}{l} \right)^2 \left(2\frac{h}{l} + 1 \right)} \right] \tag{2.17}$$

Overall, the shear modulus is governed entirely by skin thickness. While the positive coefficient for the geometric core term validates the physical consistency of the modified Gibson-Ashby model, its quantitative contribution is practically negligible. For instance, very low values of shear modulus were observed in Paragraph 2.3: re-entrant topology is inherently compliant in shear.

2.5. Foam filler

The structure becomes more articulated with the introduction of viscoelastic polyurethane foam inside the honeycomb cells. Very often, auxetic material applications include foam as a filler. In fact, foam enhances energy absorption and damping capabilities while stabilizing the deformation of the cells and preventing premature buckling. The final aim of this particular material combination is to improve crashworthiness by providing a more controlled and progressive collapse so that the accelerations transmitted to occupants are reduced.

The original `function_rhc_generator` already contained additional information: it de-

termines the position of the foam layers to be used later in the `*ASSEMBLY` module.
The actual 3D foam components are generated through the function `foam_mesh_generator`. The former builds a full foam block from hexahedral `C3D8R` elements, with nodes placed on a regular grid that is later transformed to match the re-entrant cell shape through geometric projection based on the re-entrant angle. The example of an orphan mesh generated in `MATLAB` and imported into `Abaqus/CAE` is shown in Figure 2.19.

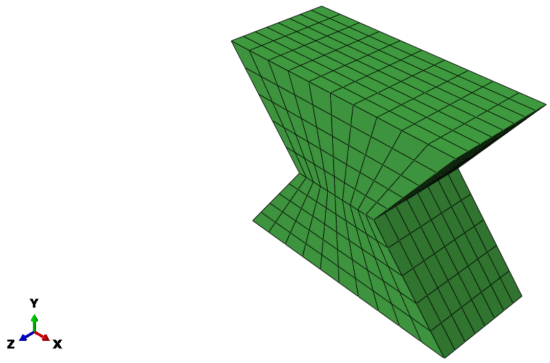

Figure 2.19: Foam (*PART).

An additional `half_foam_mesh_generator` is necessary to model the foam that will fill the half hourglasses at the top and bottom of the honeycomb. The function calls the previous one and simply truncates the full foam along its midplane. The result is shown in Figure 2.20 with an example of a general `main.inp` imported into the `CAE`.

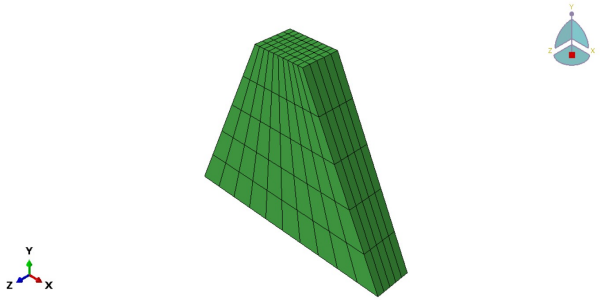

Figure 2.20: Half foam (*PART).

Both foams share the same `*MATERIAL` definition: `CONFOR CF45M` is adopted, a commercial open-cell polyurethane foam widely used in aerospace and protective applications because of its high energy absorption and slow recovery characteristics [1]. In order to consider this behavior, the Abaqus `LOW DENSITY FOAM` material model definition is adopted: it takes into account the nonlinear compressive response, strain-rate dependency, and volumetric

strain effects.
The foam density is set to $\rho = 9.9851 \times 10^{-11}$ tonne/mm^3.
The mechanical response of the material is described through uniaxial test data in both tension and compression. Each data block provides the engineering strain, nominal stress, transverse strain, and strain rate, so that `Abaqus` is able to interpolate the response over a wide range of deformation. `LATERAL STRAIN DATA = YES` enables a more accurate reproduction of the Poisson-like response of the material under large compressive deformation, which will be the objective of the study in Chapter 4. Other parameters focus on the tensile response and failure modality, but they will not be useful for the analyses performed in this work.
In the `main.m` script, both full and half foam are defined as `*PART`. While defining the element sets, the new function `write_contact_set` automatically identifies and groups all the interface nodes between the honeycomb and each individual foam. In the `*ASSEMBLY` module, two node-based surfaces are generated: `HC_SURF_ASM` for all the interface nodes of the re-entrant honeycomb and `FOAM_SURF_ASM` for all the interface nodes of all the foams and half foams generated, which are then linked through a single `*TIE` constraint without adjustment. In this way, no relative motion, debonding, or friction is expected, and kinematic continuity is ensured.
Finally, in the `*ASSEMBLY` module, one instance for each foam and half foam, filling a specific cell, is created. The precise coordinates to position each instance are provided by `foampoints`, `upperfoam`, and `lowerfoam` arrays generated earlier, ensuring correct alignment.

The usual analyses are performed to evaluate the in-plane elastic properties E_{11}, ν_{12}, E_{22}, ν_{21}, and G_{12}. For each case, the same modeling logic, mesh generation, load, and boundary condition strategies described in the previous sections are applied, obviously using the new configuration that includes foam. It is important to highlight a small difference in the `.inp` file: in the `*STEP`, `nlgeom` is set to `YES`, so that geometric nonlinearities are accurately considered during the simulations.

2.5.1. Evaluation of the transverse Young's modulus E_{11} and Poisson's ratio ν_{12}

Avoiding redundancy, in the following subsections, only the main results and approximate formulas are presented.
A horizontal compressive force of 500 N is applied at the reference point `RP3`.
The Young's modulus E_{11} was modeled using a physics-enforced regression approach.

Preliminary unrestricted models produced severe multi-collinearity, causing an unrealistic value for the foam regressor. For this reason, the baseline stiffness of the polyurethanic foam ($E_{foam} = 27\,\text{MPa}$) was treated as a known constant. Assuming a superposition of the face sheets and the re-entrant contributions, the regression was forced through the origin of the net stiffness:

$$E_{11} = E_{FEM} - E_{foam} \tag{2.18}$$

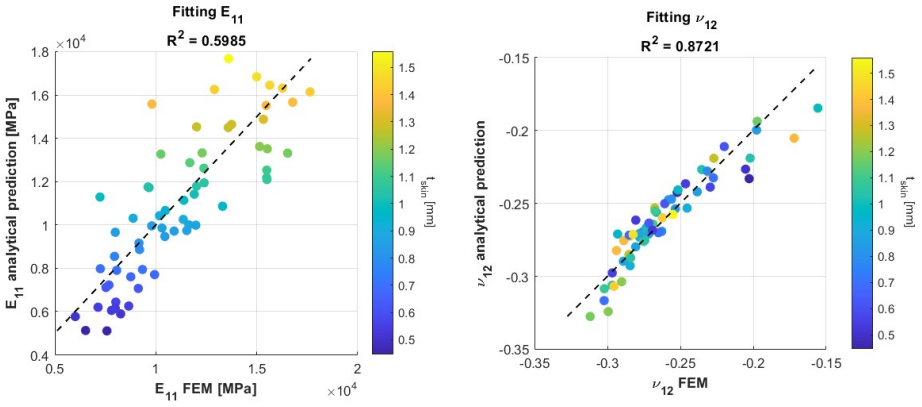

Figure 2.21: Results fitting for E_{11} and ν_{12} for foam-filled re-entrant honeycomb with skins.

$$E_{11} \approx 27 + 11320 \cdot t_{skin} + 5.72 \times 10^4 \cdot \left(\frac{t}{l}\right)^3 \frac{h/l + \sin(\theta)}{\cos^3(\theta)} \tag{2.19}$$

The skin thickness coefficient is almost identical to that found for the transverse direction (11 320 MPA/mm vs 11 256 MPA/mm), with a discrepancy of less than 0.6%. The geometric contribution of the re-entrant skeleton proved to be statistically negligible (*p-value* ≈ 0.83): the core is inherently more compliant in the longitudinal direction, so when stiff face sheets and foam are added, its contribution is overshadowed by the skin-foam system.

$$\begin{aligned} \nu_{12} \approx &- 0.105 - 0.036 \cdot \left(\frac{h}{l}\right) + 0.863 \cdot \left(\frac{t}{l}\right) \\ &+ 0.080 \cdot \sin\theta - 0.047 \cdot t_{skin} - 0.003 \cdot N_x \end{aligned} \tag{2.20}$$

The model confirms that the wall slenderness ratio remains the primary geometric driver for positive values, counteracted by the interaction with the skins. The lower coefficient

of determination reflects the complex interactions and inherent sensitivity to boundary conditions and local deformations in foam-filled structures.

2.5.2. Evaluation of the transverse Young's modulus E_{22} and Poisson's ratio ν_{21}

A vertical compressive force of 500 N is applied at reference point `RP1`, and the system of constraints is the same as described in Paragraph 2.4.1 during the evaluation of the transverse Young's modulus E_{22} of the re-entrant honeycomb with skins.

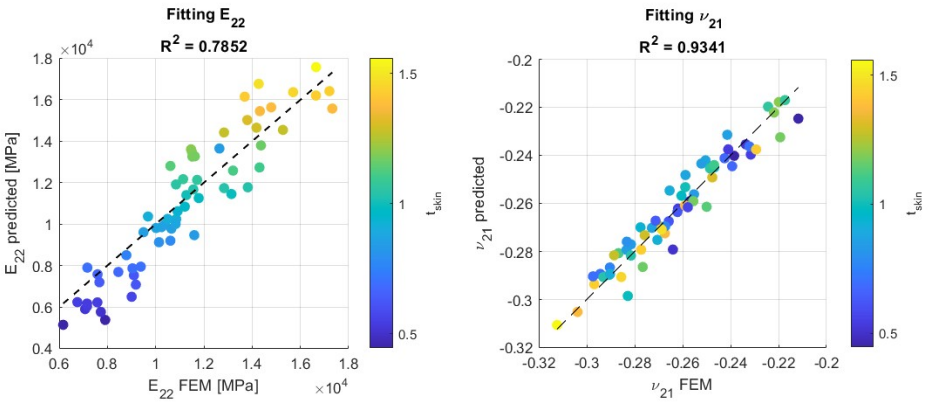

Figure 2.22: Results fitting for E_{22} and ν_{21} for foam-filled re-entrant honeycomb with skins.

The resulting model shows good accuracy and yields physically consistent positive coefficients for all components. In particular, Equation 2.21 demonstrates that the coefficient related to skin thickness shows perfect agreement with the aforementioned Rule of Mixtures, validating the FEM analyses.

$$E_{22} \approx 27 + 11256 \cdot t_{skin} + 5.88 \times 10^5 \cdot \left[\left(\frac{t}{l}\right)^3 \frac{\frac{h}{l} + \sin\theta}{\cos\theta \left(\frac{h}{l}\right)^2 \left(2\frac{h}{l} + 1\right)} \right] \tag{2.21}$$

$$\nu_{21} \approx -0.3215 + 0.0248 \cdot \left(\frac{h}{l}\right) + 2.0894 \cdot \left(\frac{t}{l}\right) - 0.97 \cdot \left(\frac{t}{l} \cdot t_{skin}\right) \tag{2.22}$$

The first constant term in equation 2.22 implicitly captures the contribution of the foam,

elevating the initial auxeticity to less negative values. The linear geometric terms highlight that higher wall slenderness inhibits the bending required for the auxetic mechanism to function. Finally, the interaction term describes the mechanical coupling of the restraining effect of the skins and the re-entrant relative density.

2.5.3. Evaluation of the shear modulus G_{12}

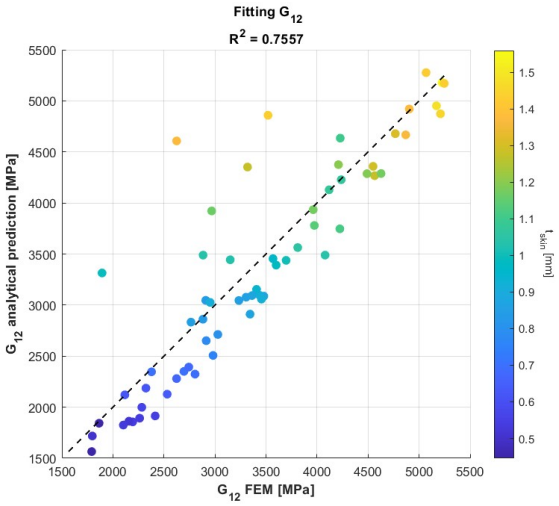

Figure 2.23: Results fitting for G_{12} for foam-filled re-entrant honeycomb with skins.

$$G_{12} \approx 10.8 + 3313 \cdot t_{skin} + 3.95 \times 10^6 \cdot \left(\frac{t}{l}\right)^3 \tag{2.23}$$

The baseline resistance is provided by the foam matrix (10.8 MPa). The face sheets provide the dominant contribution, even though the coefficient is approximately 20% lower than the theoretical prediction due to the *shear lag effect* arising from the finite shear compliance of the core, which prevents a perfectly uniform stress transfer across the cross-section.

Finally, the most important result is that the re-entrant lattice actively participates in resisting shear loads when supported by the foam filler, which acts as an elastic foundation that constrains cell wall bending.

2.6. Additional parameter: core thickness

Despite the primary focus of the present Chapter being on the in-plane elastic properties of the auxetic material, the core thickness plays an important role in the overall structural response. For this reason, considering a reasonable limit for the total panel thickness of

30 mm and knowing that skins can be at most 1.5 mm thick, a new parameter is introduced in the `LHS.m` generator as an eighth variable. Its name in the scripts is indicated as `z_thickness` or `z_core`, and it represents exclusively the core thickness. It will vary between 5 and 27 mm.
At this stage, all previous analyses are repeated to evaluate elastic moduli, Poisson's ratio, and shear modulus in two scenarios: the core with skins and the core with skins filled with polyurethane foam.

2.6.1. Evaluation of the transverse Young's modulus E_{22} and Poisson's ratio ν_{21} for the re-entrant honeycomb with skins

The analytical model for the equivalent compressive stiffness E_{22} adopts the `Membrane Theory` approach [32], which postulates that the in-plane rigidity of a sandwich panel is governed by the superposition of its constituent layers, weighted by their respective volume fractions. Accordingly, the regression model is created to depend explicitly on the relative density of the face sheets (ϕ_{skin}) and the core (ϕ_{core}):

$$\phi_{skin} = \frac{2t_{skin}}{H_{tot}}, \quad \phi_{core} = \frac{z_{core}}{H_{tot}} \tag{2.24}$$

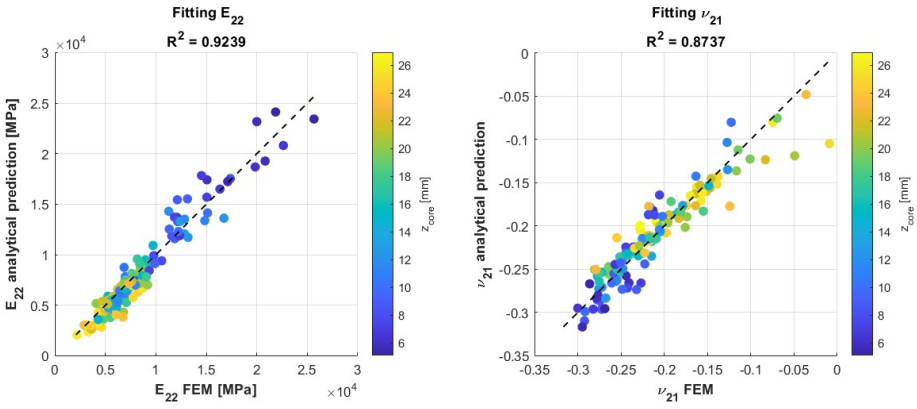

Figure 2.24: Results fitting for E_{22} and ν_{21} for re-entrant honeycomb with skins.

$$E_{22} = 67664 \cdot \phi_{skin} + 9.63 \times 10^5 \cdot \phi_{core} \cdot \left[\left(\frac{t}{l} \right)^3 \frac{\frac{h}{l} + \sin\theta}{\cos\theta \left(\frac{h}{l} \right)^2 \left(2\frac{h}{l} + 1 \right)} \right] \tag{2.25}$$

The regression coefficient for the skin volume fraction aligns remarkably well with the standard Young's modulus of aluminum. This indicates that the FEM model correctly scales the stiffness based on the effective cross-sectional area of the skins, regardless of the total panel thickness.

$$\nu_{21} \approx -0.258 + 0.015 \cdot \left(\frac{h}{l}\right) + 3.513 \cdot \left(\frac{t}{l}\right) - 0.205 \cdot t_{skin} + 0.0047 \cdot z_{core} \tag{2.26}$$

It is revealed that the assumption that 3D sandwiches behave purely like 2D extrusions is not valid. Thicker panels exhibit slightly less auxetic response compared to thinner panels. Although the dominant terms remain wall slenderness and cell aspect ratio.

2.6.2. Evaluation of the shear modulus G_{12} for the re-entrant honeycomb with skins

The shear modulus analysis demonstrates that the only dominant contribution is that of the skins. The core contribution was statistically negligible ($p > 0.5$): this confirms that the re-entrant skeleton provides no significant resistance to shear deformation in the absence of a supporting foam filler. Considering $\phi_{skin} = \frac{2t_{skin}}{z_{core}+2t_{skin}}$, the model approximates:

$$G_{12} \approx 28111 \cdot \phi_{skin} \tag{2.27}$$

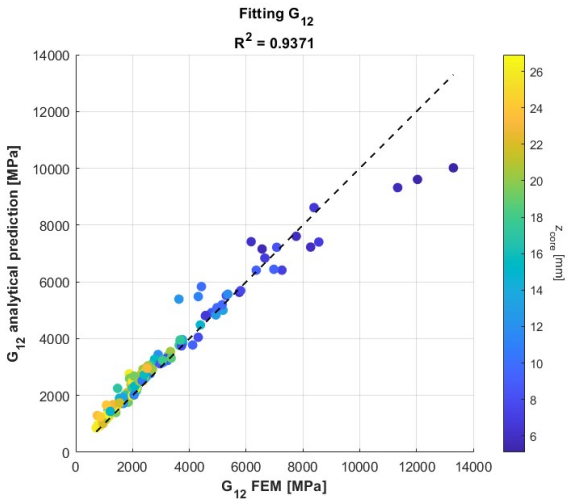

Figure 2.25: Results fitting for G_{12} for re-entrant honeycomb with skins.

The correlation with the theoretical shear modulus of aluminum is strong, with a deviation of less than 7%. Moreover, increasing the core thickness dilutes the skin volume fraction,

causing a direct decrease in G_{12}.

2.6.3. Evaluation of the transverse Young's modulus E_{22} and Poisson's ratio ν_{21} for the foam-filled re-entrant honeycomb with skins

The baseline foam contribution has been fixed.

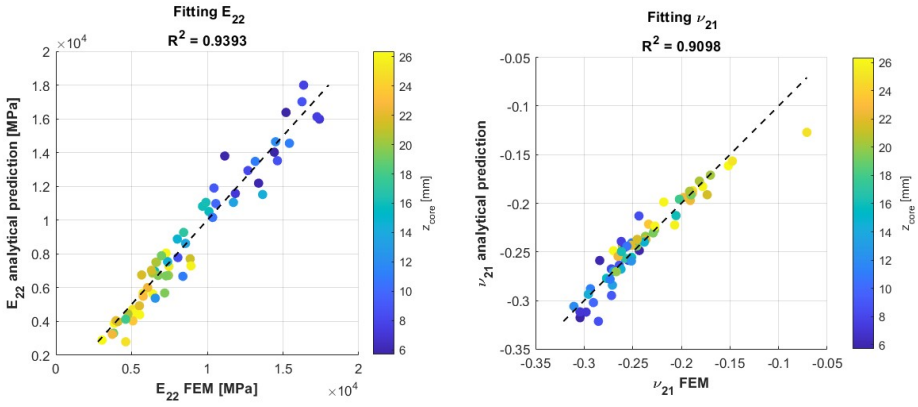

Figure 2.26: Results fitting for E_{22} and ν_{21} for foam-filled re-entrant honeycomb with skins.

$$E_{22} \approx 70807 \cdot \phi_{skin} + 27 \cdot \phi_{core} + 5.62 \times 10^5 \cdot \phi_{core} \cdot \left[\left(\frac{t}{l} \right)^3 \frac{\frac{h}{l} + \sin\theta}{\cos\theta \left(\frac{h}{l} \right)^2 \left(2\frac{h}{l} + 1 \right)} \right] \tag{2.28}$$

The numerical simulations capture the membrane behavior of the skins with great accuracy; in fact, the coefficient for the skin volume fraction aligns almost perfectly with the theoretical Young's modulus of aluminum. The regression term associated with the re-entrant core explains the combined effect of bending stiffness and synergistic confinement: since the foam is constrained inside the cells, it exerts a stabilizing pressure, increasing the overall stiffness.

$$\nu_{21} \approx -0.338 + 0.025 \cdot \left(\frac{h}{l} \right) + 3.743 \cdot \left(\frac{t}{l} \right) - 0.136 \cdot t_{skin} + 0.0036 \cdot z_{core} \tag{2.29}$$

The regression confirms the auxetic behavior of the core and the counteraction of the foam. Thick walls for the core are stiffer and struggle to contract. Additionally, thicker panels

become more effective in suppressing foam expansion, and they limit its contrast effect on the core. Finally, higher core extrusions show a slight reduction in auxetic capability due to the increased kinematic constraints.

2.6.4. Evaluation of the transverse Young's modulus E_{11} and Poisson's ratio ν_{12} for the foam-filled re-entrant honeycomb with skins

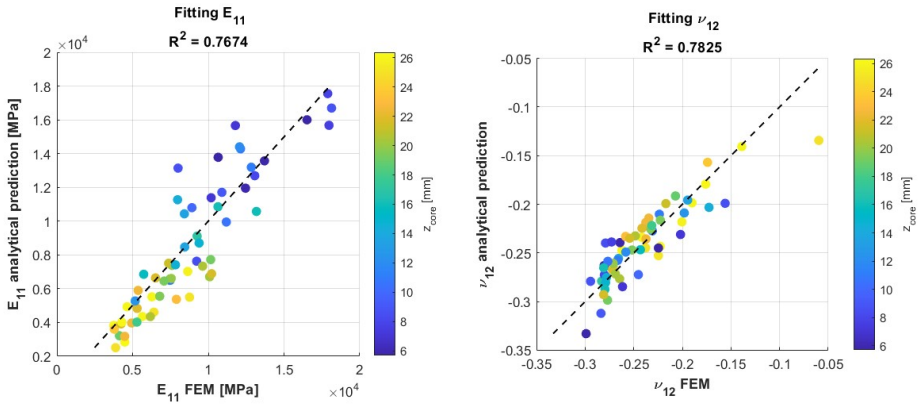

Figure 2.27: Results fitting for E_{11} and ν_{12} for foam-filled re-entrant honeycomb with skins.

$$E_{11} \approx 69635 \cdot \phi_{skin} + 27 \cdot \phi_{core} \tag{2.30}$$

Once again, the regression coefficient for the skins perfectly matches the aluminum modulus. The core contribution is statistically negligible, demonstrating that the longitudinal compliance of the core is so high that it adds virtually no stiffness beyond the baseline contribution of the foam filler.

$$\nu_{12} = -0.037 \cdot \left(\frac{h}{l}\right) + 3.024 \cdot \left(\frac{t}{l}\right) + 0.147 \cdot \sin\theta - 0.185 \cdot t_{skin} + 0.0023 \cdot z_{core} \tag{2.31}$$

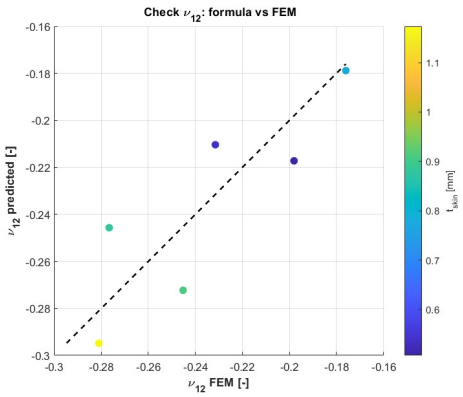

Figure 2.28: Overfitting check for ν_{12}.

The aspect ratio and wall slenderness ratio remain the primary drivers, rewarding thinner sheets to obtain more negative values. The skins play a confinement role for the foam, and core thickness confirms its role as a 3D secondary parameter.

2.6.5. Evaluation of the shear modulus G_{12} for the foam-filled re-entrant honeycomb with skins

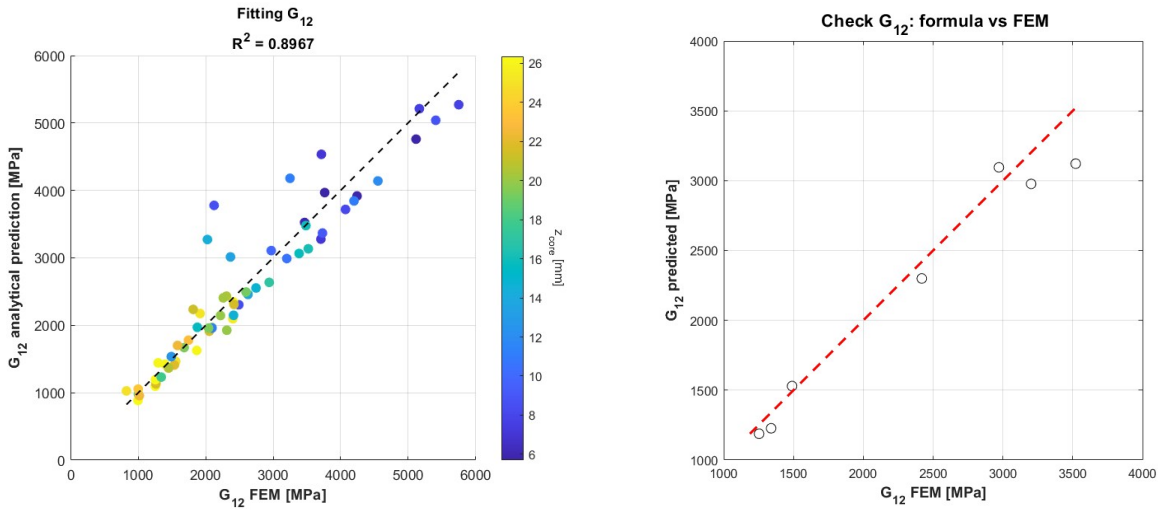

Figure 2.29: Results fitting and overfitting check for G_{12} for foam-filled re-entrant honeycomb with skins.

$$G_{12} \approx 19994 \cdot \phi_{skin} + 10.8 \cdot \phi_{core} + 3.76 \times 10^6 \cdot \left[\phi_{core} \cdot \left(\frac{t}{l} \right)^3 \right] \tag{2.32}$$

Equation 2.32 shows a regression coefficient for the skins that is approximately 24% lower than the theoretical shear modulus for aluminum. The deviation can be physically attributed to the shear lag effect. Conversely, the re-entrant honeycomb contribution is significant, thanks to the foam that acts as an elastic support for the cell walls. The foam itself contributes less than 11 MPa, but its presence is fundamental for the core.

2.7. Foam-filled re-entrant honeycomb configuration

In anticipation of the subsequent experimental phase, new analyses were launched. The configuration considers the re-entrant honeycomb with cells filled with polyurethane foam, without skins. The parameters are all those previously shown, including the honeycomb extrusion.

2.7.1. Evaluation of the transverse Young's modulus E_{11} and Poisson's ratio ν_{12}

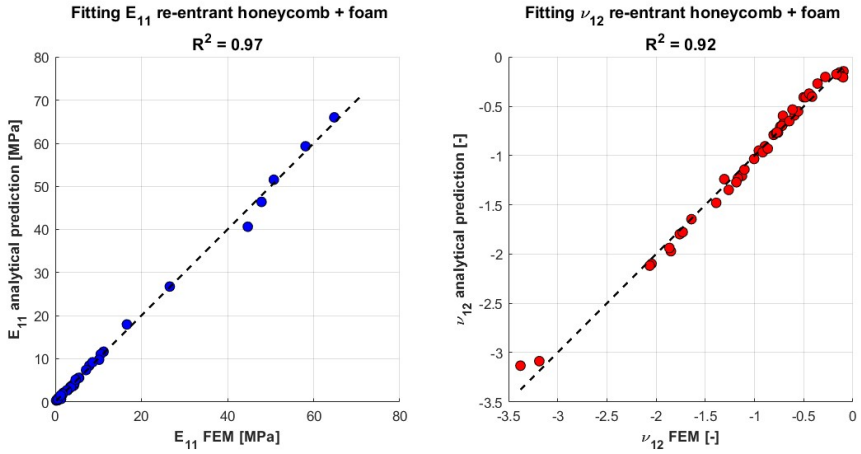

Figure 2.30: Results fitting for E_{11} and ν_{12} for foam-filled re-entrant honeycomb.

$$E_{11} \approx 0.14 + 91900 \left(\frac{t}{l}\right)^3 \frac{\frac{h}{l} + \sin\theta}{\cos^3\theta} \tag{2.33}$$

The longitudinal stiffness ranges between 10 and 60 MPa and remains below the values found in Section 2.2 for the solo re-entrant due to the specific design workspace adopted. Extreme geometries have been excluded from the initial dataset, and the maximum aluminum thickness has been lowered to 1.5 mm, resulting in more slender configurations.

The dominant deformation mechanism remains bending.

$$\nu_{12} \approx -0.648 + 0.217\left(\frac{h}{l}\right) - 1.222\left(\frac{t}{l}\right) - 3.147\sin\theta + 0.003N_x + 0.014N_y \tag{2.34}$$

The Poisson's ratio analysis required a polynomial response surface model to account for complex interactions and edge effects. The auxetic behavior is preserved, and the finite boundary effects slightly moderate the response.

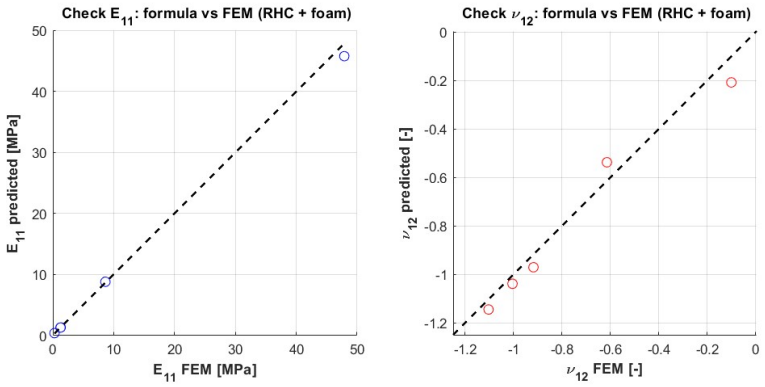

Figure 2.31: Overfitting check.

2.7.2. Evaluation of the transverse Young's modulus E_{22} and Poisson's ratio ν_{21}

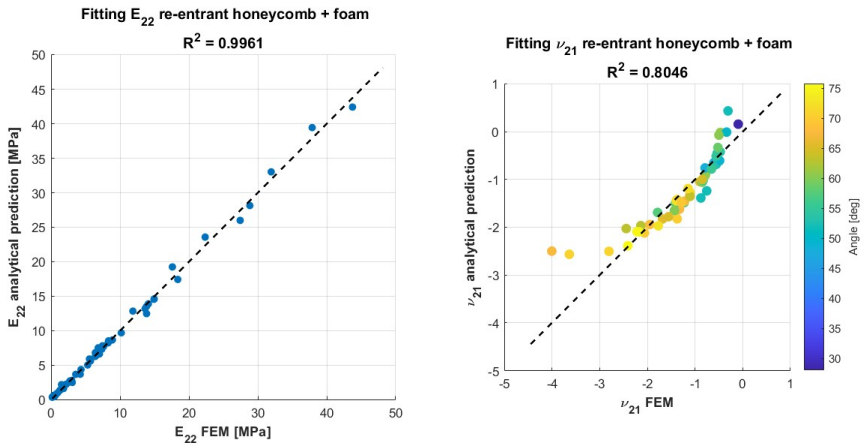

Figure 2.32: Results fitting for E_{22} and ν_{21} for foam-filled re-entrant honeycomb.

$$E_{22} \approx 0.30 + 75686 \left(\frac{t}{l}\right)^3 \frac{\cos\theta}{\left(\frac{h}{l} + \sin\theta\right)\sin^2\theta} \tag{2.35}$$

The regression analysis results in an intercept of 0.3 MPa, confirming that the response is strongly governed by bending, and foam provides a minimal but non-zero contribution. Moreover, the observed range of stiffness is limited for the same aforementioned reasons of design space restriction.

$$\nu_{21} \approx -5.01 + 0.85\left(\frac{h}{l}\right) + 21.3\left(\frac{t}{l}\right) - 4.5\sin\theta + 47.8\left(\frac{t}{l}\sin\theta\right) \tag{2.36}$$

Conversely, Poisson's ratio once again requires a non-linear polynomial model to consider the complex interaction between the skeleton, foam, and boundary effects.

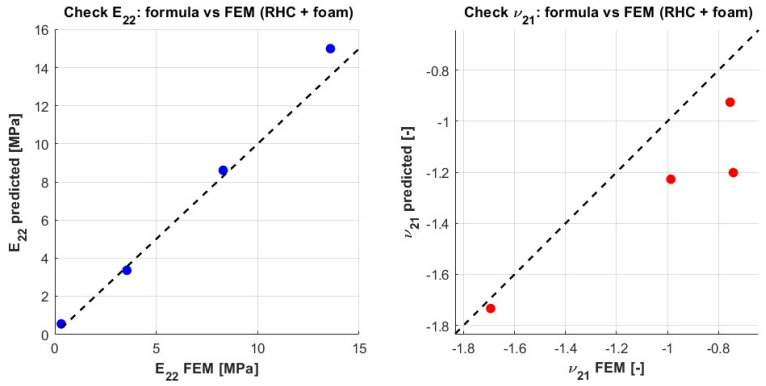

Figure 2.33: Overfitting check.

2.7.3. Evaluation of the shear modulus G_{12}

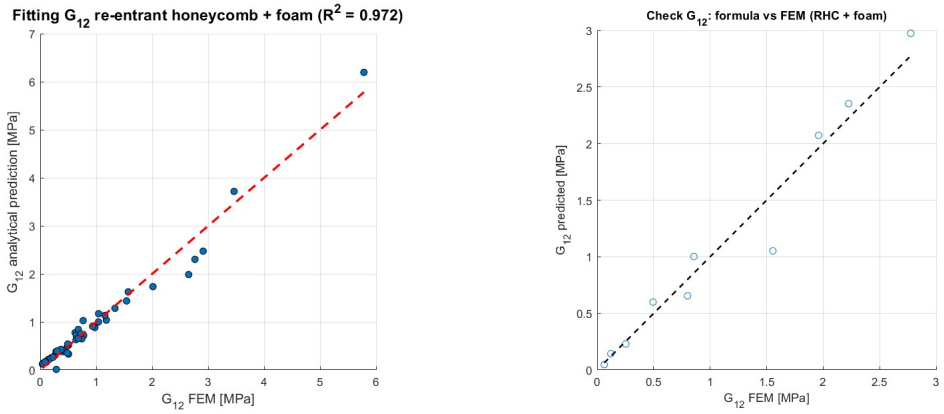

Figure 2.34: Results fitting for G_{12} for foam-filled re-entrant honeycomb.

$$G_{12} \approx 0.216 + \left(\frac{t}{l}\right)^3 \left[308500 - 155900 \cdot \cos\theta - 121200 \cdot \frac{h}{l}\right] \tag{2.37}$$

The results highlight the dominance of bending as the main deformation mechanism, consistent with the predictions of Masters and Evans. However, augmented terms are required to accurately capture the stiffening effects at the cell nodes and local shear deformations. The intercept once again shows the small but not insignificant contribution of foam.

2.8. Optimization

Before proceeding with the experimental section in Chapter 3 and numerical simulations in Chapter 4, the first fundamental step is the selection of an appropriate configuration. As seen previously, many different combinations of the eight varying parameters produce structures that are able to guarantee great in-plane stiffness values on paper. Higher values of Young's and shear moduli do not mean that the best solution has already been obtained. In fact, total mass must be considered to evaluate structural effectiveness.
The first challenging task is to identify a possible optimal configuration among the thousands generated during the static analyses. Rather than simply choosing the one with the highest stiffness, it becomes essential to balance stiffness against mass, guarantee the auxetic behavior, and consider practical constraints. One of them arises directly from the application context: the energy absorbers in the subfloor of a helicopter are mounted between two anchor points spaced at a certain distance. Based on the literature on medium-sized helicopters [17], a free length of 500 mm is reasonable for this study. It means that the old independent parameter `cellsize` becomes a dependent parameter since the total `model length` has been fixed. It will be derived in the modified script `main.m` through the inverted formula:

$$\text{cellsize} = \frac{\text{model length} + (\text{n horizontal} - 1) \cdot 0.5 \cdot \frac{\text{cell height}}{\tan(\text{angle})}}{\text{n horizontal}} \tag{2.38}$$

All scripts and functions have been updated.
To find a possible optimal structure, a `MATLAB` genetic algorithm (`GA`) has been adopted. The objective is to find the combination of parameters that generates a configuration that maximizes the in-plane shear modulus G_{12} and the auxeticity while minimizing the density (mass per unit volume). For instance, the upcoming simulations aim to involve non-vertical and localized impacts. In such conditions, a higher shear modulus ensures better load distribution and energy absorption.

The genetic algorithm is a population-based optimization method inspired by natural selection and evolution. Each candidate solution represents a set of the 7 geometric parameters, and it is evaluated through a fitness function. By applying selection, crossover, and mutation, the algorithm pushes the population towards a possible optimal configuration.
The 7-dimensional design space includes:

- `h`, cell height,
- θ, re-entrant angle (in degrees),
- `t`, core aluminum sheet thickness,
- `n_horizontal`, number of horizontal cells (constrained to be an integer),
- `n_vertical`, number of vertical cells (constrained to be an integer),
- `s`, skin thickness,
- `z`, core extrusion thickness.

This study investigates two distinct configurations of the foam-filled re-entrant honeycomb, distinguishing between the presence and absence of external skins.
A large population of 1000 individuals, with up to 100 generations, is chosen to explore the multimodal space and reduce the risk of premature convergence. The explorable values are limited by the vectors lower and upper bounds, defined as:

- lb = [20, 10, 1, 10, 4, 0.5, 5],
- ub = [100, 80, 1.5, 20, 7, 1.5, 20].

The optimization problem is formulated differently for the two configurations, as the presence of aluminum skins fundamentally alters the structural mechanics.

In the absence of skins, the lower and upper bounds vectors exclude the sixth parameter. The cellular core must provide sufficient shear stiffness (G_{12}) on its own while maximizing the auxetic performance. Therefore, G_{12} is explicitly included in the objective function to penalize compliant designs. The minimization target is defined as:

$$target = \frac{\nu_{12} \cdot G_{12}}{\rho_{norm}} \tag{2.39}$$

Since ν_{12} is negative for auxetic structures, minimizing this product simultaneously maximizes the magnitude of the Poisson's ratio and the shear stiffness, while minimizing the

normalized density. The script includes a penalty method for positive Poisson's ratios in case the algorithm explores non-auxetic configurations.
When aluminum skins are present, the in-plane shear stiffness is largely dominated by the skins themselves, making G_{12} inherently high for all possible designs. Consequently, the optimization focuses on enhancing the auxetic behavior and lightweighting. The objective function is simplified to:

$$target = \frac{\nu_{12}}{\rho_{norm}} \tag{2.40}$$

The density ρ is calculated as:

$$\rho = \frac{mass}{V_{tot}} \tag{2.41}$$

and normalized to be comparable to the other targets.
The total volume is trivial to obtain:

$$V_{tot} = 500 \cdot (h \cdot n\_v) \cdot (z + 2 \cdot s) \tag{2.42}$$

where $s = 0$ when skins are absent.
The algorithm returns the best set of parameters `x_best` and the associated target value `fval`.
The script is run 10 times, saving the best set of parameters for each run in a new `population.csv`. These configurations have been submitted to the `montecarlo.m` script so that the same analysis described in Paragraph 2.3 can be conducted on `Abaqus`. The displacements were saved using the usual `Python` automation, while mass values were recorded by opening each `Job.odb` file. The results were post-processed to discover which configurations revealed the minimum `target` value.
The best model obtained for each configuration is characterized by the following parameters:

Table 2.3: Optimized configuration parameters from the genetic algorithm and `Abaqus` analyses.

h [mm]	θ [°]	t [mm]	n_h	n_v	s [mm]	z [mm]
20	64.8	1.5	10	6	0	16.1
20	28.9	1.5	10	6	0.5	15.3

3 | Experimental section

Following the theoretical characterization and numerical optimization, the research progressed to the physical validation phase. This Chapter details the manufacturing and testing of physical prototypes of the foam-filled aluminum re-entrant honeycombs.

The acquired experimental data are fundamental to validate the non-linear Finite Element Models that will be developed.

3.1. Specimen manufacturing

The raw material provided for the specimen fabrication was a commercial aluminum alloy sheet with dimensions of 2×1 m. A crucial deviation from the numerical optimization must be noted: while the configuration identified in Paragraph 2.8 relied on a sheet thickness of 1.5 mm, the available commercial plate has a thickness of 1.2 mm. As a consequence, the FEM model will be re-evaluated considering this change so that a comparison between numerical and experimental results can be performed in Chapter 4.

Figure 3.1: Shearing machine.

The manufacturing process involved cutting the sheet into a smaller area and then into 12 distinct strips, which form the layers of the re-entrant honeycomb structure.

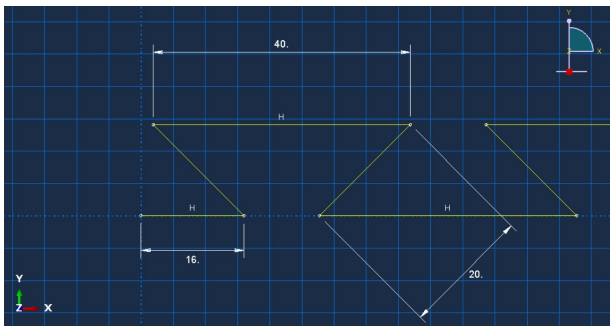

Figure 3.2: Repeated unit, conceptual sketch for aluminum strips with quoted dimensions.

The total unfolded length of each strip was calculated as follows:

$$L_{tot} = 2 \cdot 16\,mm + 9 \cdot 40\,mm + 10 \cdot 20\,mm = 592\,mm \tag{3.1}$$

Since the core extrusion was set to 1.5 mm, the aluminum area required for a single model is:

$$A = 1.5 \cdot L_{tot} = 0.10656\,m^2 \tag{3.2}$$

The entire panel was cut into a smaller panel and finally into 12 strips using the hydraulic guillotine shear showed in Figure 3.1. A small additional tolerance was considered to ensure dimensional accuracy and to eliminate the border that results rough at the end of the process.

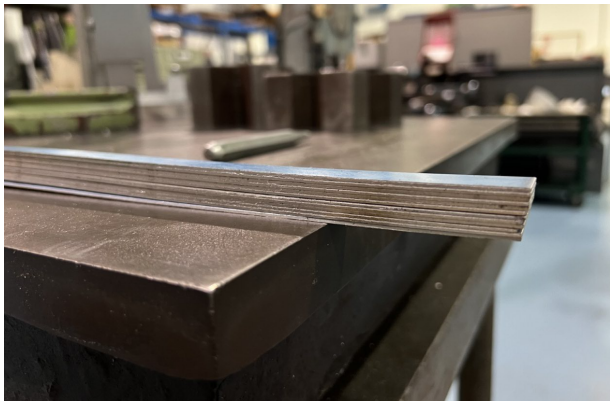

Figure 3.3: The 12 layers.

Following the cutting phase, the folding points were manually marked on each strip. To

achieve the target 50° angle:

- two custom jigs were manufactured from a solid aluminum block available in the laboratory. The block was machined using a bandsaw to create a clean cut;
- each strip was carefully bent using a jig and a rubber mallet to avoid localized damage;
- to contrast the springback effect, each fold was finally over-bent manually.

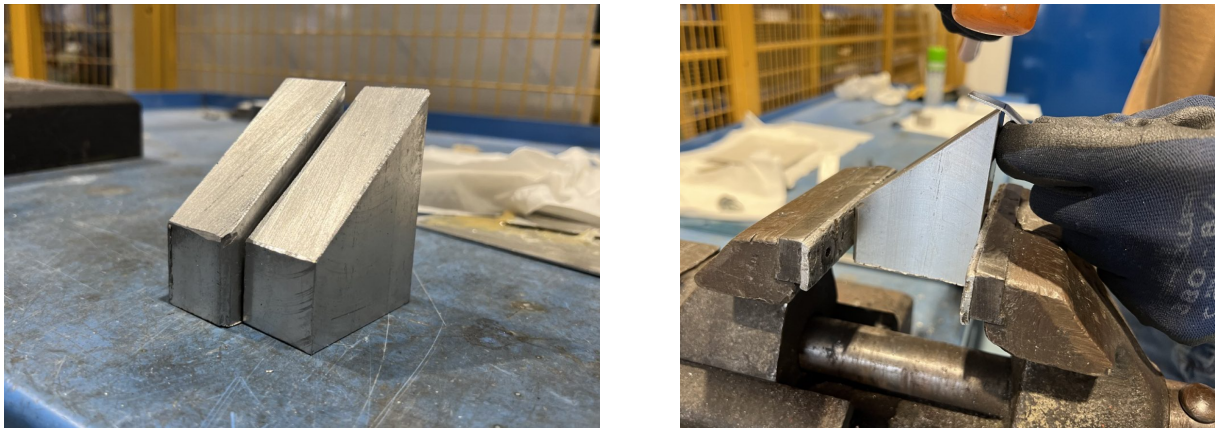

Figure 3.4: Aluminum jigs.

Once all the strips were carefully formed, they were aligned to create the re-entrant honeycomb grid structure. They have been temporarily constrained in the correct configuration using Kapton heat-resistant tape [11]. The cell walls, in this manner, coincide with greater precision, which is difficult to obtain through manual manufacturing.

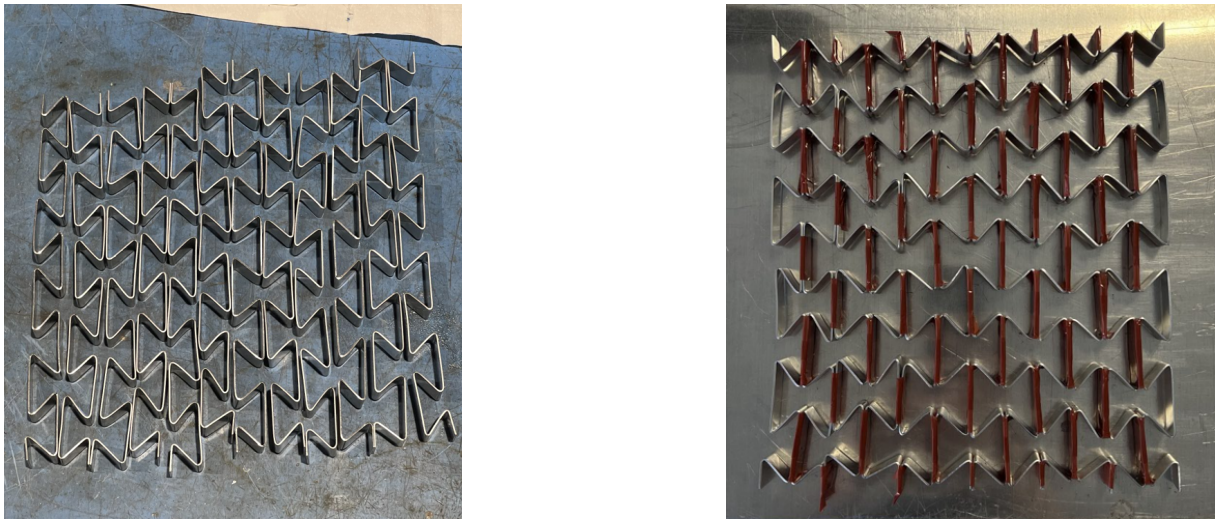

Figure 3.5: Separate single layers and Kapton application to create model `RH-1`.

To mitigate the residual stresses induced during the folding and constraining processes, a stress-relief heat treatment was performed. The assembly was placed in a laboratory oven subjected to a cycle of 6 hours at 180 C, during which a distributed dead weight was placed on top of the structure to prevent and correct out-of-plane warping.
Finally, the Kapton was removed, and an epoxy-based structural adhesive (Scotch Weld AKF 163-2K) was applied to the same horizontally coinciding parts.

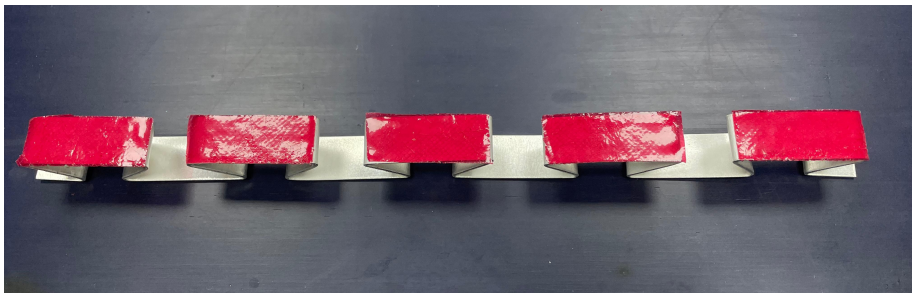

Figure 3.6: Kapton adhesive applied on a layer.

The structure was placed in the laboratory oven using a Teflon (PTFE) sheet to avoid possible dispersion of the resin, and it was subjected to a cycle at 125 C for 2 hours.

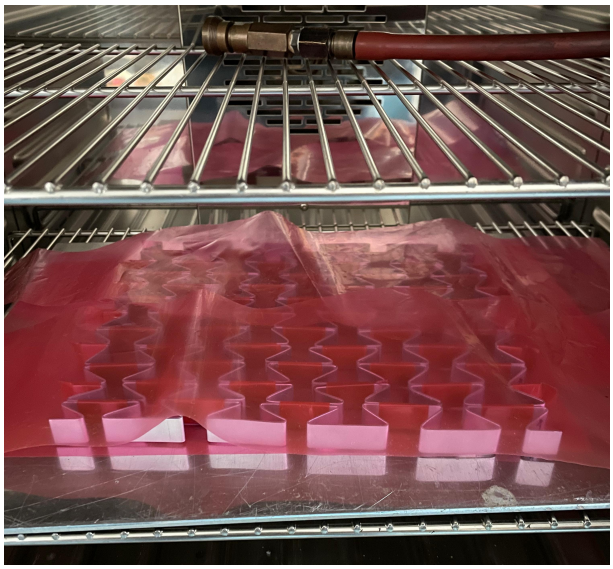

Figure 3.7: Second cycle in oven at 125 C for 2 hours.

The final structure obtained is shown in the following picture. Kapton was removed later.

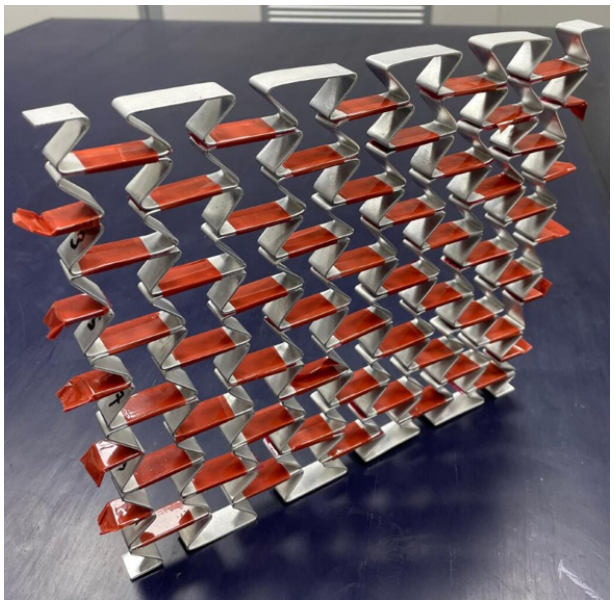

Figure 3.8: Assembled re-entrant honeycomb `RH-1`.

After the successful creation of the first prototype, `RH-1`, the manufacturing phase continued with the production of two additional identical structures. Each one is composed of 12 layers, so 24 additional strips were sheared from the original aluminum panel following the same rolling direction.
The strips were then subjected to the same technological process described for the first prototype.

3.2. Foam filling

To improve the crashworthiness capabilities of the auxetic energy absorber, the re-entrant aluminum core was reinforced using a specialized polyurethane foam filler, `CONFOR CF45M` [1]. As mentioned in Paragraphs 1.1.5 and 2.5, this material is widely adopted in the aerospace industry for impact protection and vibration damping. Such foam exhibits highly viscoelastic behavior and strain-rate sensitivity.
The primary structural objectives can be summarized as two main effects. First, the foam provides lateral support to the aluminum cells, delaying local buckling and preventing possible catastrophic global failure modes. The structure is forced to deform in a more progressive and stable manner. Secondly, the filler contributes directly to the total energy dissipation, increasing the energy absorption capability.
Starting from a bulk panel of `CONFOR CF45M`, hourglass-shaped discrete pieces were cut with precision using the hydraulic guillotine shear. Every insert was individually placed to fill the cells of the aluminum skeleton, ensuring a tight fit.

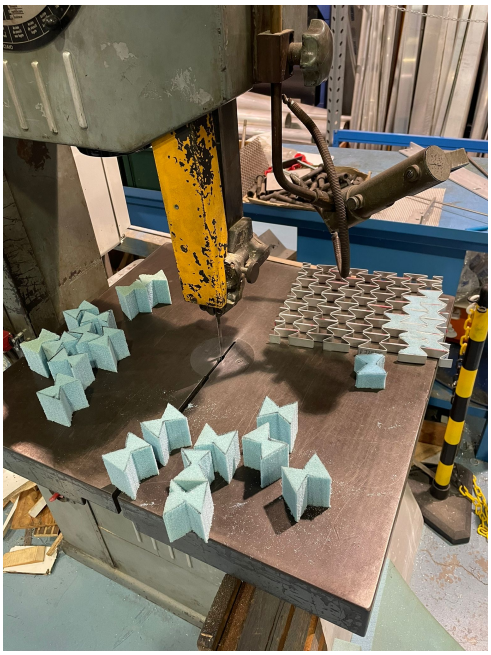

Figure 3.9: Foam inserts and placement inside cells.

3.3. Drop tower test

A vertical crush test was conducted at the LAST laboratory, located in the Politecnico di Milano, Bovisa, B6 building. The experimental setup included a guided vertical drop tower equipped with an impactor, whose minimum mass is 5.55 kg and can be increased by adding specific disks. The impactor is a steel cylinder terminating in a rigid hemispherical nose, whose diameter is 10 cm. For instance, the numerical model took those parameters into consideration from the beginning of the investigation.

Figure 3.10: Impactor mass.

The specimen called `RH-2` was mounted on a dedicated support, whose height can be regulated according to the model dimensions and the desired measurements. The support was notably designed with transparent clamping plates, so that all entire model can be captured by the camera, allowing for the complete visualization of the deformation kinematics.
Data acquisition was performed using:

- an accelerometer, mounted on the impactor and connected to the main station via cable, which is able to register data at a frequency of 20 kHz;
- an high-speed imaging camera, with a 4 seconds span and a very high temporal resolution to capture the rapid transient phases of the collapse.

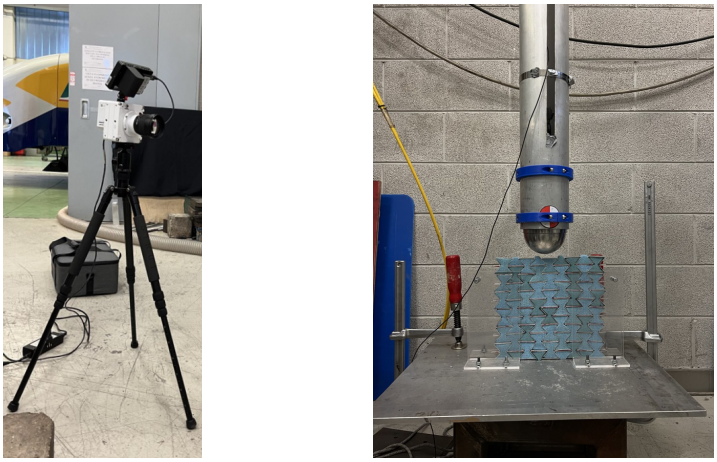

Figure 3.11: High resolution camera and final set-up.

3.3.1. Drop test

The impactor was lifted via a cable mechanism to a height of 5.497 m. The precise value was measured using a Laser Distance Meter. Subsequently, it was released, and it impacted the center of the top of the specimen in free fall. However, it is important to consider tolerances and friction.
After the sudden impact, the first qualitative analysis of the videotape highlighted the following aspects.
The auxetic behavior is confirmed: the structure shrinks in both directions, which means that the cells work to absorb energy.
Elastic recovery is clearly present: a significant elastic springback can be observed immediately after the maximum compression. For this reason, the graph of velocity is expected to oscillate from negative to positive and then back to negative values.

An important residual plastic deformation characterizes the structure at the end of the test, validating its capacity to dissipate kinetic energy by collapsing.

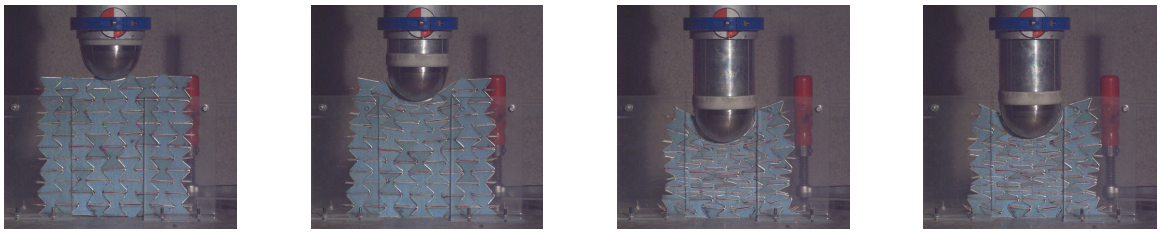

(a) Before impact (b) Punch indentation (c) Max. indentation (d) Elastic springback

Figure 3.12: Crash progression in specimen RH-2.

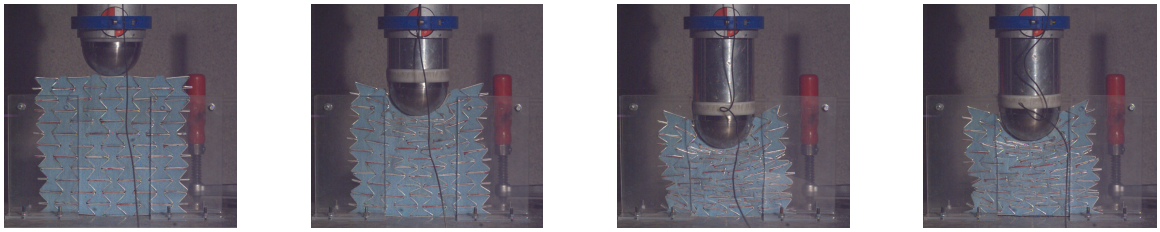

(a) Before impact (b) Punch indentation (c) Max. indentation (d) Elastic springback

Figure 3.13: Crash progression in specimen RH-3.

Figure 3.14: Deformed specimens RH-2 and RH-3.

3.4. Aluminum tensile test

To accurately define the material properties, in anticipation of the subsequent numerical validation, uniaxial tensile tests were conducted on the aluminum alloy strips used to

build the honeycomb structures. The tests were performed using the MTS servo-hydraulic universal testing machine equipped with hydraulic wedge grips, available at the material testing laboratory at Politecnico di Milano.

Figure 3.15: MTS servo-hydraulic testing machine.

It is fundamental to highlight that the aluminum strips tested were not standard dog-bone specimens. The strips are simply rectangular with a constant cross-section, thus, the failure is expected to occur at the grip interfaces.
A clip-on extensometer was mounted in correspondence with the central section of the specimen to ensure precise strain measurements.

Figure 3.16: Positioned specimen with extensometer mounted.

The constitutive behavior of the aluminum alloy was derived by analyzing the experimental data and taking into account the limitations imposed by the specimen geometry.
As usual, the Young's modulus was calculated using the strain data provided by the extensometer, collected in the `uniaxial_tests.xlxs`. All the experimental curves show an initial consistent linear response, and stiffness results E =67.424 MPa, typical for aluminum alloys.
The result is the mean value of the slopes of the linear segment in the stress-strain curves:

$$E = \frac{\sigma}{\epsilon} \tag{3.3}$$

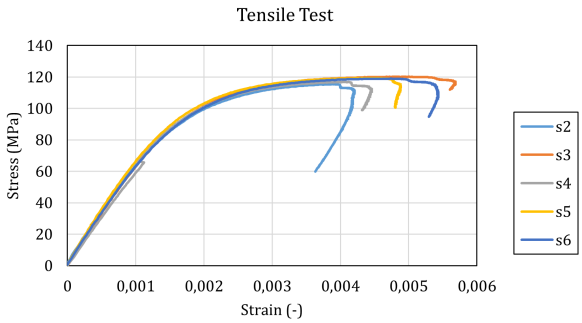

Figure 3.17: Experimental curves stress vs strain.

The unusual shape of the specimen caused stress concentration at grip interfaces. Consequently, local strain measurements became unreliable beyond the proportional limit. For instance, plastic localization and necking started outside the *gauge length*. For these reasons, the post-yielding behavior should be evaluated using the global stress-displacement curves derived from the movement of the crosshead of the machine.

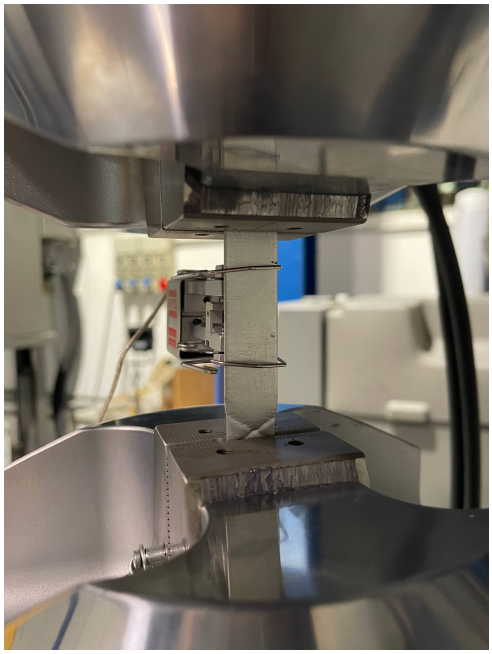

Figure 3.18: Specimen 1 failure.

To validate the observations, the standard 0.2% offset method was applied to the initial strain data, and the theoretical intersection confirms that the yield point is around 110 MPa, while the maximum ultimate strength before failure never exceeded 120 MPa. It is a reasonable approximation to model the material as elastic-perfectly plastic, with a conservative yield stress value set at 110 MPa.

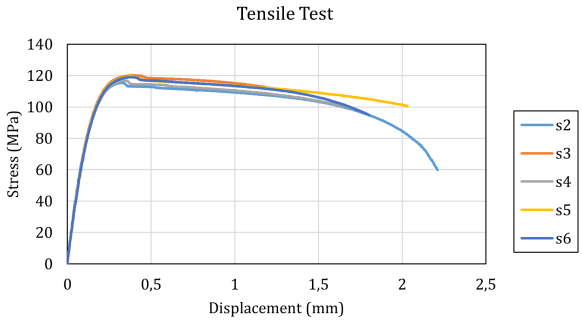

Figure 3.19: Experimental curves stress vs displacement.

4 | Dynamic numerical simulations and model validation

After performing extensive evaluations and regression analyses for in-plane Young's and shear moduli, as well as Poisson's ratios across a wide spectrum of geometric parameters, numerous configurations were obtained. The stiffness values cover a limited yet varied range. All designs, especially the core solo, exhibited auxetic behavior, confirmed by the negative Poisson's ratio. Possible optimal combinations of the geometric parameters were obtained and require further investigation.
The central problem is still to be addressed: are these structures also capable of effectively absorbing energy while maintaining a relatively low activation threshold?
This Chapter aims to provide a positive answer to the question.

Two main types of crash simulations were carried out:

- global compressive test, where the selected structure is crushed up to a pre-defined displacement;
- localized impact test, with a hemispherical punch, representing concentrated loading.

However, the very first main goal is the reciprocal validation of the experimental tests and numerical models. For this reason, the two impact simulations are now introduced, but the analyses will be carried out later in this Chapter.

4.1. Global compressive test

The global crash test is designed to evaluate the specific energy absorbed (SEA) under quasi-axial impact conditions.
The analysis is performed using `Abaqus/Explicit`. The solver is particularly suitable for highly nonlinear problems involving large deformations, complex contact interactions, and short duration dynamic events such as crash or impact tests. The explicit formula-

tion integrates the equations of motion directly in time using a central-difference method, avoiding the need for the implicit method for matrix inversion at each increment.
The model includes two analytical rigid surfaces acting as compression platens. In the `main.m` script, a dedicated `*PART` named `WALL` is created to represent an analytical surface, including a single reference node `RP`. Analytical surfaces in `Abaqus` are idealized geometric entities that do not require meshing, avoiding contact penetration errors and reducing computational costs. The surfaces are defined as cylinders, providing a smooth and continuous contact interface over the entire model width. Using the cylindrical definition instead of the planar one ensures accurate contact, even if the model experiences slight rotations or global bending during the simulation.
Two instances of this part have been created: `WALL-1` positioned at 1 mm at the bottom of the structure and `WALL-2` positioned at 2 mm at the top of the structure. Each surface has got a reference point that controls the rigid body kinematics of its associated surface.

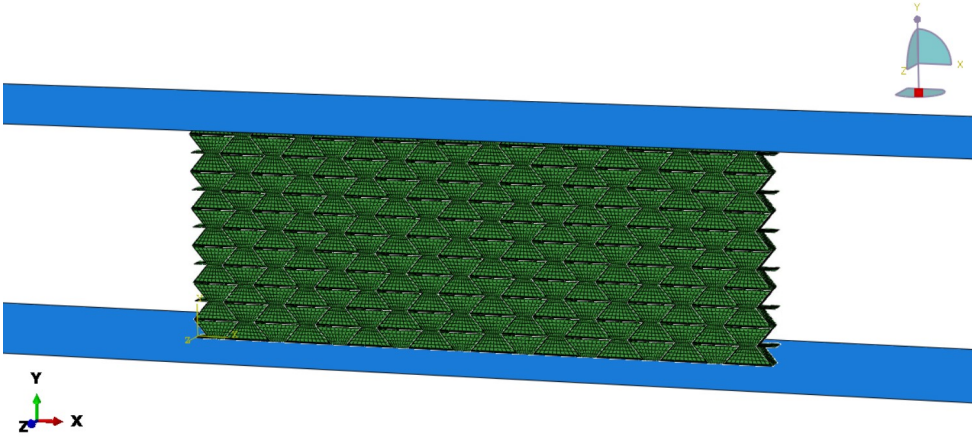

Figure 4.1: Example of Assembly for global compressive analysis.

The lower surface is constrained using an `ENCASTRE` condition.
The upper surface is constrained in all directions, with the exception of the global y-axis. Along this direction, a constant downward velocity of $-5000\,\mathrm{mm/s}$ is imposed. This particular motion simulates a compression impact against the lower rigid plate.
Contact between the structure and the surfaces is modeled using a `GENERAL CONTACT` formulation, with a friction coefficient of 0.4 and a `HARD` pressure overclosure relationship, causing an abrupt stiffness increase upon contact. The `Abaqus GENERAL CONTACT` is a strong formulation that automatically detects and enforces contact between all exterior surfaces of the model, avoiding manual pair definition.
The simulation is carried out using an explicit dynamic procedure with nonlinear geo-

metric effects enabled. The `STEP` duration is set to 0.01 sec. As suggested in the `Abaqus User Guide`, bulk viscosity coefficients are added to improve numerical stability.
`History outputs` are requested at the upper plate reference points to record the displacement, velocity, acceleration, and reaction force at every increment.

4.2. Impact test with hemisferical punch

Spoiling the advantages of the auxetic behavior, the investigation progresses to evaluate the response of the model to localized impact loads that can indeed occur during a helicopter lifecycle. Concentrated loads are typical of impacts with terrain irregularities or debris. Thus, it is fundamental to evaluate efficiency in terms of energy absorption and to assess the structural integrity and penetration resistance.
The finite element method was derived from the previous uniform crash simulations.
The upper analytical rigid surface, called `WALL-2`, was suppressed and replaced by a hemispherical impactor, designated in the model as `PUNCH`. In the `Part` module, an analytical rigid surface was generated via revolution. The size of the radius, which is $R = 50\,\text{mm}$, has been chosen according to the impactor available in the laboratory. A Reference Point (`RP1`) was created at the center of the hemisphere.
In the `Assembly` module, it was positioned to align its vertical axis with the center of the cross-sectional XZ-area, ensuring a centered impact. The Reference Point has been re-defined in the same position to allow the application of boundary conditions on it.

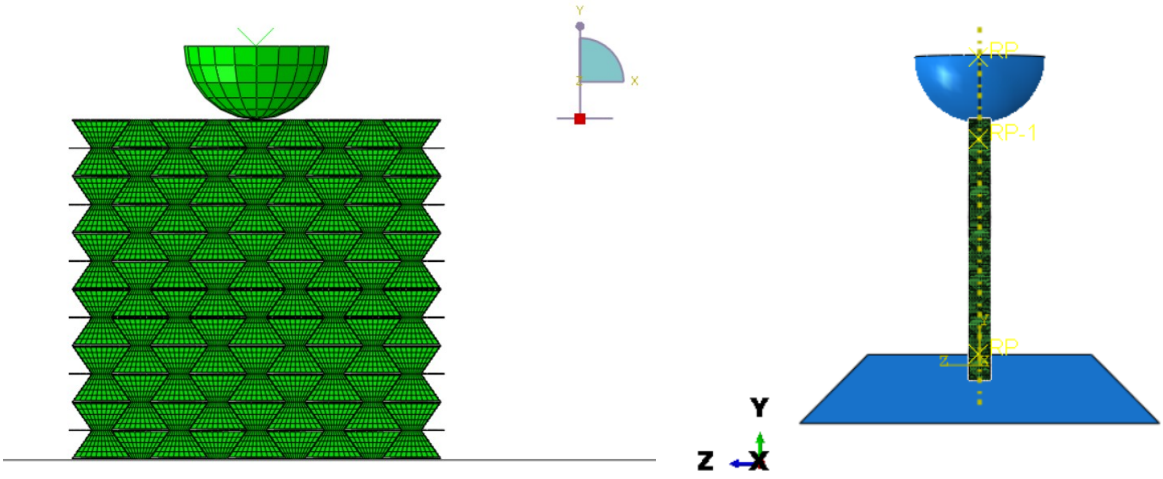

Figure 4.2: Example of Assembly for localized impact analysis.

Unlike the displacement-controlled simulation performed in the previous section, the following analysis simulates a dynamic drop test governed by the kinetic energy of the falling

mass.
To represent the physical inertia of the impactor, a point mass of 5.55 kg was assigned to the Reference Point in the `Property` module.
The boundary conditions applied are the same as in the previous analysis, restricting all degrees of freedom except for vertical translations along the Y-axis. The boundary condition imposing a constant velocity was removed. Instead, in the `Predefined Field`, an initial velocity was set. The punch will decelerate naturally upon contact with the structure.
Finally, the `History Output` was set to record the time-history of reaction force, vertical displacement, velocity, and acceleration at the Reference Point.

4.3. Numerical validation

In the present section, the numerical framework described in Paragraph 4.2 is adapted to replicate the specific experimental conditions of the impact tests. `Abaqus/Explicit` is adopted, and the models have been updated to reflect the actual geometric properties measured on the handcrafted specimens `RH-2` and `RH-3`. Moreover, `Al-2024-T3` was substituted in the material definition to reflect the values described in Paragraph 3.4. A critical boundary condition for the simulation is the impact velocity of the hemispherical punch. To ensure good fidelity, it was derived using `PCC` (Phantom Camera Control) software. After a calibration procedure, the velocity was calculated as the statistical mean of 10 repeated measurements, resulting in $v_{02} = 8.389\,\mathrm{m/s}$ and $v_{03} = 9.322\,\mathrm{m/s}$. Despite a negligible difference in drop height, the impact velocities are different due to increased cable friction in the first experiment. Generally, the kinematic behavior of the tower used is described by the equation:

$$v_0 = \sqrt{2 \cdot g \cdot h \cdot \eta} \tag{4.1}$$

with an efficiency factor $\eta = 0.8$. For specimen `RH-3`, it results in a velocity of $v_{03} = 9.287\,\mathrm{m/s}$, which is consistent with the more precise value obtained through the software.
To consider the influence of the idealization of the numerical with respect to real specimens, five identical simulations were run for each of them. The only parameter that changed was the shell thickness of the re-entrant honeycomb, ranging from its nominal value to a reduction of 10% at equally spaced intervals.
The geometric measures of each specimen are presented in Tables 4.1 and 4.2.

Table 4.1: Measured geometric properties of the re-entrant lattice specimens (mean values).

Specimen	**Cell size** [mm]	**Cell height** [mm]	L_{tot} [mm]	H_{tot} [mm]	**Thickness** t [mm]	**Extrusion** z [mm]
RH-2	40.18	38.64	258.29	234.40	1.17	15.31
RH-3	40.37	38.37	254.29	232.50	1.22	15.31

Table 4.2: Experimental impact conditions recorded for the drop tests.

Specimen	**Drop height** H_{drop} [m]	**Impact velocity** v_0 [m/s]
RH-2	5.497	8.389
RH-3	5.495	9.322

An example of the deformed shape of the model at maximum compression is shown in Figure 4.3.

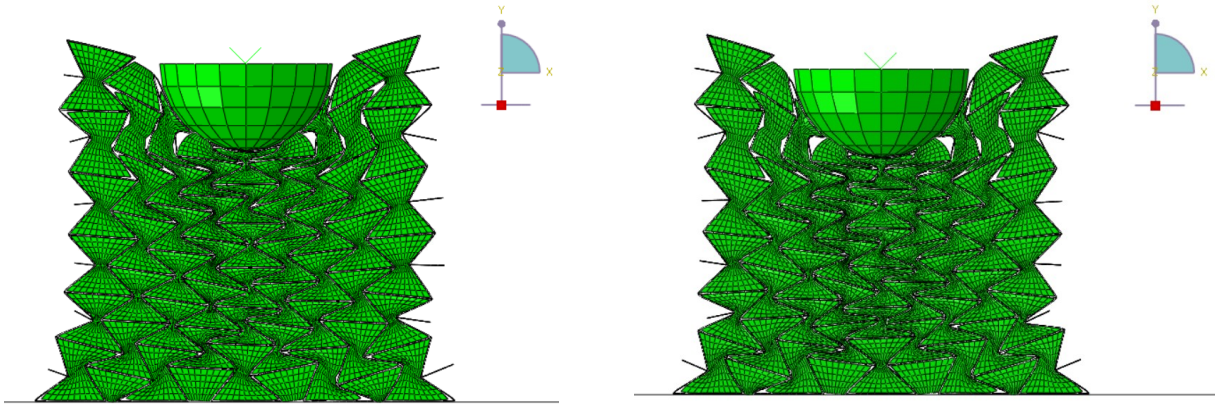

Figure 4.3: Maximum deformation for `RH-2` and `RH-3`, nominal shell thickness.

The experimental and numerical acceleration-time curves are superimposed in Figure 4.4 for direct comparison. The plot highlights that the FEM model correctly predicts the overall deformation behavior of the structure. The trend is very well captured, as well as the peak load, with a slight numerical overestimation. Although the idealized homogeneous model and the imperfections of the handcrafted specimens cause a certain discrepancy. In fact, the numerical model is intrinsically stiffer and perfectly symmetric.

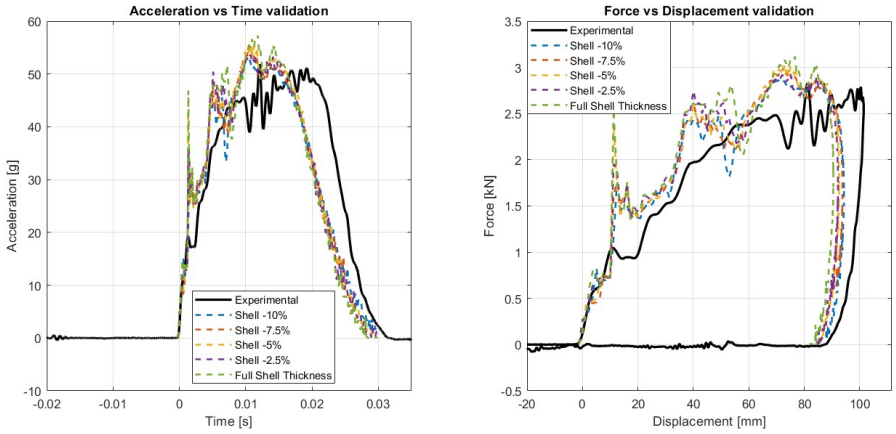

Figure 4.4: `RH-2`: experimental vs numerical data.

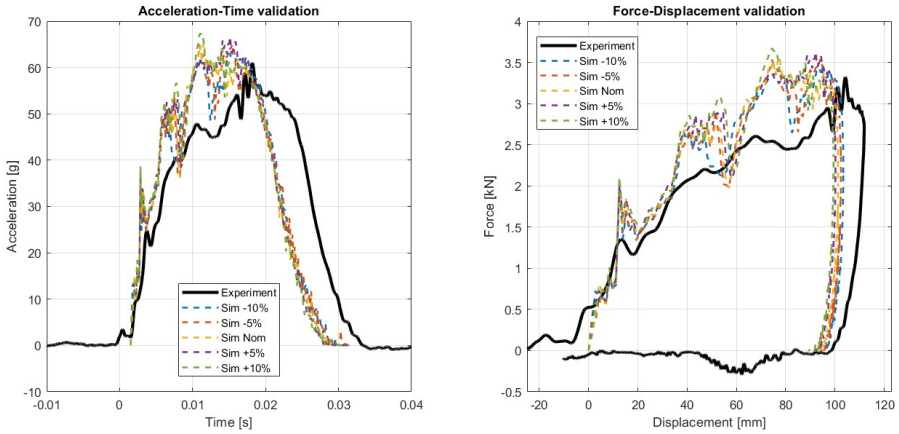

Figure 4.5: `RH-3`: experimental vs numerical data.

The validation analyses reveal a good correlation between the experimental and numerical results. Although distinct deviations can be observed due to the inherent differences between the physical specimens and the numerical idealization. The FEM models assume perfect geometries, sharp angles, homogeneous materials, and a precisely centered impact. On the other hand, the real structures suffer from manufacturing imprecisions and geometric imperfections. Consequently, the numerical curves exhibit stiffer behavior: the initial rise is steeper, and the peaks are slightly overestimated. The real specimens absorb the impact energy over a longer deformation path compared to analytical predictions.

4.4. Results of the global compressive test

To investigate the deformation behavior, both optimal configurations were tested under the condition detailed in Paragraph 4.1. Figure 4.6 illustrates the deformed shape of the finite element model of the foam-filled re-entrant honeycomb at the end of the crushing event.

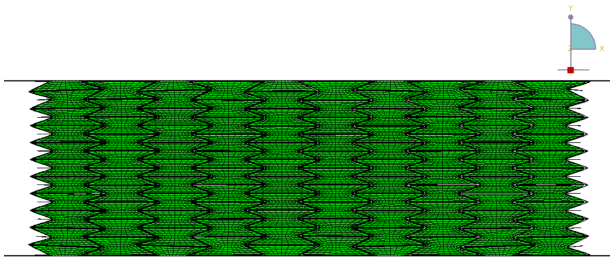

Figure 4.6: Deformed shape of the optimal RHC + foam model.

A more distinct deformation pattern is evident in the analysis of the configuration that includes skins. An additional structure can be observed in Figure 4.8: it was built with the same geometric parameters as specimen `RH-2`, except for a doubled length and the addition of two thick skins of 1.5 mm each. The result is shown to give more credit to the following considerations.

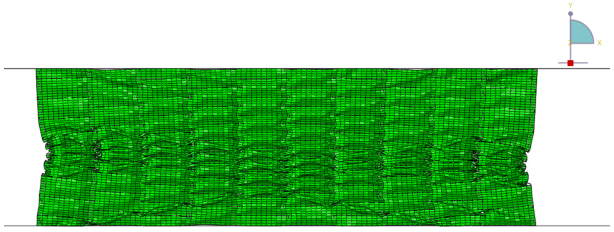

Figure 4.7: Deformed shape of the optimal RHC + foam + skins model.

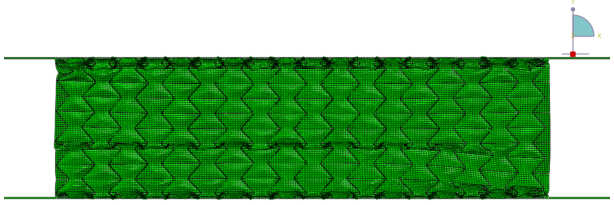

Figure 4.8: Deformed shape of the specimen `RH-2` + skins.

- The crushing initiates symmetrically at the layers in direct contact with the rigid surfaces.
- The cell walls, along with the skins, begin to fold and buckle in the outer area. The deformation progresses inward through the center of the panel.
- The central layers begin to collapse later, demonstrating that the auxetic beam is able to absorb energy progressively through the folding of the layers.

This particular mechanism is consistent with the crash of auxetic panels in the literature. As demonstrated by Novak [28], uniform re-entrant structures tend to deform primarily in the area of the shear planes. The presence of polyurethane foam filler, while not drastically changing the results, acts to stabilize the progressive collapse and contributes to the total energy absorption.

The following plot was extracted from `History Outputs`. It presents two curves.

- DISPLACEMENT ($U2$): the dark blue line represents displacement, enforced through the reference point of the superior surface. For this reason, the progression is linear at a rate of 5000 mm/s;
- REACTION FORCE ($RF2$): calculated at the reference point of the superior analytical surface. It represents the negative force of the structure opposing motion. Its modulus is the force experienced as the structure progressively crushes.

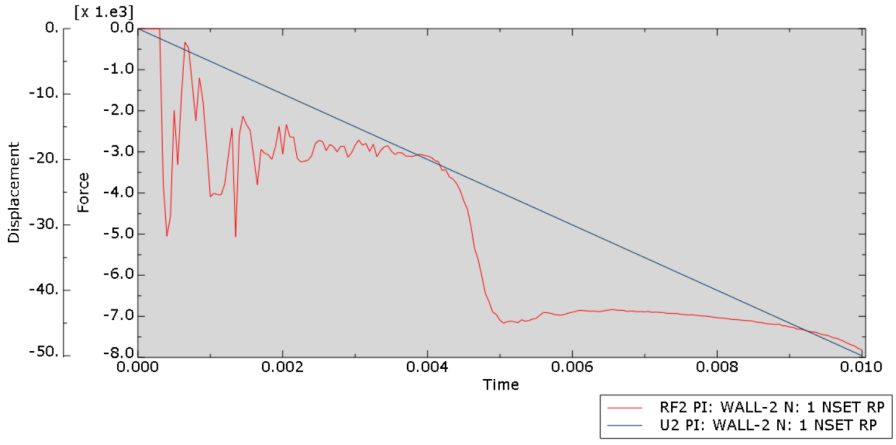

Figure 4.9: Reaction force and displacement at `RP2` for RHC + foam model.

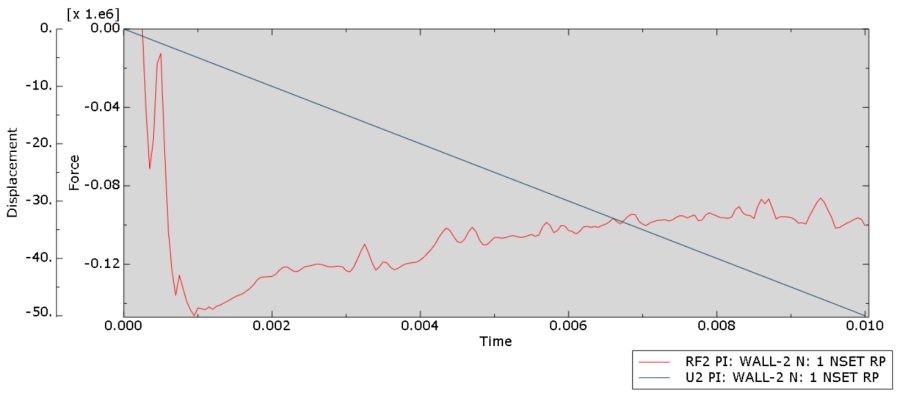

Figure 4.10: Reaction force and displacement at RP2 for RHC + foam + skins model.

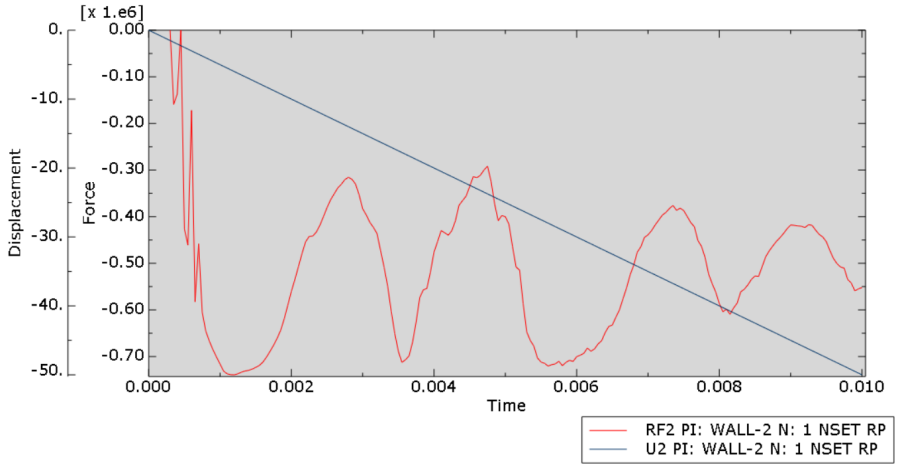

Figure 4.11: Reaction force and displacement at reference point RP2.

The configuration without skins clearly exhibits the lowest Initial Peak Crash Force (IPCF), as the reaction load is generated only by the compliant re-entrant honeycomb. The force-displacement curve displays a fluctuating trend characterized by distinct oscillations corresponding to the discrete collapse of the layers.

The introduction of skins results in a substantial increase in IPCF. They act by distributing the load over the entire structure, engaging the honeycomb globally rather than locally. The stiffening effect is amplified in the thick-skin configuration, where the activation force necessary to crash the structure is the highest. The thin-skin panel maintains a relatively smooth energy absorption plateau, suggesting an efficient coupling in which the skins distribute the load without inducing severe instabilities. The thick-skin configuration displays large force oscillations. The high bending stiffness promotes macroscopic folding and dynamic buckling modes.

Overall, the oscillatory pattern confirms the expected collapse mechanism: the structure does not fail globally, but rather through a series of progressive local instabilities along the cell lines, similar to the progressive folding observed in aluminum tubes subjected to axial crush.

4.4.1. Specific Energy Absorption (SEA)

To quantify the crashworthiness of the design, the key metric is the Specific Energy Absorption (SEA), defined as:

$$SEA = \frac{E_{absorbed}}{m_{crashed}} \tag{4.2}$$

where energy absorbed ($E_{absorbed}$) is the total energy dissipated, calculated by integrating the reaction force over the total displacement, and crashed mass ($m_{crashed}$) is the effective mass of the structure that is subjected to deformation.
The crushed mass is calculated as follows:

$$m_{crashed} = \rho \cdot A_{res} \cdot U_{tot} \tag{4.3}$$

Density is calculated from geometry by dividing the total mass of the structure, provided by `Abaqus`, by the total volume of the core, foam, and skins.
The resistant area is the usual cross-sectional area in the XZ-plane.
Total displacement is the imposed displacement:

$$U_{tot} = 5000\,mm/s \cdot 0.01\,s = 50\,mm \tag{4.4}$$

The post-processing of report data extracted from `Abaqus/CAE` was performed in the `postprocess_SEA` file in `Excel`. After conversions and calculations, the following values

have been extracted for the first model (RHC + foam).

$$E_{absorbed} = 254.4\,\text{J} \tag{4.5}$$
$$A_{res} = A_{XZ} = 498.12 \cdot 15.31 = 7626.22\,\text{mm}^2 \tag{4.6}$$
$$m_{model} = 1.26779\,\text{kg} \tag{4.7}$$
$$V_{model} = 498.12 \cdot 200 \cdot 15.31 = 1525240.378\,\text{mm}^3 \tag{4.8}$$
$$\rho_{model} = m_{model} \cdot V_{model} = 831.21\,\text{kg/m}^3 \tag{4.9}$$
$$m_{crashed} = \rho_{model} \cdot (A_{res} \cdot U_{tot}) = 0.317\,\text{kg} \tag{4.10}$$
$$SEA = \frac{E_{absorbed}}{m_{crashed}} \approx 803\,\text{J/kg} \tag{4.11}$$

The configuration with skins exhibits much higher performance. Moreover, the total mass is slightly inferior to the core solo due to the presence of more open cells and very thin plates.

$$E_{absorbed} \approx 5570\,\text{J} \tag{4.12}$$
$$A_{res} = A_{XZ} = 500 \cdot (15.31 + 2 \cdot 0.5) = 8155\,\text{mm}^2 \tag{4.13}$$
$$m_{model} = 1.16144\,\text{kg} \tag{4.14}$$
$$V_{model} = 500 \cdot 200 \cdot 16.31 = 1631000\,\text{mm}^3 \tag{4.15}$$
$$\rho_{model} = m_{model} \cdot V_{model} = 712.103\,\text{kg/m}^3 \tag{4.16}$$
$$m_{crashed} = \rho_{model} \cdot (A_{res} \cdot U_{tot}) = 0.2893\,\text{kg} \tag{4.17}$$
$$SEA = \frac{E_{absorbed}}{m_{crashed}} \approx 19.25\,\text{kJ/kg} \tag{4.18}$$

4.5. Aluminum grid

The analysis of the previous models revealed a very high initial peak crushing force due to the significant contribution to stiffness provided by the aluminum skins. The structures demonstrated good energy absorption, however, the initial peak is undesirable as it could transmit excessive g-loads to the occupants. Moreover, the solid skins have an important impact on the overall mass of the structure. To address these two key issues, a design iteration has been undertaken: the continuous skins have been replaced with a lighter aluminum grid.

The primary objectives of the new design were to reduce stiffness, reduce mass while maintaining good specific energy absorption, and ensure structural integrity while maintaining sufficient shear strength.

To satisfy all the requirements, a grid topology with perpendicular intersections, globally

rotated by `45°` in the XY-plane, was selected. For instance, the peculiar orientation is known to be very efficient in resisting shear loads.

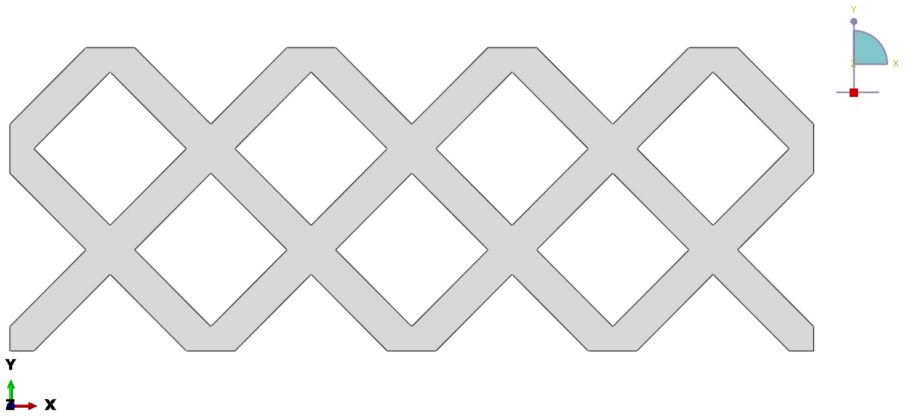

Figure 4.12: Aluminum front grid (*PART).

This new grid part was implemented in the `Abaqus/CAE` model by replacing the original `skin` parts. The geometry was generated by sketching a 500x187.5 mm shell panel and subsequently applying a patterned `extrusion cut`. The cut consists of a repeating array of rotated squares, centered to maintain symmetry.
The primary design constraint adopted was to ensure that the resulting grid bands had a width between 20 and 40 mm. Three distinct geometric configurations were developed:

- `grid4`, a pattern based on 4 square cut-outs, each with a side length of 67 mm,
- `grid5`, a pattern based on 5 square cut-outs, each with a side length of 50 mm,
- `grid6`, a pattern based on 6 square cut-outs, each with a side length of 35.36 mm.

The three configurations have been tested under identical crushing conditions to evaluate their performance against the baseline model and determine the optimal grid geometry.

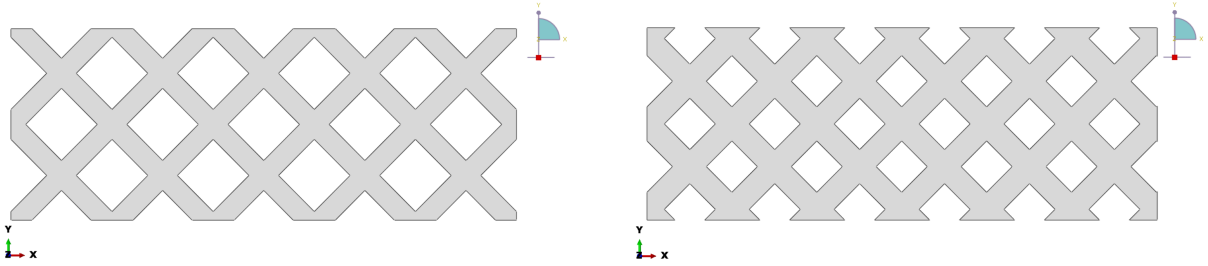

Figure 4.13: Aluminum front grids (*PART), patterns `grid5` and `grid6`.

4.5.1. Evaluation of the shear modulus G_{12}

Before proceeding, it is necessary to evaluate the loss in shear rigidity with respect to the previous case model, which has the core filled with foam and aluminum skins. The grid is designed to carry shear loads, but it is evident that it cannot perform like a continuous panel.

The analysis from Paragraph 2.3 is performed on three identical models with the three different grid. The re-entrant honeycomb geometric parameters imitate the experimental specimens dimensions. The scripts have been updated and adjusted to the new configuration. More specifically, the input file from the generation of the new models has been combined with the `Job-1.inp` derived from shear modulus analyses. In particular, a new `*TIE` has been defined between the re-entrant honeycomb core and the new grid. The rigid analytical surfaces have been removed. A force of 500 N acts on the reference point `RP1`.

The results are presented here to provide an idea of the Mises stress acting on the structure and the variation in the displacement of these peculiar configurations.

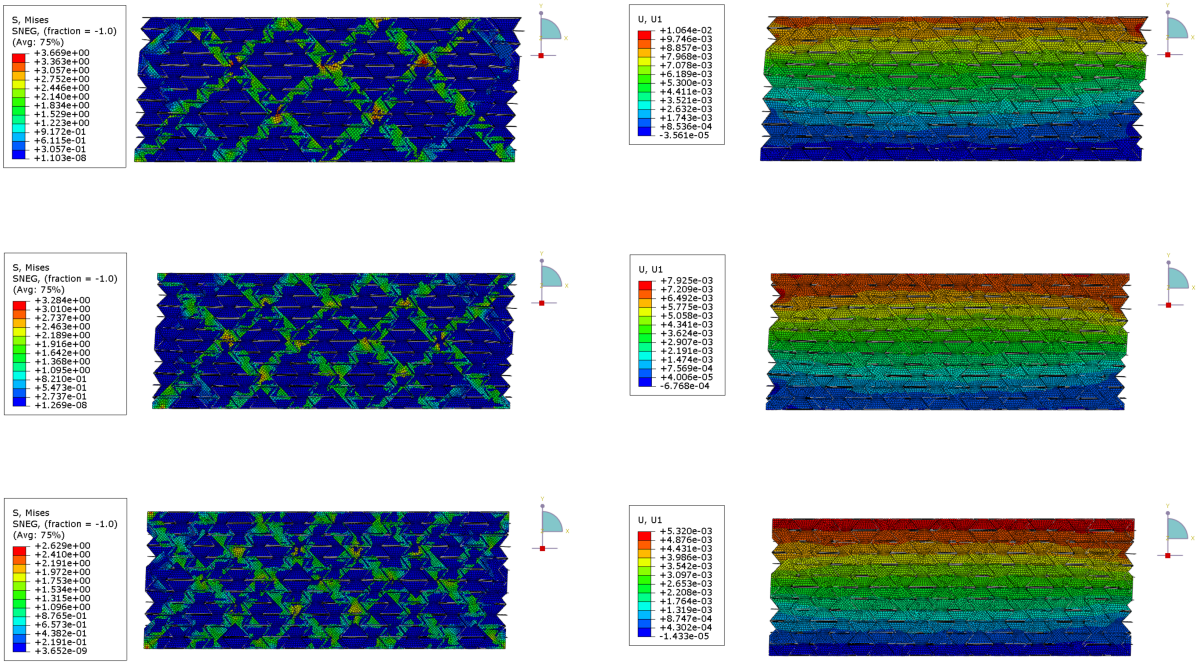

In the Output DataBase (.odb), the displacement at reference point `RP1` is plotted and saved in a report file for post-processing. The results obtained in Table 4.3 clearly demonstrate that shear resistance is preserved.

Table 4.3: Shear modulus confrontation

model	U_1 [mm]	τ	γ	G_{12} [MPa]
grid4	$9.1731 \cdot 10^{-3}$	0.0568	$0.4892 \cdot 10^{-4}$	1161.4
grid5	$7.32477 \cdot 10^{-3}$	0.0568	$0.3865 \cdot 10^{-4}$	1469.9
grid6	$5.297 \cdot 10^{-3}$	0.0568	$0.2825 \cdot 10^{-4}$	2011.2
skins	$2.837 \cdot 10^{-3}$	0.0568	$0.1513 \cdot 10^{-4}$	3755.1

4.5.2. Qualitative crash anaylis

The three models were analyzed under the impact conditions described in Paragraph 4.1, and the deformed shapes are now presented.
In all three reaction force plots, it is immediately noticeable that the absorption of energy is much smoother.

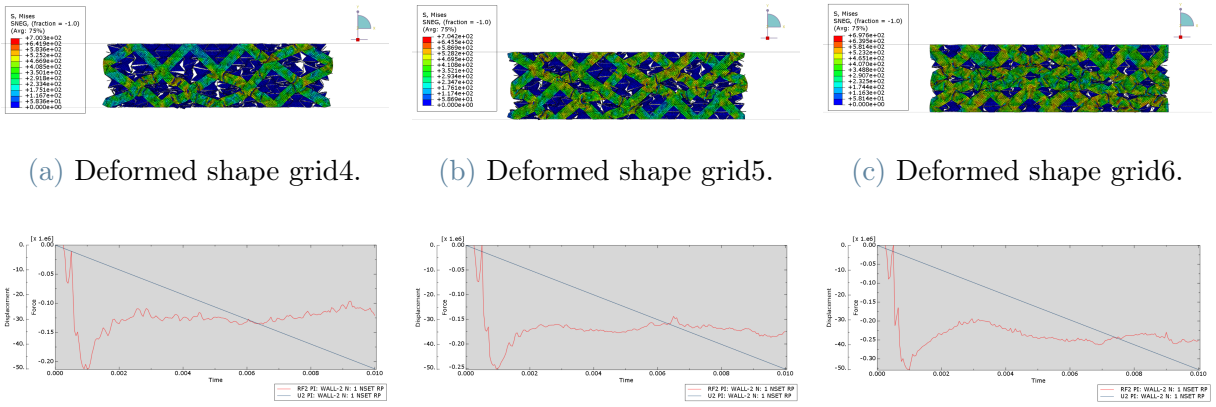

(a) Deformed shape grid4. (b) Deformed shape grid5. (c) Deformed shape grid6.

(d) Plot grid4. (e) Plot grid5. (f) Plot grid6.

Figure 4.14: Comparison of deformed shapes and corresponding force-displacement curves for grid configurations 4, 5, and 6.

4.5.3. Global compressive test on the optimized models

An additional variant is investigated: it preserves the same geometric parameters as the second optimal configuration but replaces the solid skins with aluminum `grid5` (4.13).

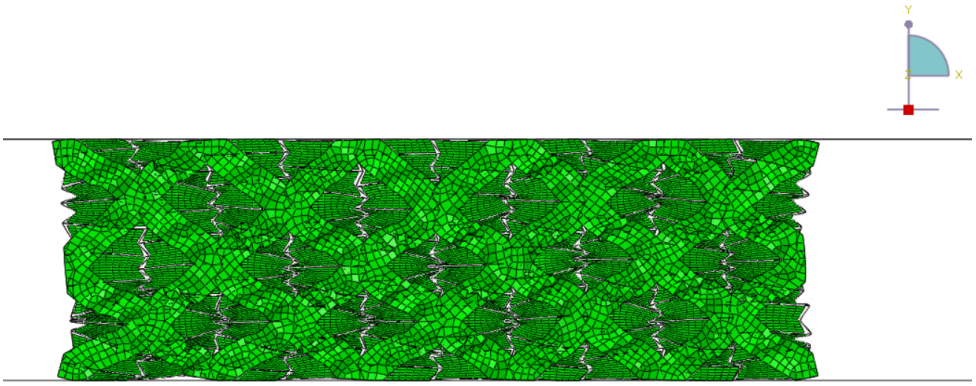

Figure 4.15: Deformed shape of the optimal RHC + foam + grid.

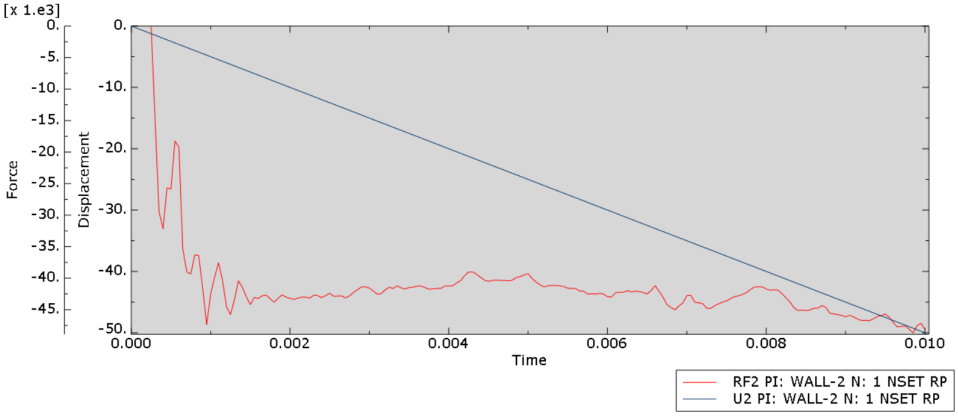

Figure 4.16: Force and displacement vs time plot.

It is immediate to observe that the peak load is more than halved with respect to the skins configuration. Moreover, the energy absorption is much more progressive and smoother.

$$E_{absorbed} \approx 1.3\,\text{kJ} \tag{4.19}$$

$$A_{res} = A_{XZ} = 500 \cdot (15.31 + 2 \cdot 0.5) = 8155\,\text{mm}^2 \tag{4.20}$$

$$m_{model} = 1.05344\,\text{kg} \tag{4.21}$$

$$V_{model} = 500 \cdot 200 \cdot 16.31 - 40 \cdot 50^2 \cdot 0.5 = 1581000\,\text{mm}^3 \tag{4.22}$$

$$\rho_{model} = m_{model} \cdot V_{model} = 666.312\,\text{kg/m}^3 \tag{4.23}$$

$$m_{crashed} = \rho_{model} \cdot (A_{res} \cdot U_{tot}) = 0.2717\,\text{kg} \tag{4.24}$$

$$SEA = \frac{E_{absorbed}}{m_{crashed}} \approx 4.8\,\text{kJ/kg} \tag{4.25}$$

4.6. Localized impact on the optimized models

The analysis described in 4.2 was performed on the three models. The punch was repositioned, and its initial velocity was set to $v_0 = 10\,\mathrm{m/s}$. The mass of the punch, concentrated at his `RP`, is increased to 6 kg.

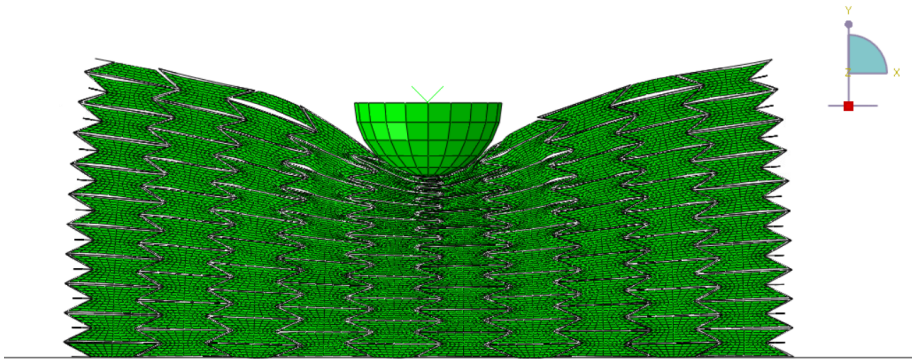

Figure 4.17: Deformed structure RHC + foam.

The analysis of the outputs reveals that the punch indentation is approximately 82 mm and the structure was able to absorb almost all the energy in 0.01 s. Post-processing of data was performed in `Excel` to calculate energy absorption and SEA.

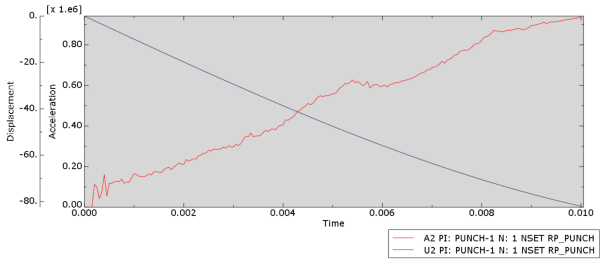

Figure 4.18: Acceleration and displacement vs time curves.

Total initial kinetic energy of the impactor was:

$$E_k = \frac{1}{2} m v_0^2 = 300\,J \tag{4.26}$$

The integration of the force-displacement curve with the trapezoidal rule results in 230 J of the initial energy absorbed. During the imposed simulation time, the crashed mass must be evaluated. Considering the total volume and the total mass of the model provided by

`Abaqus`:

$$\rho_{model} = m_{model} \cdot V_{model} = 831.2\, kg/m^3 \tag{4.27}$$

Real indentation is the total displacement of the punch minus the initial relative position between the tip of the punch (`RP`) and the upper layer of the structure:

$$U_{eff} = U_{tot} - \Delta y = 0.080\, m \tag{4.28}$$

$$m_{crashed} = \rho_{model} \cdot (U_{eff} \cdot A_{res}) = 0.08815\, kg \tag{4.29}$$

$$SEA = \frac{E_{absorbed}}{m_{crashed}} \approx 2.6\, kJ/kg \tag{4.30}$$

For the following configurations, initial velocity will be set to 5 m/s and the mass of the punch is increased to 100 kg in order to observe an appreciable indentation within the rigid aluminum skins and grid. Thereby, the initial total kinetic energy of the impactor is:

$$E_k = \frac{1}{2} m v_0^2 = 1205\, \text{J} \tag{4.31}$$

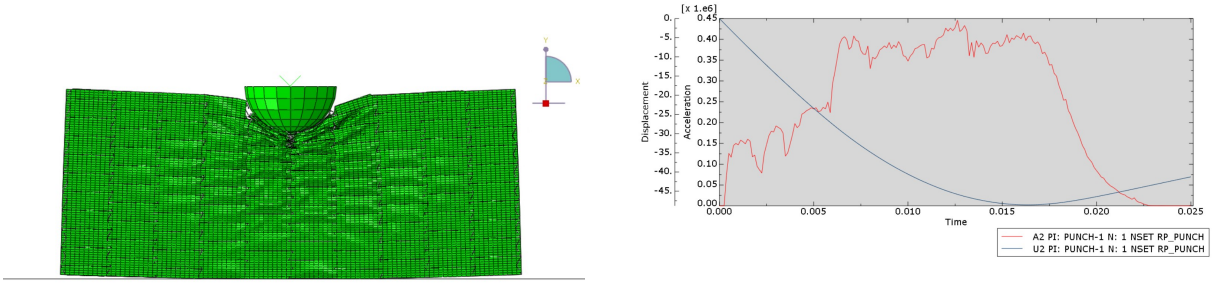

(a) Deformed shape.

(b) Acceleration and displacement vs time curves.

Figure 4.19: Localized impact for the optimum RHC + foam + skins configuration.

$$E_{absorbed} \approx 1.19\,\text{kJ} \tag{4.32}$$
$$m_{model} = 1.16144\,\text{kg} \tag{4.33}$$
$$V_{model} = 500 \cdot 200 \cdot 16.31 - 40 \cdot 50^2 \cdot 0.5 = 1631000\,\text{mm}^3 \tag{4.34}$$
$$\rho_{model} = m_{model} \cdot V_{model} = 712.103\,\text{kg/m}^3 \tag{4.35}$$
$$U_{eff} = U_{tot} - \Delta y = 0.045\,m \tag{4.36}$$
$$m_{crashed} = \rho_{model} \cdot (A_{crash} \cdot U_{eff}) = 0.0397\,\text{kg} \tag{4.37}$$
$$SEA = \frac{E_{absorbed}}{m_{crashed}} \approx 29\,\text{kJ/kg} \tag{4.38}$$

The sandwich configuration exhibits an increase in SEA of approximately 10 kJ/kg under localized impact compared to the global crushing scenario. The membrane stretching and severe localized shearing of the aluminum skins prior to failure cause this increment, which is notable but not enormous because the aluminum skins inhibit the beneficial in-plane auxetic contraction of the core.

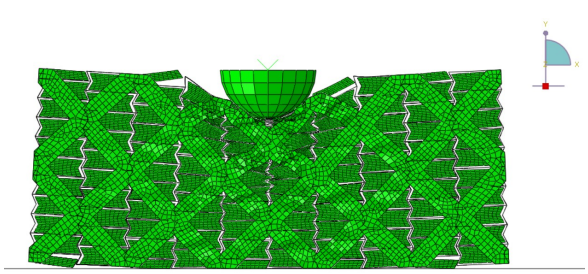

(a) Deformed shape.

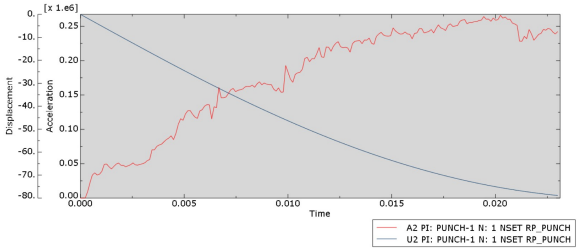

(b) Acceleration and displacement vs time curves.

Figure 4.20: Localized impact for the optimum RHC + foam + `grid5` configuration.

$$E_{absorbed} \approx 1.21\,\text{kJ} \tag{4.39}$$
$$m_{model} = 1.05344\,\text{kg} \tag{4.40}$$
$$V_{model} = 500 \cdot 200 \cdot 16.31 - 40 \cdot 50^2 \cdot 0.5 = 1581000\,\text{mm}^3 \tag{4.41}$$
$$\rho_{model} = m_{model} \cdot V_{model} = 666.312\,\text{kg/m}^3 \tag{4.42}$$
$$U_{eff} = U_{tot} - \Delta y = 0.077\,m \tag{4.43}$$
$$m_{crashed} = \rho_{model} \cdot (A_{crash} \cdot U_{eff}) = 0.0719\,\text{kg} \tag{4.44}$$
$$SEA = \frac{E_{absorbed}}{m_{crashed}} \approx 17\,\text{kJ/kg} \tag{4.45}$$

Conversely, the grid-stiffened configuration demonstrates a remarkable SEA increase,

shifting from 5 kJ/kg under global compression to roughly 17 kJ/kg under localized impact. The discontinuous nature of the grid provides essential shear stiffness while still preserving the structural degrees of freedom required for the auxetic kinematics of the re-entrant honeycomb. In this way, the core can actively draw material inward to densify beneath the punch, proving this hybrid design to be highly efficient and robust in managing localized impact.

To provide a clear overview and summarize the results gathered from the various analyses and post-processing steps, the Specific Energy Absorption (SEA) values are reported in Table 4.4.

Table 4.4: Specific Energy Absorption (SEA) values for the 3 investigated auxetic beam configurations under global compression and localized impact tests.

Configuration	**SEA (kJ/kg)**	
	Global compressive test	**Localized impact test**
Foam-filled re-entrant honeycomb	0.8	2.6
Skins reinforcement	19.0	29.0
Grids reinforcement	5.0	17.0

Although the highest absolute values are achieved with the continuous skins, it is clearly observed that the auxetic beams perform significantly better under localized impact. Furthermore, the results indicate that as the structure is progressively stiffened, the densification mechanism becomes increasingly inhibited.

4.7. Case study for an aeronautical A.T.D.

As mentioned in the Introduction, a possible and hopefully effective application of the structure that has been examined is the energy absorption system in helicopters and VTOLs.
The Federal Aviation Administration (F.A.A.) adopts the `FAA HYBRID III 50M` dummy for its regulations. It is a 50th percentile male automotive crash test dummy modified for Federal Aviation mandated crashworthiness safety testing for general and transport category aircraft and general and transport category rotorcraft [18]. Regulations impose only a maximum lumbar spine load of 6670 N when the seat is subjected to a 30 g acceleration. No other limits are imposed on the subfloor, which is part of the entire energy absorption system.
The objective of the case study is to prove if a simple configuration of this alternative structure can be more effective than the traditional solution. An increase in mass and a small decrease in shear resistance are expected.
The Anthropomorphic Testing Device (ATD) `Hybrid III 50M` is available at the LAST laboratory at Politecnico di Milano. It has got its own numerical model validated in Abaqus that will be adopted for the following simulations. The numerical tests usually aim to evaluate:

- the first aeronautical critical point, which is the lumbar acceleration;
- the second aeronautical critical point, which is the moment on the head.

The simulations conducted will focus only on the lumbar spine load to prove the effectiveness of the innovative structure. The numerical model runs through the `main.inp` file, which includes all the subsystems (seat, ATD, floor, 4-point belt) and properties. The seat is equipped with a cartridge absorber, and it is modeled as a *connector*, that establishes a preselected relationship between two points. The 4-point belt is modeled as a *beam*. The ATD is modeled as a rigid body, except for the lumbar area and the head. The `main.inp` automatically extracts the concentrated force acting in the direction of the spine (`CTF3`).
In addition to the dummy `Abaqus` model, two different versions of subfloors will be integrated under the seat.

The first one adopts four auxetic re-entrant honeycomb beams filled with foam in the optimized configuration studied in Paragraph 2.8.

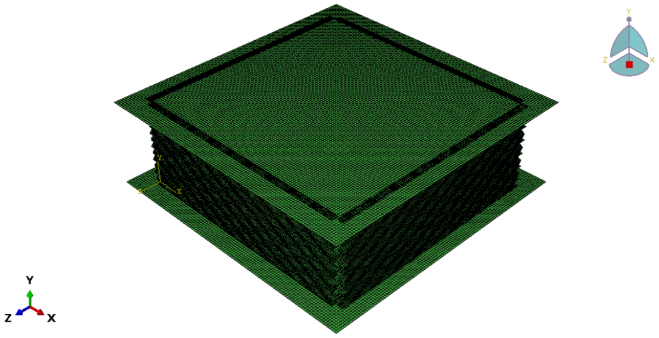

Figure 4.21: Alternative subfloor assembly using auxetic beams.

The second assembly includes aluminum grids 4.5.
The structure is simplified in `Abaqus` as an assembly of two shell skins and the central composition of auxetic beams. More specifically, the upper skin is expected to carry high flexural loads, so it is modeled as a 600×600 mm sandwich plate made of two aluminum layers separated by IMPAXX foam. IMPAXX™ is a highly engineered, extruded polystyrene foam manufactured to maximize efficiency and minimize weight [8]. The lower skin is a simple shell element plate made of aluminum.
The two configurations are tested under a typical standard scenario of free-fall conditions at an impact velocity of 8 m/s, considering two distinct surfaces: flat ground and irregular terrain. More specifically, the uneven terrain is geometrically simplified as a rigid analytical surface with a localized semicircular corrugation, designed to replicate a possible worst-case scenario where the impact energy could concentrate on a restricted section.

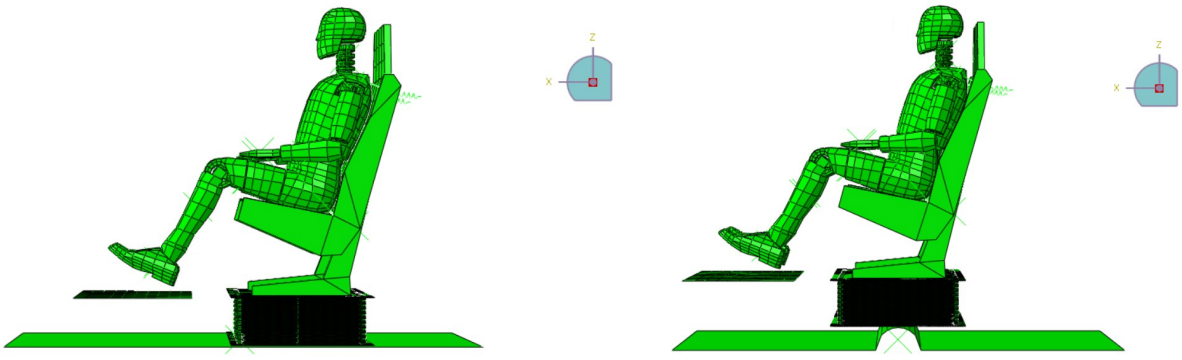

Figure 4.22: Assembly undeformed.

4.7.1. Results of the analyses

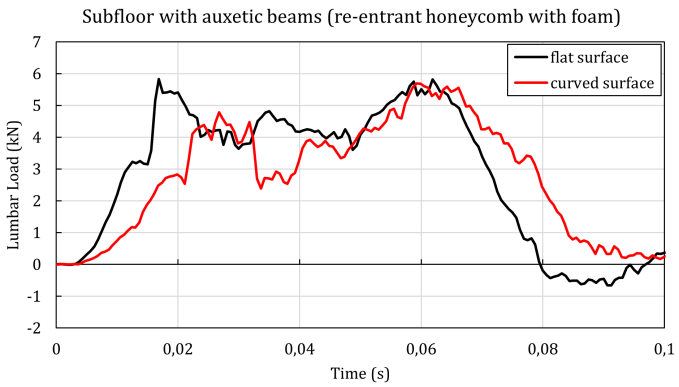

Figure 4.23: Auxetic subfloor drop test: load transmitted to the spine vs time curves.

Figure 4.23 illustrates the dynamic response of the integrated ATD, seat, and auxetic subfloor system.
In the flat impact condition, the subfloor demonstrates a uniform and progressive crushing behavior, which maximizes energy absorption and minimizes the decelerative loads transmitted to the occupant.
The impact on the irregular surface introduces a more severe asymmetric loading state, forcing the subfloor to accommodate the localized intrusion of the bump. Despite the concentrated stress, the auxetic beams effectively manage the irregular deformation profile, absorbing the kinetic energy and avoiding catastrophic structural failure. This peculiar adaptive response ensures a more controlled load transfer to the seat.
Most notably, in both impact scenarios, the maximum compressive load recorded at the occupant's lumbar spine remains strictly below the 6670 N threshold imposed by regulations. The crashworthiness and protective efficacy of the proposed innovative energy-absorption system are validated.

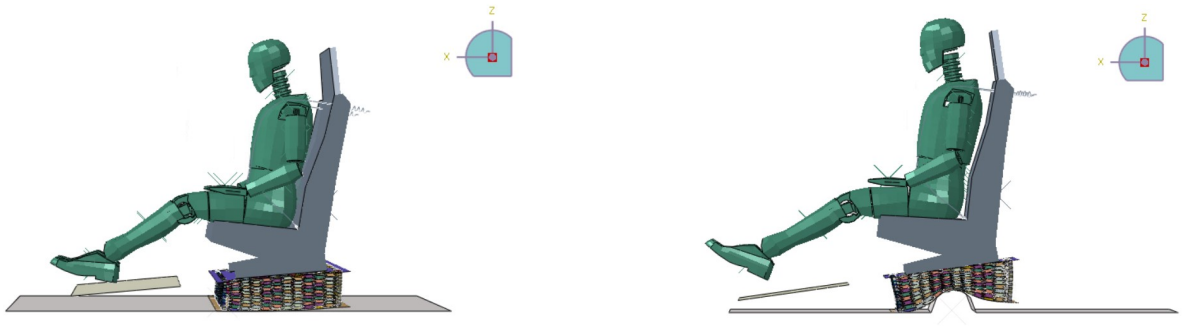

Figure 4.24: Deformed auxetic subfloor, flat and irregular terrain.

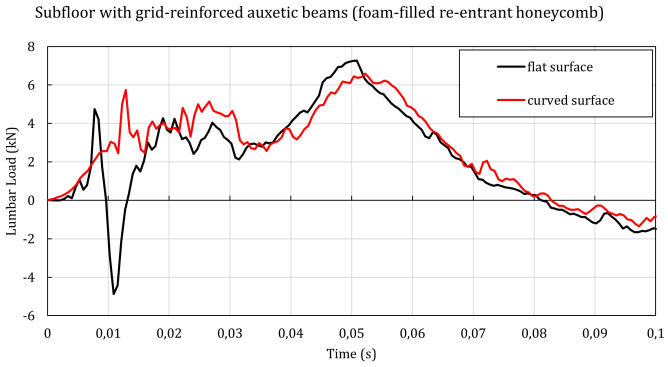

Figure 4.25: Auxetic grid-reinforced subfloor drop test: load transmitted to the spine vs time curves.

The grid-reinforced configuration exhibits a distinct dynamic behavior. During the drop onto the flat, uniform surface, the added rigidity slightly compromises the energy absorption capabilities. As shown by the black curve in Figure 4.25, the subfloor assembly fails to maintain the transmitted lumbar load below the imposed threshold. Although the compressive peak exceeds the survivability limit by a narrow margin of less than 0.4 kN. Minor geometric refinements, such as reducing the aluminum grid thickness, could easily result in a configuration that respects the limit. The impact on the irregular surface highlights the remarkable capability of auxetic structures to absorb localized severe impacts. The red curve clearly shows that the load transmitted to the spine remains safely below the threshold.

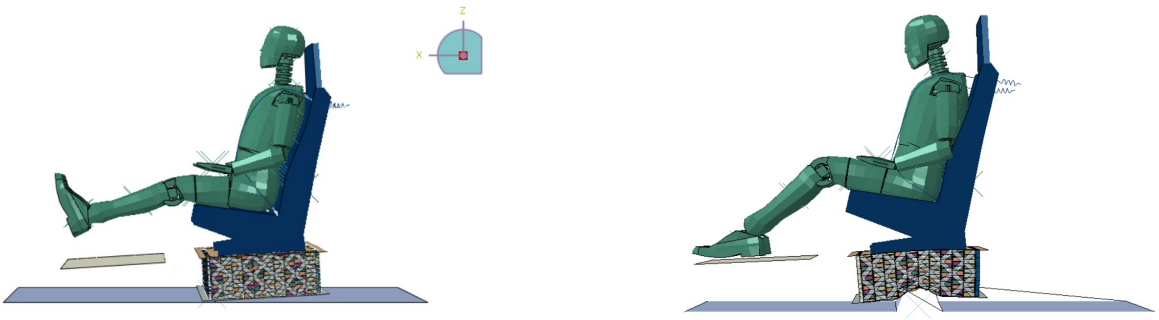

Figure 4.26: Deformed grid-reinforced auxetic subfloor, flat and irregular terrain.

5 | Conclusions and future developments

The present research effort was driven by the continuous evolution of rotorcraft safety standards, which increasingly demand lightweight structural solutions capable of superior crashworthiness. The primary objective of this thesis was to systematically investigate the mechanical performance of foam-filled aluminum re-entrant honeycombs, evaluating their potential integration as energy-absorbing subfloor components. By navigating through theoretical formulations, numerical optimizations, experimental testing, and full-scale dynamic simulations, the work aimed to assess whether the extraordinary properties of auxetic metamaterials could practically translate into safer structures.

Overall, the core objectives of the research have been successfully met, providing a comprehensive understanding of how geometric parameters influence the mechanical response of these complex beams. The extensive static analyses conducted on multiple geometric configurations confirmed the underlying hypothesis: the auxetic re-entrant core, coupled with a polymeric foam filler, exhibits exceptional behavior. Under compressive loads, the structure activates its characteristic densification mechanism, drawing material inward and providing a stable, progressive crushing response that is ideal for dissipating kinetic energy during impact. However, the transition from an idealized energy absorber to a load-bearing subfloor component revealed critical structural trade-offs. The initial objective of characterizing the elastic properties, specifically the in-plane shear modulus, highlighted a significant limitation of the bare auxetic core. While performing well in pure compression, the honeycomb-only configuration proved to be compliant in shear. In the context of a rotorcraft airframe, where the subfloor must ensure global torsional and shear stability during normal flight operations, this high compliance renders the unconstrained core unsuitable for direct structural application. To address this limitation, the research also investigated the introduction of continuous external aluminum skins. The in-plane shear stiffness was drastically increased, satisfying the structural requirements. On the other hand, the numerical and dynamic crash analyses revealed that this solution introduces severe penalties in terms of crashworthiness and overall weight. The high bending

stiffness of the solid skins alters the failure mode, inhibiting the progressive cellular folding and promoting macroscopic dynamic buckling. This results in high initial peak crash forces and fluctuating load profiles, transmitting lethal decelerations to the occupants.

The search for an optimal configuration, capable of balancing the competing needs for high shear stiffness and progressive energy absorption, led to the investigation of a third structural variant: the integration of a 45° aluminum grid in place of solid skins. The analyses indicate that this grid-stiffened configuration represents an effective intermediate solution. It provides a sufficient geometric constraint to substantially elevate the shear resistance compared to the honeycomb skeleton while mitigating the weight penalties and the severe crash force peaks. Moreover, the discontinuous nature of the grid allows the underlying re-entrant core to preserve its auxetic densification mechanism.

The successful implementation of the Finite Element Model, strictly validated against the experimental data obtained from the physical prototypes, provided the necessary confidence to extend these findings into a realistic full-scale crash scenario. The final case study, which simulated the drop test of the engineered subfloor on both flat and irregular terrains, demonstrated the excellent response of auxetic structures to localized impacts. The structure successfully managed the severe asymmetric loading conditions induced by the irregular ground, preventing catastrophic failure and ensuring that the loads transferred to the seat structure remained always within survivable thresholds.

Despite these encouraging results, the current research indicates that the absolute optimum has yet to be found. The optimized geometry provides a good baseline, but further adjustments are needed to tailor the stiffness and energy absorption for real aeronautical applications. Building on these findings, future research should focus on two main steps to mature this subfloor concept.

First and foremost, it should consider the transition from aluminum alloys to advanced composite materials, such as Carbon Fiber Reinforced Polymers (CFRP) or Glass Fiber Reinforced Polymers (GFRP). Manufacturing the re-entrant skeleton out of composites could drastically increase the Specific Energy Absorption and the global stiffness-to-weight ratio, pushing the performance boundaries significantly beyond the achievable values typical of isotropic metals. Secondly, the integration of the auxetic energy absorbers into the actual rotorcraft subfloor requires a much deeper investigation. In this work, the subfloor integration was treated as a final demonstrative case study to validate the dynamic performance of the isolated components. Future studies must address the complex structural interactions between the auxetic beams, the fuselage frames, and the outer aerodynamic skin. This includes analyzing complex joining techniques, the effects of multi-axial com-

bined loading, and the response to off-axis impacts, which are statistically frequent in helicopter crash scenarios.
Exploring all those aspects will be the necessary next step to possibly transition the proposed auxetic subfloor concept from a numerical and experimental prototype into a certified crashworthy system.

Bibliography

[1] Aearo Technologies. Confor™ m foams. `https://www.aearotechnologies.com/materials/confor-m-foams/`, 2026. Accesso: 29 gennaio 2026.

[2] A. Airoldi. Proprietà significative delle leghe leggere d'alluminio nella progettazione ad assorbimento di energia delle strutture aeronautiche. *La metallurgia italiana*, March 2008.

[3] A. Airoldi, N. Novak, F. Sgobba, A. Gilardelli, and M. Borovinsek. Foam-filled energy absorbers with auxetic behaviour for localized impacts. *Materials Science Engineering A*, 788, 2020.

[4] K. L. ALDERSON, A. FITZGERALD, and K. E. EVANS. The strain dependent indentation resilience of auxetic microporous polyethylene. *Journal of Materials Science*, 35:4039–4047, 2000.

[5] P. Astori, M. Zanella, and M. Bernardini. Validation of numerical models of a rotorcraft crashworthy seat and subfloor. *MDPI Aerospace*, December 2020.

[6] F. M. B., J. L. J. Pereira, G. A. Oliver, C. S. S. Roque da Silva, L. R., and G. F. Gomes. A review on the energy absorption response and structural applications of auxetic structures. *Mechanics of Advanced Materials and Structures*, 29:5823–5842, 2022.

[7] V. Burlayenkoa and T. Sadowski. Effective elastic properties of foam-filled honeycomb cores of sandwich panels. *Composite Structures*, 92:2890–2900, 2010.

[8] Coastal Automotive. Impaxx stable consistent energy absorbing foam. `https://coastal-automotive.com/solutions/impaxx/`, 2026. Accesso: 27 gennaio 2026.

[9] J. D. Cronkhite. Crashworthy design concepts for airframe structures of light air. *SAE Transactions*, 90(2):2125–2137, 1981.

[10] Z. Dong, Y. Li, T. Zhao, W. Wu, D. Xiao, and J. Liang. Experimental and numerical studies on the compressive mechanical properties of the metallic auxetic reentrant honeycomb. *Materials and Design*, 182, 2019.

[11] DuPont. kapton original, summary of properties. https://www.beta.dupont.com/content/dam/electronics/amer/us/en/electronics/public/documents/en/EI-10142_Kapton-Summary-of-Properties.pdf, 2025. Accesso: 15 dicembre 2025.

[12] European Aviation Safety Agency. *EASA CS-27: Certification Specifications for Small Rotorcraft*. European Aviation Safety Agency, Cologne, Germany, amendment 4 edition, 2016.

[13] European Aviation Safety Agency. *EASA CS-29: Certification Specifications for Small Rotorcraft*. European Aviation Safety Agency, Cologne, Germany, amendment 4 edition, 2016.

[14] A. Galbiati. Composite chiral absorber for localized impacts. Tesi di laurea magistrale, Politecnico di Milano, Milano, Italia, 2024.

[15] L. Gibson. Lecture 4: Honeycombs, in-plane behavior. Lecture slides, Massachusetts Institute of Technology, Spring 2015. URL https://ocw.mit.edu/courses/3-054-cellular-solids-structure-properties-and-applications-spring-2015/179b3dcc703bb34a34e4490c29c97f35_MIT3_054S15_L4_honey_trans.pdf. MIT OpenCourseWare, Course 3.054.

[16] L. J. Gibson, M. F. Ashby, G. S. SCHAJER, and C. I. Robertson. The mechanics of two-dimensional cellular materials. *Journal of the American Helicopter Society*, 382 (1782):25–42, 1982.

[17] K. Hughes, R. Vignjevic, and J. Campbell. Experimental observations of an 8 m/s drop test of a metallic helicopter underfloor structure onto a hard surface: part 1. *Journal of Aerospace Engineering*, 221(5):661–678, 2007.

[18] HUMANETICS. Faa hybrid iii 50m. https://www.humaneticsgroup.com/products/anthropomorphic-test-devices/aerospace-military/faa-hybrid-iii-50m#:~:text=The%20FAA%20HIII-50M%20is%20a%20Hybrid%20III%2050th,category%20aircraft%20and%20general%20and%20transport%20category%20rotorcraft., 2026. Accesso: 15 gennaio 2026.

[19] K. E. Jackson. Advances in rotorcraft crashworthiness – trends leading to improved survivability. *Journal of the American Helicopter Society*, 63(2):1–25, 2018.

[20] P. U. Kelkar, H. S. Kim, K.-H. Cho, J. Y. Kwak, C.-Y. Kang, and H.-C. Song. Cellular auxetic structures for mechanical metamaterials: A review. *Sensors*, 20 (3132), 2020.

[21] E. Kucukkalfa, B. Yilmaz, and K. Yildiz. Synergistic effects of foam reinforcement and geometric parameters on the mechanics of re-entrant auxetic structures. *Experimental Mechanics*, 65:1167–1181, June 2025.

[22] V. Lopresto. Crashworthiness design and evaluation of civil aircraft structures. *Progress in Aerospace Sciences*, 148, 2024.

[23] H. C. Luo, X. Ren, Y. Zhang, X. Y. Zhang, X. G. Zhang, C. Luo, X. Cheng, and Y. M. Xie. Mechanical properties of foam-filled hexagonal and re-entrant honeycombs under uniaxial compression. *Composite Structures*, 280, 2022.

[24] I. G. Masters and K. E. Evans. Models for the elastic deformation of honeycombs. *Composite Structures*, 35:403–422, 1996.

[25] S. B. R. M. F. Muhammad Azeem Aslam, Zhang Ke and I. M. Bello. An investigation of soft impacts on selected aerospace grade alloys based on johnson-cook material model. *Journal of Physics: Conference Series*, 1707, 2020.

[26] M. Najafi, H. Ahmadi, and G. Liaghat. Experimental investigation on energy absorption of auxetic structures. *Materials Today: Proceedings*, 34:350–355, 2021.

[27] N. Novak, M. Vesenjak, and Z. Ren. Auxetic cellular materials - a review. *Journal of Mechanical Engineering*, 62:485–493, 2016.

[28] N. Novak, H. Al-Rifaie, A. Airoldi, L. Krstulović-Opara, T. Łodygowski, Z. Ren, and M. Vesenjak. Quasi-static and impact behaviour of foam-filled graded auxetic panel. *International Journal of Impact Engineering*, 178, August 2023.

[29] B. Schürger, J. Bocko, P. Frankovský, I. Delyová, and J. Kostka. Directional auxetic behavior of mechanical metamaterials: Material-dependent and geometry-driven mechanisms. *Materials*, 18(5103), 2025.

[30] C. Yang, H. D. Vora, and Y. Chang. Behavior of auxetic structures under compression and impact forces. *Smart Materials and Structures*, 27, January 2018.

[31] B. Yilmaz, E. Akar, E. Kucukkalfa, and K. Yildiz. Direct foaming approach for reinforcing reentrant auxetic structures for superior compressive properties and energy absorption. *International Conference on Recent Advances in Air and Space Technologies (RAST)*, 10th edition, 2023.

[32] D. Zenkert. *The Handbook of Sandwich Construction*. EMAS (Engineering Materials Advisory Services), West Midlands, UK, 1995. ISBN 0947817964.

List of Figures

List of Tables

List of Symbols

Variable	Description	Unit
E	energy	J
E_{11}	transverse Young's modulus	MPa
E_{22}	longitudinal Young's modulus	MPa
G_{12}	in-plane shear modulus	MPa
m	mass	kg
RF	reaction force	N
SEA	specific energy absorption	J/kg
U_1	nodal displacement in x	m
U_2	nodal displacement in y	m
v	velocity	m/s
γ	shear strain	-
ν_{12}, ν_{21}	Poisson's ratios	-
ρ	density	kg/m^3
τ	shear stress	MPa
θ	re-entrant angle	$^\circ$

Acknowledgements

Desidero ringraziare il professor Airoldi per avermi dato l'opportunità di avere un assaggio del mondo della ricerca e per aver condiviso la propria esperienza, permettendomi di indagare un ambito nuovo e affascinante.
Ringrazio il dottor Caporale per avermi guidato con sapienza e pazienza in ogni aspetto di questo grande lavoro.
Ringrazio mamma e papà per il supporto, il coraggio e il silenzioso sacrificio che hanno fatto per permettermi di studiare e realizzare i miei sogni.
Ringrazio la mia speciale sorellina Anna, la stellina che illumina la mia vita.
Infine, un ringraziamento di cuore va a tutte le persone che ho avuto la fortuna e il privilegio di conoscere in questi 5 intensi anni tra Verona, Milano e Madrid. Ringrazio chi rappresenta un pilastro fondante della mia vita, chi è stato anche solo di passaggio, chi è al mio fianco da sempre e chi è arrivato da poco. Siete tanti e troppo speciali, pertanto vi dedicherò un messaggio ciascuno. Grazie per avermi aiutato a crescere, accompagnandomi fino a questo traguardo.